Spin-active color centers in silicon carbide for telecom-compatible quantum technologies

Tom Bosma

Book cover: Impression of an amber stone with a spider inclusion, illuminated by a beam of white light. Cover design by Martin C. Kamminga.

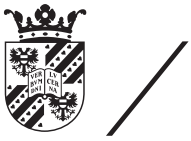

university of groningen

faculty of science and engineering

zernike institute for advanced materials

Zernike Institute PhD thesis series 2021-06
ISSN: 1570-1530

The work described in this thesis was performed in the research groups Physics of Quantum and Nanodevices of the Zernike Institute for Advanced Materials at the University of Groningen, The Netherlands. This work was supported by The Zernike Institute for Advanced Materials and the EU QuanTELCO project

Printed by Ipskamp Drukkers, Enschede

rijksuniversiteit
groningen

Spin-active color centers in silicon carbide for telecom-compatible quantum technologies

Proefschrift

ter verkrijging van de graad van doctor aan de
Rijksuniversiteit Groningen
op gezag van de
rector magnificus prof. dr. C. Wijmenga
en volgens besluit van het College voor Promoties.

De openbare verdediging zal plaatsvinden op

vrijdag 19 februari 2021 om 16:15 uur

door

Tom Bosma

geboren op 21 maart 1992
te Sneek

Promotor:
Prof. dr. ir. C. H. van der Wal

Copromotor:
Dr. R. W. A. Havenith

Beoordelingscommissie:
Prof. dr. C. Bonato
Prof. dr. A. Polman
Prof. dr. G. Palasantzas

Contents

CHAPTER 1

Introduction

Silicon carbide is a material that forms wonderful crystal structures, and can be described as a perfect mixture between silicon and diamond. SiC hardly occurs naturally, which is surprising considering that it consists of two of the most abundant elements on earth. As material it has many similarities to diamond, such as high hardness and high thermal stability. But even though the latter exists naturally in much larger quantities, SiC is far easier to grow synthetically [1,2], boasting two to three orders of magnitude lower production costs.

Its versatile material properties allow for silicon carbide to be used in various mechanical and electronic applications. For instance, its high hardness makes it suitable as abrasive material [3]. Combined with its high-temperature stability it is suitable as high-performance disk brake in cars [4]. Furthermore, its semiconductor nature allows for it to be used in high-voltage or high-temperature applications as electronic component, such as Schottky diodes, FETs and RF switches [5,6].

In the past decade SiC has gained renewed scientific interest with its promise for hosting bits for quantum information technology. Similar to NV centers diamond [7,8] SiC can host a wide variety of spin-active color centers, which may be used as quantum bit (qubit). Several potential qubits have been identified in silicon carbide [9–14], some of which even emit at telecom wavelengths [15], enabling efficient long-distance entanglement generation for quantum key distribution [16]. These bits can also be applied in the medical industry for sensing small environmental changes in biological systems [17]. SiC's biocompatibility makes it a good candidate for such biosensing applications [18].

The research described in this thesis aims at characterizing and identifying qubits with optimal properties in silicon carbide. We discovered that ensembles of molybdenum impurities in SiC have

favorable fine structure (Chapter 2) and long spin-relaxation time at low temperatures (Chapter 3). We also investigated the occurrence of electromagnetically induced transparency in divacancy defect ensembles with large inhomogeneous broadening (Chapter 4). Additional work is done to analyze SiC's prospects for integrated optical applications that can be easily combined with existing semiconductor architectures. As such, we engineered a novel single-crystal SiC waveguide structure where n-type doped layers are used as cladding material (Chapter 5).

1

1.1 Color center qubits in silicon carbide

Some gemstones get their vibrant colors from impurity atoms in their crystal structure. For example in chromium doped aluminum oxide, also known as ruby, the chromium impurities absorb a big portion of the visible spectrum and emit at a single wavelength (694 nm), giving the material its saturated red color [19]. For this reason such impurity defects are called color centers.

When it comes to impurities, silicon carbide is a very generous material. Many defects can slip into the material during growth [9], which generally hampers its operation in semiconductor applications. Examples are impurity atoms like molybdenum, vanadium and chrome [20], or vacancies and even divacancy defects [10], where neighboring carbon and silicon atoms are missing from the crystal lattice. A lot of work has been devoted to reduce the amount of defects in SiC throughout the past century. As a part of learning how to reduce the occurrence of a certain defect, its properties had to be studied. Across decades this research has accumulated to an impressive library of defects in SiC and their optical [9], electronic [21], and magnetic [20] properties. Still, many properties such as their fine structure and spin lifetimes are unknown. This library we now happily use to pick potential qubits in SiC and to fill in the blanks.

Apart from the variety of possible defect centers, SiC also has a great diversity in possible polytypes. These differ significantly in material properties, such as band gap. Dependent on the stacking sequence of the alternating Si and C layers, the lattice also displays different symmetries. In Fig. 1.1 three of the most common polytypes are shown. For the 3C-SiC lattice, the repeating ABC stacking sequence is strictly cubic. However, for the 4H-SiC lattice, the repeating sequence of ABCB has alternating layers of cubic and hexagonal symmetry. Dependent on the position of defects in the lattice, their properties will vary due to the different local crystal fields. For instance, vanadium defects substituting a silicon atom have been shown to exhibit anisotropic Zeeman splitting when on a hexagonal site in both

4H-SiC and 6H-SiC, whereas on cubic sites they display isotropic Zeeman behavior [20]. Additionally, the optical transitions for defects at hexagonal sites are often shifted from those for cubic sites [11,15]. Control over the growth of many different polytypes has already been established at great length [22], providing great tunability for defects in SiC.

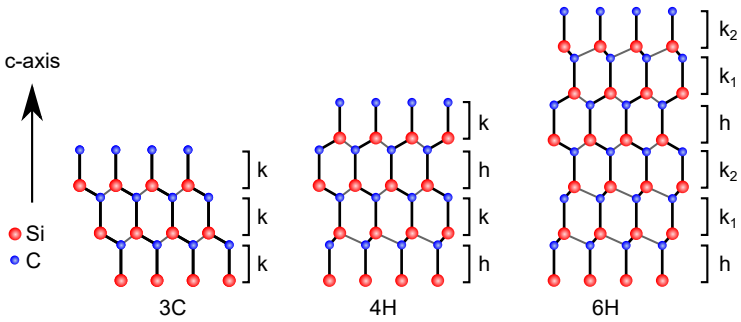

Figure 1.1: Polytypes of SiC. The specific polytypes are determined by the stacking sequence along the growth direction (c-axis). 3C-SiC has repeating sequence of length 3 (ABC) and all-cubic (k) symmetry. 4H-SiC has layers that alternate with local hexagonal (h) and cubic (k) symmetry. On top of that, 6H-SiC has inequivalent lattice sites (k_1, k_2) of cubic symmetry as well. The stacking sequence for 4H-SiC is ABCB, while it is ABCACB for 6H-SiC.

The color center defects under study in this thesis are transition-metal impurities with electronic transitions in the near-infrared. In the right charge state, these atoms have a favorable fine structure, such as a doublet or triplet electronic spin. The SiC host lattice screens these spins from external influences and maintains a steady environment, protecting their quantum states. Conversely, lattice vibrations and other impurities may cause additional disruption to these states. In combination with spin-orbit coupling the symmetry of the lattice might impose more restraints on the spin behavior, as will be discussed in Chapter 2 and 3 on molybdenum defects in SiC. The combination of the transition metal's electronic spin, the lattice symmetry and spin-orbit coupling define the spin properties of such defects.

Figure 1.2 depicts an example of a qubit energy level scheme. The two ground state levels $|g_\uparrow\rangle$ and $|g_\downarrow\rangle$ represent two spin states. The excited state level $|e\rangle$ represents a level that allows for linking transitions, and via which the system's spin might be polarized, controlled and detected. In the case of optical spin polarization this would occur by *e.g.* resonantly exciting the $|g_\uparrow\rangle - |e\rangle$ transition and waiting for the system to decay from the excited state into the $|g_\downarrow\rangle$ state.

This scheme already reveals three requirements for a proper qubit. First

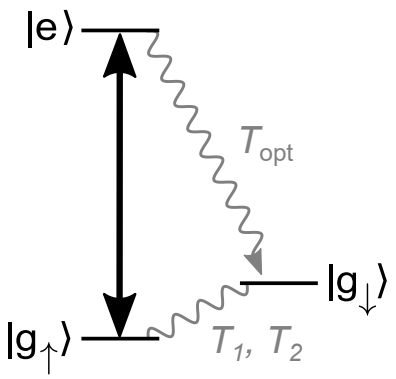

Figure 1.2: Qubit energy-level scheme. Basic energy-level scheme for a qubit that can be prepared optically by a resonant laser (black arrow). The decay paths and timescales for the optical lifetime T_{opt}, spin-flip time T_1 and ground-state spin coherence T_2 are indicated.

and second, the spin-flip time T_1 after which $|g_\downarrow\rangle$ decays back to $|g_\uparrow\rangle$ and the coherence time T_2 should be long enough to complete the computing or communication operation at hand. In order to gain from the benefits of quantum information, *e.g.* eavesdrop-free communication and the ability to detect an intruder, distant qubits need to be entangled coherently via optical communication with a well-defined phase of the quantum state [23], this makes the coherence time T_2 an important parameter. As a third requirement there is the optical lifetime T_{opt}, which determines how fast the spin can be controlled and detected. Since the readout rate for optical readout is limited to the spin-polarization speed, T_{opt} should be as short as possible while maintaining spectral selectivity [24].

1.2 Qubits at telecom wavelength

Beyond the intrinsic requirements for qubits described before, one also needs to consider the infrastructural necessities for properly setting up a quantum communication network. Many approaches for establishing entanglement for quantum key distribution rely on detecting a single photon from distant qubits. If this photon is absorbed or otherwise lost during transmission, one fails to recognize proper entanglement.

Therefore, the attenuation length of the optical channel is an important parameter, since it defines the limit in distance across which entanglement can be established. For easy scalability, the existing world-wide fiber-optic infrastructure should be used. Fig 1.3 shows the $1/e$ attenuation lengths

for standard optical fibers[25,26]. The telecom bands, specifically the C-band (1530-1565 nm) displays the lowest absorption. Additionally, for the O-band (12601360 nm) silica glass has zero dispersion, meaning signal distortion from chromatic aberrations will be minimized. Moreover, the majority of the classical communication signals are now in the (conventional) C-band, leaving the O-band relatively quiet. Thus, color centers emitting at wavelengths within the telecom O-band provide an interesting option for long-distance quantum communication.

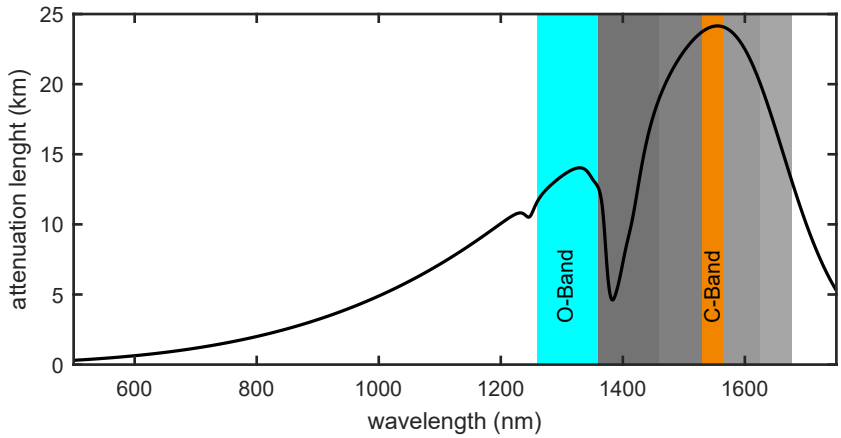

Figure 1.3: Silica fiber attenuation length around telecom wavelengths. This graph based on models for Rayleigh scattering, OH^- absorption and infrared absorption in silica fibers[25,26]. The O-Band and C-Band are specifically marked (cyan and orange shades, resp.), the dark-to-bright-gray shaded regions mark the E-Band, S-Band, L-Band and U-Band, respectively.

Although it is possible to perform a quantum frequency conversion to convert single photons from *e.g.* nitrogen-vacancy centers (637 nm) to telecom wavelengths[27], this is technologically very demanding and is accompanied by losses, limiting the rate at which entanglement can be established. Therefore, the majority of work in this thesis is aimed towards finding qubits operating at telecom wavelengths. Of course, due to the attenuation length below 15 km any entangled state needs to be relayed via quantum repeaters[28], where telecom-compatible color-center qubits in SiC could also play a prominent role.

1.3 SiC as electro-optical device platform

Silicon carbide's semiconductor nature is a great advantage for integrating optical and electrical control of color center qubits. Control over n-type or p-type doping during growth has already been established at industrial levels. This allows for electrical control over the Fermi level and thus the charge state of color center defects. It also allows for RF control to coherently address the spin states [29].

An advantage that doping control brings, is in the difference in optical transmission properties of doped versus undoped SiC and that it allows for creating monolithic waveguides. In any material free charge carriers will move to counter an applied electric field. For electric fields oscillating at low enough frequencies the entire field will be canceled. For such fields the reflectance will approach unity. Beyond a certain frequency, *i.e.* the plasma frequency, free carriers will not cancel the entire field and allow for the material to become polarized. However, the net polarization response of the material to the applied optical electrical field will still be reduced by this free carrier motion [30]. Therefore, the refractive index will be lower for a doped material, which allows for total internal reflection at an undoped/doped interface for light propagating in the undoped region. Thus, a system with alternating doped and undoped layers can be engineered to act as waveguide.

Growing an undoped layer of SiC on a highly n-doped substrate and etching it into narrow bars yields a 1D waveguide. Light focused into the core will remain confined during its propagation. Thus, the high optical intensity at the beam focus will be maintained throughout the length of the sample, well beyond the Rayleigh length in free space. This is advantageous, as quantum-optical features such as electromagnetically induced transparency (EIT) in color-center defects show increased contrast for higher laser intensities [31]. By choosing the appropriate layer sizes it is possible to fabricate single-mode waveguides, where the electrical field distribution along the cross section follows a fundamental Gaussian. This enables accurate modeling of the interaction between the optical field and defect ensembles. Additionally, topping the stack off with a p-type SiC cladding would not only protect the core from some inhomogeneities such as strain, it would also open up interesting possibilities for electrical control, as it effectively becomes a p-i-n junction. In chapter 5 we report on the feasibility of fabricating these waveguide devices in SiC.

1.4 Characterization methods

Throughout this thesis several methods for optical characterization of color-center ensembles in SiC will be discussed. Below is a summary of the methods most commonly used by our research group. Generally, they are employed in the order of appearance, as the progressive insight gained throughout this string of methods allows for continuous optimization of the signal-to-noise ratio, resolution etc.

Photoluminescence (PL) We start the optical characterization of the crystal defects by collecting a photoluminescence spectrum of the defect. This is often done by exciting the defect ensembles using a laser with above band-gap photon energy and measuring the emission spectrum. An example of such spectrum for molybdenum defects in SiC is shown in Fig. 1.4a. In this spectrum the wavelength of the zero-phonon line (ZPL) transition for *e.g.* molybdenum can be found. At this wavelength we will later drive resonant transitions in the defects. The PL spectrum also shows the phonon-sideband emission (PSB), which will be used for the detection of emission when resonantly addressing the color centers. Finally, two ZPL emission signatures originating from tungsten defects are visible at longer wavelengths[9].

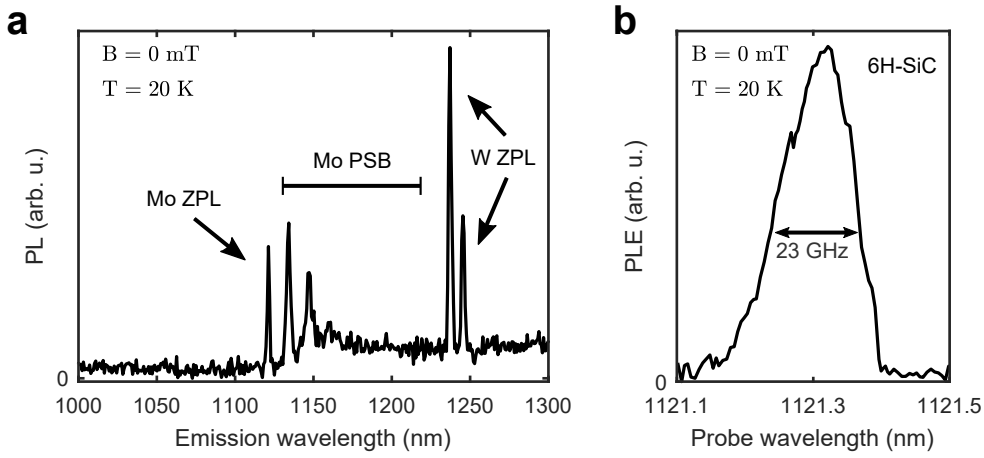

Figure 1.4: Photoluminescence spectra for 6H-SiC. a) Photoluminescence (PL) spectrum of molybdenum and tungsten in 6H-SiC. The zero-phonon line (ZPL) and phonon sideband (PSB) of molybdenum are labeled, as well as two ZPLs originating from tungsten impurities[9]. **b)** The molybdenum ZPL as measured in PLE, exhibiting a 23 GHz inhomogeneous broadening.

Photoluminescence Excitation (PLE) Broadening of the emission lines and resolution limits for spectrometers restrict how well underlying electronic transitions can be resolved. Using photoluminescence excitation allows us to investigate these transitions in more detail. By sweeping the wavelength of a single excitation laser across the ZPL wavelength and measuring the integrated PSB emission intensity, the zero-phonon line can be determined at a resolution set by the laser linewidth. A typical PLE scan for the molybdenum ZPL is shown in Fig. 1.4b. With its 23 GHz linewidth, the ZPL is still about a thousand times broader than the homogeneous electronic transition linewidth. This widening originates from inhomogeneous broadening due to *e.g.* nonuniform strain [32] throughout the defect ensemble. The homogeneous linewidth is usually several orders of magnitude smaller. For small magnetic fields (up to 1 T) any Zeeman shift of spin-state transitions will be obscured by this inhomogeneous broadening. To reveal this fine structure, we employ two-laser magnetospectroscopy methods.

Two-laser spectroscopy magnetospectroscopy In two-laser spectroscopy we use a control laser to drive spin polarization exclusively in the part of the ensemble that has transitions resonant with this laser. A second laser is used to resonantly probe the spin-state we polarized into. In this way we only get a PLE response from a resonant homogeneous subensemble, eliminating most of the inhomogeneous broadening. Figure 1.5a demonstrates the experimental approach for a four-level system. The control laser is kept at a fixed frequency (generally at the center of the ZPL as measured in PLE) and will be resonant with the $|g_\downarrow\rangle - |e\rangle$ transition for some part of the ensemble. Upon continuous excitation, the system will eventually decay into the $|g_\uparrow\rangle$ spin state, which is generally long lived. This strongly reduces the photoluminescence emission. The probe laser is detuned from the first one by a variable frequency δ. If the two-laser detuning δ is equal to the energy difference between $|g_\downarrow\rangle$ and $|g_\uparrow\rangle$, the spin polarization is disturbed and the emission reduction is lifted. Figure 1.5b shows a typical two-laser scan. Bright peaks appear at specific two-laser detunings δ, which we use to determine the energy level splittings. Since multiple peaks appear in this plot, the level structure is more complex than depicted in Fig 1.5a.

Coherent population trapping (CPT) To evaluate the coherence properties of the color-center defects we can use coherent population trapping (CPT). This phenomenon occurs when a system is driven by two lasers in the configuration of Fig 1.5a, *i.e.* both lasers couple two different states $|g_\uparrow\rangle$ and $|g_\downarrow\rangle$ to a common state $|e\rangle$. As can be seen in the figure, such

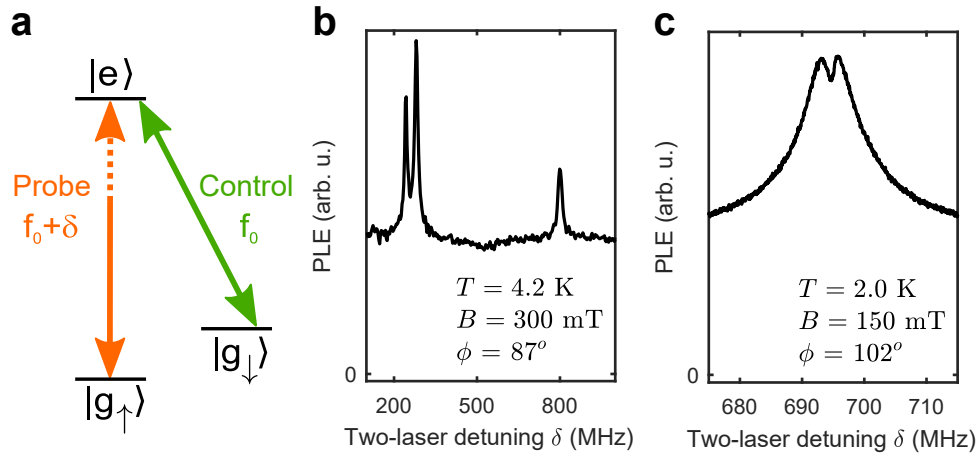

Figure 1.5: Two-laser spectroscopy for Mo in 6H-SiC. a) Working principle of two-laser spectroscopy, here shown for a three-level system: A control laser addresses the $|g_\downarrow\rangle$-$|e\rangle$ transition, thereby polarizing the spin into the $|g_\uparrow\rangle$ state, reducing the PLE response. A probe laser detuned with a frequency δ from the control laser frequency f_0 counters this spin polarization if it becomes resonant with the $|g_\uparrow\rangle$-$|e\rangle$ transition, increasing the PLE response. **b)** Example of a two-laser spectroscopy scan. Several sharp peaks appear, indicating that more than a single two-laser pumping scheme is possible (ϕ is the angle between the crystal c-axis and the applied magnetic field direction). **c)** Example of a CPT feature within a two-laser absorption peak.

a system traces out the Greek letter Lambda (Λ) and is therefore called a Λ system. At exact two-photon resonance the excitation pathways of both lasers interfere destructively, when the system is in the state [31]

$$|\Psi_{\mathrm{CPT}}\rangle = \Omega_p\,|g_\downarrow\rangle - \Omega_c\,|g_\uparrow\rangle\,, \tag{1.1}$$

with $\Omega_{c(p)}$ the Rabi frequency from the control (probe) laser. The system's dynamics therefore has the tendency to get trapped in this state. Since all terms with $|e\rangle$ vanish, the system cannot reach the excited state anymore: it is coherently trapped in the ground state. Therefore, the absorption of a defect ensemble, and thus the fluorescence emission, will be reduced under CPT conditions. An example of this is shown in Fig. 1.5c, where a clear emission dip is visible within the two-laser spectroscopy feature. The width of this dip is inversely proportional to the ensemble-averaged coherence time T_2^*. Note that for large enough control-beam Rabi frequency the absorption will drop to zero. If one were to measure the transmission through an optically thick material, it would become transparent under these conditions. In that case we speak of electromagnetically induced transparency (EIT).

Time-resolved PLE The method for detecting spin and polarizing states in two-laser spectroscopy can also be used to measure the T_1 spin-flip time: the time it takes before a spin-polarized state will decay back to thermal equilibrium. In such experiments we use a single pulsed laser. Starting from thermal equilibrium, a first pulse polarizes the spins, *e.g.* into $|g_\uparrow\rangle$. Then after a variable delay a second pulse probes the spins that flipped back to the $|g_\downarrow\rangle$ state. The time-resolved PLE emission is measured with a single-photon counter, where the difference in response between the first and second pulse is a measure for the recovery to thermal equilibrium. From the dependence on the delay τ between both pulses the recovery time T_1 can be extracted. Figure 1.6a shows an example of time-resolved emission traces as measured on Mo defects in SiC. Plotting the height of the PLE signal in the second pulse versus delay time τ reveals the exponential behavior shown in Fig 1.6b.

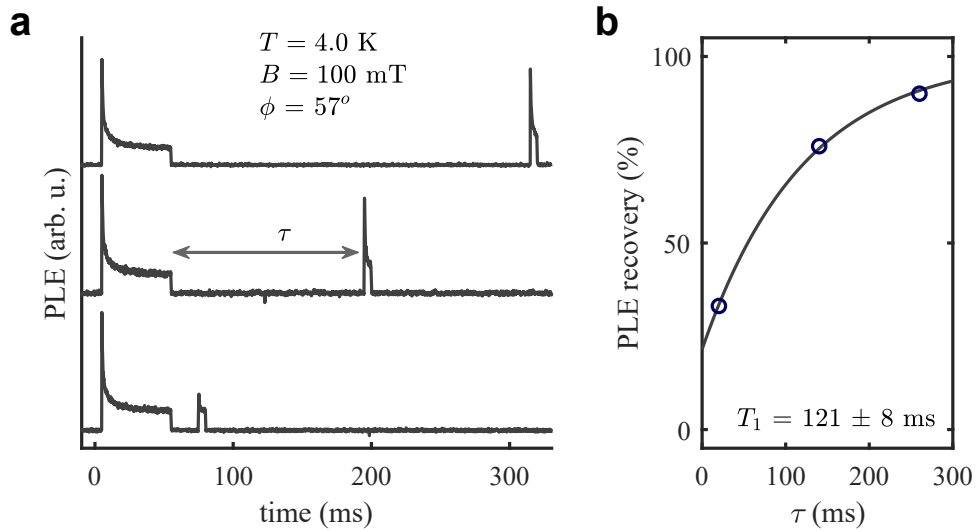

Figure 1.6: Time-resolved PLE measurement for Mo in 6H-SiC. a) Time-dependent traces of the PLE signal for three different delays τ between a first pulse (50 ms) and a second pulse (5 ms). **b)** Recovery of the initial spike in PLE response for the second pulse, relative to the first pulse, here plotted for the delay time values of **b)**. The time constant T_1 is extracted from an exponential fit (black trace).

1.5 Main achievements and thesis outline

As an outline for the remainder of this thesis the main achievements presented in each chapter are listed below.

Chapter 2 We present a study of the fine structure of molybdenum impurities in SiC, for both the 4H and 6H polytypes. Initially, we set out to confirm the expected the $S = 1$ spin-triplet character of the ground state using a two-laser magnetospectroscopy method. However, our experimental results led us to conclude that both the ground and excited state behave as spin $S = 1/2$ doublets. These findings revealed the opportunity to establish CPT in two-laser spectroscopy, from which we extracted the ensemble-averaged spin-coherence time $T_2^* = 0.3$ μs.

Chapter 3 As a follow up we studied the spin-flip time T_1 in Mo defects in 6H-SiC. The results reached exceeded expectations with T_1 times beyond seconds at a temperature of 2 K. We conducted a careful analysis, studying how couplings of the 6H-SiC environment to the Mo defect affect the spin-flip time and showed how these findings can be generalized to other transition-metal impurities in SiC.

Chapter 4 Next, we assessed divacancy defects in 4H-SiC. Specifically, we studied and demonstrated the occurrence of EIT in this system with spin $S = 1$ triplet ground-state. Spin pumping to additional levels outside the Λ schemes would, under normal circumstances, severely limit the possibility of establishing this phenomenon. However, by careful tuning of the magnetic field strength and direction, EIT could still be shown. We uncovered that the rich level structure of the divacancy in SiC also allows for a more intricate form of EIT: double EIT, with two separate transparency windows.

Chapter 5 Finally, we considered silicon carbide's potential as an integrated optoelectronic device platform. We fabricated planar waveguide structures in 4H-SiC by controlling the doping of core and cladding layers. We demonstrated the functionality of these devices and found that the losses are below 16 dB/cm, which is low enough for use in on-chip photonic applications.

References

[1] Matsunami, H. & Kimoto, T. Step-controlled epitaxial growth of SiC: High quality homoepitaxy. *Mater. Sci. Eng. R Rep.* **20**, 125–166 (1997).

[2] Celii, F. & Butler, J. Diamond chemical vapor deposition. *Annu. Rev. Phys. Chem.* **42**, 643–684 (1991).

[3] Kunz, R. & Dietrich, R. Coated silicon carbide abrasive grain (1991). US Patent 5,009,675.

[4] Domergue, J.-M., Georges, J.-M. & Laxague, M. Friction element in composite carbon/carbon-silicon carbide material and method for manufacturing same (2001). US Patent 6,221,475.

[5] Bhatnagar, M., McLarty, P. K. & Baliga, B. Silicon-carbide high-voltage (400 V) Schottky barrier diodes. *IEEE Electron Device Lett.* **13**, 501–503 (1992).

[6] Shenoy, J. N., Cooper, J. & Melloch, M. R. High-voltage double-implanted power MOSFET's in 6H-SiC. *IEEE Electron Device Lett.* **18**, 93–95 (1997).

[7] Dobrovitski, V., Fuchs, G., Falk, A., Santori, C. & Awschalom, D. Quantum control over single spins in diamond. *Annu. Rev. Condens. Matter Phys.* **4**, 23–50 (2013).

[8] Childress, L. & Hanson, R. Diamond NV centers for quantum computing and quantum networks. *MRS Bull.* **38**, 134–138 (2013).

[9] Magnusson, B. & Janzén, E. Optical characterization of deep level defects in SiC. *Mater. Sci. Forum* **483**, 341–346 (2005).

[10] Son, N. *et al.* Divacancy in 4H-SiC. *Phys. Rev. Lett.* **96**, 055501 (2006).

[11] Koehl, W. F., Buckley, B. B., Heremans, F. J., Calusine, G. & Awschalom, D. D. Room temperature coherent control of defect spin qubits in silicon carbide. *Nature* **479**, 84–87 (2011).

[12] Von Bardeleben, H., Cantin, J., Rauls, E. & Gerstmann, U. Identification and magneto-optical properties of the NV center in 4 H-SiC. *Phys. Rev. B* **92**, 064104 (2015).

[13] Widmann, M. *et al.* Coherent control of single spins in silicon carbide at room temperature. *Nat. Mater.* **14**, 164–168 (2015).

[14] Csóré, A., Gällström, A., Janzén, E. & Gali, Á. Investigation of Mo defects in 4H-SiC by means of density functional theory. *Mater. Sci. Forum* **858**, 261–264 (2016).

[15] Spindlberger, L. *et al.* Optical Properties of Vanadium in 4H Silicon Carbide for Quantum Technology. *Phys. Rev. Appl.* **12**, 014015 (2019).

[16] Scarani, V. *et al.* The security of practical quantum key distribution. *Rev. Mod. Phys.* **81**, 1301 (2009).

[17] Schirhagl, R., Chang, K., Loretz, M. & Degen, C. L. Nitrogen-vacancy centers in diamond: nanoscale sensors for physics and biology. *Annu. Rev. Phys. Chem.* **65**, 83–105 (2014).

[18] Saddow, S. E. *et al.* Single-crystal silicon carbide: A biocompatible and hemocompatible semiconductor for advanced biomedical applications. *Mater. Sci. Forum* **679**, 824–830 (2011).

[19] Zhao, Y., Wu, C., Ham, B.-S., Kim, M. & Awad, E. Microwave induced transparency in ruby. *Phys. Rev. Lett.* **79**, 641 (1997).

[20] Baur, J., Kunzer, M. & Schneider, J. Transition metals in SiC polytypes, as studied by magnetic resonance techniques. *Phys. Status Solidi A* **162**, 153–172 (1997).

[21] Pensl, G. & Choyke, W. Electrical and optical characterization of SiC. *Physica B Condens. Matter* **185**, 264–283 (1993).

[22] Tairov, Y. M. & Tsvetkov, V. General principles of growing large-size single crystals of various silicon carbide polytypes. *J. Cryst. Growth* **52**, 146–150 (1981).

[23] Duan, L.-M., Lukin, M., Cirac, J. I. & Zoller, P. Long-distance quantum communication with atomic ensembles and linear optics. *Nature* **414**, 413–418 (2001).

[24] Awschalom, D. D., Hanson, R., Wrachtrup, J. & Zhou, B. B. Quantum technologies with optically interfaced solid-state spins. *Nat. Photonics* **12**, 516–527 (2018).

[25] Bredol, M., Leers, D., Bosselaar, L. & Hutjens, M. Improved model for OH absorption in optical fibers. *J. Light. Technol.* **8**, 1536–1540 (1990).

[26] Buck, J. A. *Fundamentals of optical fibers*, vol. 50 (John Wiley & Sons, 2004).

[27] Dréau, A., Tcheborateva, A., El Mahdaoui, A., Bonato, C. & Hanson, R. Quantum frequency conversion of single photons from a nitrogen-vacancy center in diamond to telecommunication wavelengths. *Phys. Rev. Appl.* **9**, 064031 (2018).

[28] Rozpędek, F. *et al.* Near-term quantum-repeater experiments with nitrogen-vacancy centers: Overcoming the limitations of direct transmission. *Phys. Rev. A* **99**, 052330 (2019).

[29] Jobez, P. *et al.* Coherent spin control at the quantum level in an ensemble-based optical memory. *Phys. Rev. Lett.* **114**, 230502 (2015).

[30] Fox, M. *Optical properties of solids* (Oxford University Press, Oxford, 2010).

[31] Fleischhauer, M., Imamoglu, A. & Marangos, J. P. Electromagnetically induced transparency: Optics in coherent media. *Rev. Mod. Phys.* **77**, 633 (2005).

[32] Zwier, O. V., OShea, D., Onur, A. R. & Van Der Wal, C. H. All-optical coherent population trapping with defect spin ensembles in silicon carbide. *Sci. Rep.* **5**, 10931 (2015).

CHAPTER 2

Identification and tunable optical coherent control of molybdenum defects in SiC

This chapter is based on: T. Bosma*, G. J. J. Lof* *et al.* Identification and tunable optical coherent control of transition-metal spins in silicon carbide. *npj Quantum Information*, **4**, 48 (2018)

Abstract

Color centers in wide-bandgap semiconductors are attractive systems for quantum technologies since they can combine long-coherent electronic spin and bright optical properties. Several suitable centers have been identified, most famously the nitrogen-vacancy defect in diamond. However, integration in communication technology is hindered by the fact that their optical transitions lie outside telecom wavelength bands. Several transition-metal impurities in silicon carbide do emit at and near telecom wavelengths, but knowledge about their spin and optical properties is incomplete. We present all-optical identification and coherent control of molybdenum-impurity spins in silicon carbide with transitions at near-infrared wavelengths. Our results identify spin $S = 1/2$ for both the electronic ground and excited state, with highly anisotropic spin properties that we apply for implementing optical control of ground-state spin coherence. Our results show optical lifetimes of $\sim$60 ns and inhomogeneous spin dephasing times of $\sim$0.3 μs, establishing relevance for quantum spin-photon interfacing.

2.1 Introduction

Electronic spins of lattice defects in wide-bandgap semiconductors have come forward as an important platform for quantum technologies[1], in particular for applications that require both manipulation of long-coherent spin and spin-photon interfacing via bright optical transitions. In recent years this field showed strong development, with demonstrations of distribution and storage of non-local entanglement in networks for quantum communication[2–6], and quantum-enhanced field-sensing[7–11]. The nitrogen-vacancy defect in diamond is the material system that is most widely used[12,13] and best characterized[14–16] for these applications. However, its zero-phonon-line (ZPL) transition wavelength (637 nm) is not optimal for integration in standard telecom technology, which uses near-infrared wavelength bands where losses in optical fibers are minimal. A workaround could be to convert photon energies between the emitter-resonance and telecom values[17–19], but optimizing these processes is very challenging.

This situation has been driving a search for similar lattice defects that do combine favorable spin properties with bright emission directly at telecom wavelength. It was shown that both diamond and silicon carbide (SiC) can host many other spin-active color centers that could have suitable properties[20–23] (where SiC is also an attractive material for its established position in the semiconductor device industry[24,25]). However, for many of these color centers detailed knowledge about the spin and optical properties is lacking. In SiC the divacancy[26–28] and silicon vacancy[10,29–31] were recently explored, and these indeed show millisecond homogeneous spin coherence times with bright ZPL transitions closer to the telecom band.

We present here a study of transition-metal impurity defects in SiC, which exist in great variety[32–37]. There is at least one case (the vanadium impurity) that has ZPL transitions at telecom wavelengths[33], around 1300 nm, but we focus here (directed by availability of lasers in our lab) on the molybdenum impurity with ZPL transitions at 1076 nm (in 4H-SiC) and 1121 nm (in 6H-SiC), which turns out to be a highly analogous system. Theoretical investigations[38], early electron paramagnetic resonance[33,39] (EPR), and photoluminescence (PL) studies[40–42] indicate that these transition-metal impurities have promising properties. These studies show that they are deep-level defects that can be in several stable charge states, each with a distinctive value for its electronic spin S and near-infrared optical transitions. Further tuning and engineering possibilities come from the fact that these impurities can be embedded in a variety of SiC polytypes (4H, 6H, etc., see Fig. 2.1a). Recent work by Koehl *et al.*[37] studied chromium

impurities in 4H-SiC using optically detected magnetic resonance. They identified efficient ZPL (little phonon-sideband) emission at 1042 nm and 1070 nm, and their charge state as neutral with an electronic spin $S = 1$ for the ground state.

Our work is an all-optical study of ensembles of molybdenum impurities in p-type 4H-SiC and 6H-SiC material. The charge and spin configuration of these impurities, and the defect configuration in the SiC lattice that is energetically favored, was until our work not yet identified with certainty. Our results show that these Mo impurities are in the $Mo^{5+}(4d^1)$ charge state (we follow here conventional notation[33]: the label 5+ indicates that of an original Mo atom 4 electrons participate in bonds with SiC and that 1 electron is transferred to the p-type lattice environment). The single remaining electron in the 4d shell gives spin $S = 1/2$ for the ground state and optically excited state that we address. While we will show later that this can be concluded from our measurements, we assume it as a fact from the beginning since this simplifies the explanation of our experimental approach.

In addition to this identification of the impurity properties, we explore whether ground-state spin coherence is compatible with optical control. Using a two-laser magneto-spectroscopy method[28,43,44], we identify the spin Hamiltonian of the $S = 1/2$ ground state and optically excited state, which behave as doublets with highly anisotropic Landé g-factors. This gives insight in how a situation with only spin-conserving transitions can be broken, and we find that we can use a weak magnetic field to enable optical transitions from both ground-state spin levels to a common excited-state level (Λ level scheme). Upon two-laser driving of such Λ schemes, we observe coherent population trapping (CPT, all-optical control of ground-state spin coherence and fundamental to operating quantum memories[45,46]). The observed CPT reflects inhomogeneous spin dephasing times comparable to that of the SiC divacancy[28,47] (near 1 μs).

In what follows, we first present our methods and results of single-laser spectroscopy performed on ensembles of Mo impurities in both SiC polytypes. Next, we discuss a two-laser method where optical spin pumping is detected. This allows for characterizing the spin sublevels in the ground and excited state, and we demonstrate how this can be extended to controlling spin coherence.

Both the 6H-SiC and 4H-SiC (Fig. 2.1a) samples were intentionally doped with Mo. There was no further intentional doping, but near-band-gap photoluminescence revealed that both materials had p-type characteristics. The Mo concentrations in the 4H and 6H samples were estimated[41,42] to be in the range 10^{15}-10^{17} cm^{-3} and 10^{14}-10^{16} cm^{-3}, respectively. The samples were cooled in a liquid-helium flow cryostat with optical access, which was

equipped with a superconducting magnet system. The setup geometry is depicted in Fig. 2.1b. The angle ϕ between the direction of the magnetic field and the c-axis of the crystal could be varied, while both of these directions were kept orthogonal to the propagation direction of excitation laser beams. In all experiments where we resonantly addressed ZPL transitions the laser fields had linear polarization, and we always kept the direction of the linear polarization parallel to the c-axis. Earlier studies [38,41,42] of these materials showed that the ZPL transition dipoles are parallel to the c-axis. For our experiments we confirmed that the photoluminescence response was clearly the strongest for excitation with linear polarization parallel to the c-axis, for all directions and magnitudes of the magnetic fields that we applied. All results presented in this work come from photoluminescence (PL) or photoluminescence-excitation (PLE) measurements. The excitation lasers were focused to a $\sim$100 μm spot in the sample. PL emission was measured from the side. A more complete description of experimental aspects is presented in the Methods section.

2.2 Results

For initial characterization of Mo transitions in 6H-SiC and 4H-SiC we used PL and PLE spectroscopy (see Methods). Figure 2.1c shows the PL emission spectrum of the 6H-SiC sample at 3.5 K, measured using an 892.7 nm laser for excitation. The ZPL transition of the Mo defect visible in this spectrum will be studied in detail throughout this work. The shaded region indicates the emission of phonon replicas related to this ZPL [41,42]. While we could not perform a detailed analysis, the peak area of the ZPL in comparison with that of the phonon replicas indicates that the ZPL carries clearly more than a few percent of the full PL emission. Similar PL data from Mo in the 4H-SiC sample, together with a study of the temperature dependence of the PL, can be found in the Appendix (Fig. A1).

For a more detailed study of the ZPL of the Mo defects, PLE was used. In PLE measurements, the photon energy of a narrow-linewidth excitation laser is scanned across the ZPL part of the spectrum, while resulting PL of phonon-sideband (phonon-replica) emission is detected (Fig. 2.1b, we used filters to keep light from the excitation laser from reaching the detector, see Methods). The inset of Fig. 2.1c shows the resulting ZPL for Mo in 6H-SiC at 1.1057 eV (1121.3 nm). For 4H-SiC we measured the ZPL at 1.1521 eV (1076.2 nm, see Appendix). Both are in close agreement with literature [41,42]. Temperature dependence of the PLE from the Mo defects in both 4H-SiC and 6H-SiC can be found in the Appendix (Fig. A2).

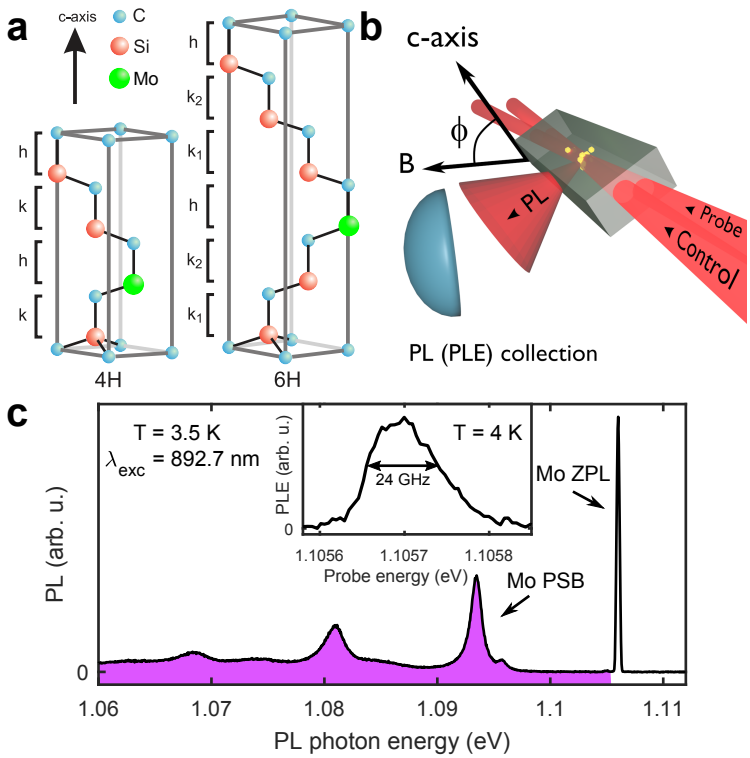

Figure 2.1: Crystal structures of SiC, setup schematic and optical signatures of Mo in 6H-SiC. a, Schematic illustration of the stacking of Si-C bilayers in the crystal structure of the 4H-SiC and 6H-SiC polytypes, which gives lattice sites with cubic and hexagonal local environment labeled by $k_{(1,2)}$ and h, respectively. Our work revisits the question whether Mo impurities are present as substitutional atoms (as depicted) or residing inside Si-C divacancies. The c-axis coincides with the growth direction. **b**, Schematic of SiC crystal in the setup. The crystal is placed in a cryostat with optical access. Laser excitation beams (control and probe for two-laser experiments) are incident on a side facet of the SiC crystal and propagate normal to the c-axis. Magnetic fields **B** are applied in a direction orthogonal to the optical axis and at angle ϕ with the c-axis. Photoluminescence (PL) is collected and detected out of another side facet of the SiC crystal. **c**, PL from Mo in 6H-SiC at 3.5 K and zero field, resulting from excitation with an 892.7 nm laser, with labels identifying the zero-phonon-line (ZPL, at 1.1057 eV) emission and phonon replicas (shaded and labeled as phonon sideband, PSB). The inset shows the ZPL as measured by photoluminescence excitation (PLE). Here, the excitation laser is scanned across the ZPL peak and emission from the PSB is used for detection.

The width of the ZPL is governed by the inhomogeneous broadening of the electronic transition throughout the ensemble of Mo impurities, which is typically caused by nonuniform strain in the crystal. For Mo in 6H-SiC we observe a broadening of 24 ± 1 GHz FWHM, and 23 ± 1 GHz for 4H-SiC. This inhomogeneous broadening is larger than the anticipated electronic spin splittings[33], and it thus masks signatures of spin levels in optical transitions between the ground and excited state.

In order to characterize the spin-related fine structure of the Mo defects, a two-laser spectroscopy technique was employed[28,43,44]. We introduce this for the four-level system sketched in Fig. 2.2a. A laser fixed at frequency f_0 is resonant with one possible transition from ground to excited state (for the example in Fig. 2.2a $|g_2\rangle$ to $|e_2\rangle$), and causes PL from a sequence of excitation and emission events. However, if the system decays from the state $|e_2\rangle$ to $|g_1\rangle$, the laser field at frequency f_0 is no longer resonantly driving optical excitations (the system goes dark due to optical pumping). In this situation, the PL is limited by the (typically long) lifetime of the $|g_1\rangle$ state. Addressing the system with a second laser field, in frequency detuned from the first by an amount δ, counteracts optical pumping into off-resonant energy levels if the detuning δ equals the splitting Δ_g between the ground-state sublevels. Thus, for specific two-laser detuning values corresponding to the energy spacings between ground-state and excited-state sublevels the PL response of the ensemble is greatly increased. Notably, this technique gives a clear signal for sublevel splittings that are smaller than the inhomogeneous broadening of the optical transition, and the spectral features now reflect the homogeneous linewidth of optical transitions[28,47].

In our measurements a 200 μW continuous-wave control and probe laser were made to overlap in the sample. For investigating Mo in 6H-SiC the control beam was tuned to the ZPL at 1121.32 nm ($f_{\text{control}} = f_0 = 267.3567$ THz), the probe beam was detuned from f_0 by a variable detuning δ (*i.e.* $f_{\text{probe}} = f_0 + \delta$). In addition, a 100 μW pulsed 770 nm re-pump laser was focused onto the defects to counteract bleaching of the Mo impurities due to charge-state switching[28,48,49] (which we observed to only occur partially without re-pump laser). All three lasers were parallel to within 3° inside the sample. A magnetic field was applied to ensure that the spin sublevels were at non-degenerate energies. Finally, we observed that the spectral signatures due to spin disappear in a broad background signal above a temperature of ~10 K (Fig. S4), and we thus performed measurements at 4 K (unless stated otherwise).

Figure 2.2b shows the dependence of the PLE on the two-laser detuning for the 6H-SiC sample (4H-SiC data in Appendix Fig. A6), for a range of magnitudes of the magnetic field (here aligned close to parallel with the c-

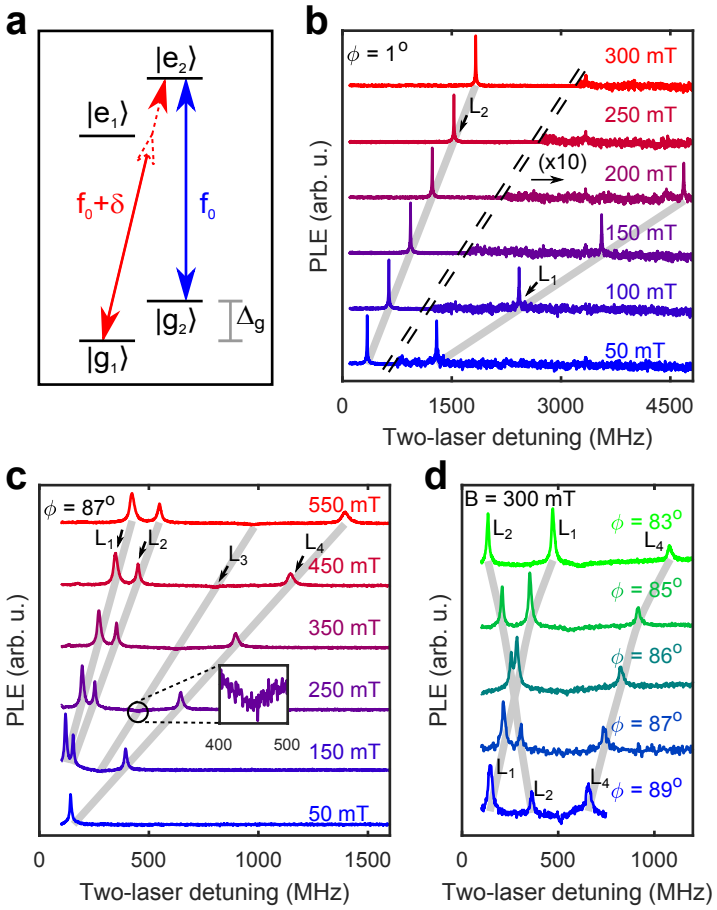

Figure 2.2: Two-laser spectroscopy results for Mo in 6H-SiC. **a**, Working principle of two-laser spectroscopy: one laser at frequency f_0 is resonant with the $|g_2\rangle$-$|e_2\rangle$ transition, the second laser is detuned from the first laser by δ. If δ is such that the second laser becomes resonant with another transition (here sketched for $|g_1\rangle$-$|e_2\rangle$) the photoluminescence will increase since optical spin-pumping by the first laser is counteracted by the second and vice versa. **b-d**, Photoluminescence excitation (PLE) signals as a function of two-laser detuning at 4 K. **b**, Magnetic field dependence with field parallel to the c-axis ($\phi = 1°$). For clarity, data in the plot have been magnified by a factor 10 right from the dashed line. Two peaks are visible, labeled L_1 and L_2 (the small peak at 3300 MHz is an artefact from the Fabry-Pérot interferometer in the setup). **c**, Magnetic field dependence with the field nearly perpendicular to the c-axis ($\phi = 87°$). Three peaks and a dip (enlarged in the inset) are visible. These four features are labeled L_1 through L_4. The peak positions as a function of field in **b-c** coincide with straight lines through the origin (within 0.2% error). **d**, Angle dependence of the PLE signal at 300 mT (angles accurate within 2°). Peaks L_1 and L_4 move to the left with increasing angle, whereas L_2 moves to the right. The data in **b-d** are offset vertically for clarity.

axis, $\phi = 1°$). Two emission peaks can be distinguished, labeled line L_1 and L_2. The emission (peak height) of L_2 is much stronger than that of L_1. Figure 2.2c shows the results of a similar measurement with the magnetic field nearly orthogonal to the crystal c-axis ($\phi = 87°$), where four spin-related emission signatures are visible, labeled as lines L_1 through L_4 (a very small peak feature left from L_1, at half its detuning, is an artifact that occurs due to a leakage effect in the spectral filtering that is used for beam preparation, see Methods). The two-laser detuning frequencies corresponding to all four lines emerge from the origin ($\mathbf{B} = 0$, $\delta = 0$) and evolve linearly with magnetic field (we checked this up to 1.2 T). The slopes of all four lines (in Hertz per Tesla) are smaller in Fig. 2.2c than in Fig 2b. In contrast to lines L_1, L_2 and L_4, which are peaks in the PLE spectrum, L_3 shows a dip.

In order to identify the lines at various angles ϕ between the magnetic field and the c-axis, we follow how each line evolves with increasing angle. Figure 2.2d shows that as ϕ increases, L_1, L_3, and L_4 move to the left, whereas L_2 moves to the right. Near 86°, L_2 and L_1 cross. At this angle, the left-to-right order of the emission lines is swapped, justifying the assignment of L_1, L_2, L_3 and L_4 as in Fig. 2.2b,c. The Appendix presents further results from two-laser magneto-spectroscopy at intermediate angles ϕ (section A2).

We show below that the results in Fig. 2.2 indicate that the Mo impurities have electronic spin $S = 1/2$ for the ground and excited state. This contradicts predictions and interpretations of initial results [33,38,41,42]. Theoretically, it was predicted that the defect associated with the ZPL under study here is a Mo impurity in the asymmetric split-vacancy configuration (Mo impurity asymmetrically located inside a Si-C divacancy), where it would have a spin $S = 1$ ground state with zero-field splittings of about 3 to 6 GHz [33,38,41,42]. However, this would lead to the observation of additional emission lines in our measurements. Particularly, in the presence of a zero-field splitting, we would expect to observe two-laser spectroscopy lines emerging from a nonzero detuning [28]. We have measured near zero fields and up to 1.2 T, as well as from 100 MHz to 21 GHz detuning (Appendix section A2), but found no more peaks than the four present in Fig. 2.2c. A larger splitting would have been visible as a splitting of the ZPL in measurements as presented in the inset of Fig. 2.1c, which was not observed in scans up to 1000 GHz. Additionally, a zero-field splitting and corresponding avoided crossings at certain magnetic fields would result in curved behavior for the positions of lines in magneto-spectroscopy. Thus, our observations rule out that there is a zero-field splitting for the ground-state and excited-state spin sublevels. In this case the effective spin-

Hamiltonian[50] can only take the form of a Zeeman term

$$H_{g(e)} = \mu_B g_{g(e)} \mathbf{B} \cdot \tilde{\mathbf{S}}, \tag{2.1}$$

where $g_{g(e)}$ is the g-factor for the electronic ground (excited) state (both assumed positive), μ_B the Bohr magneton, $\mathbf{B}$ the magnetic field vector of an externally applied field, and $\tilde{\mathbf{S}}$ the effective spin vector. The observation of four emission lines can be explained, in the simplest manner, by a system with spin $S = 1/2$ (doublet) in both the ground and excited state.

For such a system, Fig. 2.3 presents the two-laser optical pumping schemes that correspond to the observed emission lines L_1 through L_4. Addressing the system with the V-scheme excitation pathways from Fig. 2.3c leads to increased pumping into a dark ground-state sublevel, since two excited states contribute to decay into the off-resonant ground-state energy level while optical excitation out of the other ground-state level is enhanced. This results in reduced emission observed as the PLE dip feature of L_3 in Fig. 2.2c (for details see Appendix section A5).

We find that for data as in Fig. 2.2c the slopes of the emission lines are correlated by a set of sum rules

$$\Theta_{L3} = \Theta_{L1} + \Theta_{L2}, \tag{2.2}$$

$$\Theta_{L4} = 2\Theta_{L1} + \Theta_{L2}. \tag{2.3}$$

Here Θ_{Ln} denotes the slope of emission line L_n in Hertz per Tesla. The two-laser detuning frequencies for the pumping schemes in Fig. 2.3a-d are related in the same way, which justifies the assignment of these four schemes to the emission lines L_1 through L_4, respectively. These schemes and equations directly yield the g-factor values g_g and g_e for the ground and excited state (Appendix section A2).

We find that the g-factor values g_g and g_e strongly depend on ϕ, that is, they are highly anisotropic. While this is in accordance with earlier observations for transition metal defects in SiC[33], we did not find a comprehensive report on the underlying physical picture. In Appendix section A7 we present a group-theoretical analysis that explains the anisotropy $g_g \approx 1.7$ for $\phi = 0°$ and $g_g = 0$ for $\phi = 90°$, and similar behavior for g_e (which we also use to identify the orbital character of the ground and excited state). In this scenario the effective Landé g-factor[50] is given by

$$g(\phi) = \sqrt{\left(g_{\parallel} \cos\phi\right)^2 + (g_{\perp} \sin\phi)^2}, \tag{2.4}$$

where $g_{\parallel}$ represents the component of g along the c-axis of the silicon carbide structure and $g_{\perp}$ the component in the basal plane. Figure 2.4 shows

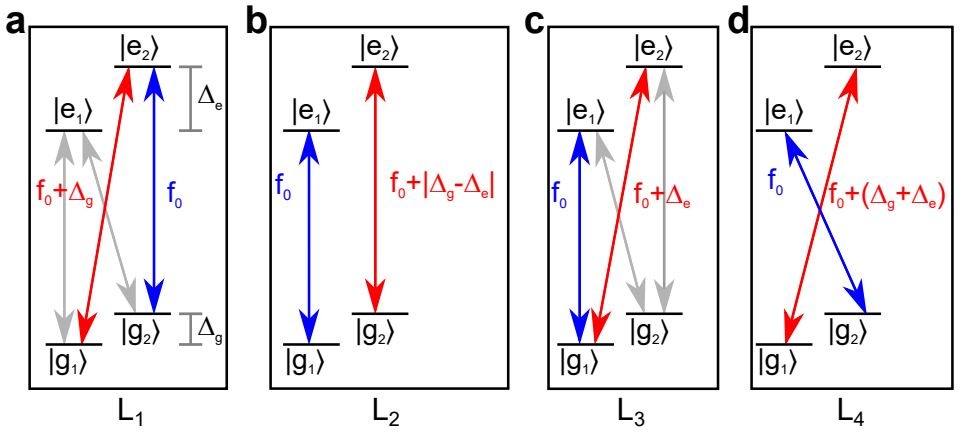

Figure 2.3: Two-laser pumping schemes with optical transitions between $S = 1/2$ ground and excited states. **a**, Λ scheme, responsible for L_1 emission feature: Two lasers are resonant with transitions from both ground states $|g_1\rangle$ (red arrow) and $|g_2\rangle$ (blue arrow) to a common excited state $|e_2\rangle$. This is achieved when the detuning equals the ground-state splitting Δ_g. The gray arrows indicate a secondary Λ scheme via $|e_1\rangle$ that is simultaneously driven in an ensemble when it has inhomogeneous values for its optical transition energies. **b**, Π scheme, responsible for L_2 emission feature: Two lasers are resonant with both vertical transitions. This is achieved when the detuning equals the difference between the ground-state and excited-state splittings, $|\Delta_g - \Delta_e|$. **c**, V scheme, responsible for L_3 emission feature: Two lasers are resonant with transitions from a common ground state $|g_1\rangle$ to both excited states $|e_1\rangle$ (blue arrow) and $|e_2\rangle$ (red arrow). This is achieved when the laser detuning equals the excited state splitting Δ_e. The gray arrows indicate a secondary V scheme that is simultaneously driven when the optical transition energies are inhomogeneously broadened. **d**, X scheme, responsible for the L_4 emission feature: Two lasers are resonant with the diagonal transitions in the scheme. This is achieved when the detuning is equal to the sum of the ground-state and the excited-state splittings, $(\Delta_g + \Delta_e)$.

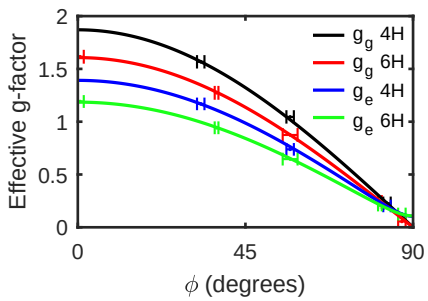

Figure 2.4: Effective g-factors for the spin of Mo impurities in SiC. Angular dependence of the g-factor for the $S = 1/2$ ground (g_g) and excited states (g_e) of the Mo impurity in 4H-SiC and 6H-SiC. The solid lines indicate fits of equation (2.4) to the data points extracted from two-laser magneto-spectroscopy measurements as in Fig. 2b,c.

the ground and excited state effective g-factors extracted from our two-laser magnetospectroscopy experiments for 6H-SiC and 4H-SiC (additional experimental data can be found in the Appendix). The solid lines represent fits to the equation (2.4) for the effective g-factor. The resulting $g_{\parallel}$ and $g_{\perp}$ parameters are given in table 1.

The reason why diagonal transitions (in Fig. 2.3 panels a,c), and thus the Λ and V scheme are allowed, lies in the different behavior of g_e and g_g. When the magnetic field direction coincides with the internal quantization axis of the defect, the spin states in both the ground and excited state are given by the basis of the S_z operator, where the z-axis is defined along the c-axis. This means that the spin-state overlap for vertical transitions, *e.g.* from $|g_1\rangle$ to $|e_1\rangle$, is unity. In such cases, diagonal transitions are forbidden as the overlap between *e.g.* $|g_1\rangle$ and $|e_2\rangle$ is zero. Tilting the magnetic field away from the internal quantization axis introduces mixing of the spin states. The amount of mixing depends on the g-factor, such that it differs for the ground and excited state. This results in a tunable non-zero overlap for all transitions, allowing all four schemes to be observed (as in Fig. 2.2b where $\phi = 87°$). This reasoning also explains the suppression of all emission lines except L_2 in Fig. 2.2b, where the magnetic field is nearly along the c-axis. A detailed analysis of the relative peak heights in Fig. 2.2b-c compared to wave function overlap can be found in the Appendix (section A4).

The Λ driving scheme depicted in Fig. 2.3a, where both ground states are coupled to a common excited state, is of particular interest. In such cases it is possible to achieve all-optical coherent population trapping (CPT) [45], which is of great significance in quantum-optical operations that use ground-state spin coherence. This phenomenon occurs when two lasers address a Λ system

at exact two-photon resonance, *i.e.* when the two-laser detuning matches the ground-state splitting. The ground-state spin system is then driven towards a superposition state that approaches $|\Psi_{CPT}\rangle \propto \Omega_2 |g_1\rangle - \Omega_1 |g_2\rangle$ for ideal spin coherence. Here Ω_n is the Rabi frequency for the driven transition from the $|g_n\rangle$ state to the common excited state. Since the system is now coherently trapped in the ground state, the photoluminescence decreases.

In order to study the occurrence of CPT, we focus on the two-laser PLE features that result from a Λ scheme. A probe field with variable two-laser detuning relative to a fixed control laser was scanned across this line in frequency steps of 50 kHz, at 200 μW. The control laser power was varied between 200 μW and 5 mW. This indeed yields signatures of CPT, as presented in Fig. 2.5. A clear power dependence is visible: when the control beam power is increased, the depth of the CPT dip increases (and can fully develop at higher laser powers or by concentrating laser fields in SiC waveguides[47]). This observation of CPT confirms our earlier interpretation of lines L_1-L_4, in that it confirms that L_1 results from a Λ scheme. It also strengthens the conclusion that this system is $S = 1/2$, since otherwise optical spin-pumping into the additional (dark) energy levels of the ground state would be detrimental for the observation of CPT.

Using a standard model for CPT[45], adapted to account for strong inhomogeneous broadening of the optical transitions[47] (see also Appendix section A6) we extract an inhomogeneous spin dephasing time T_2^* of 0.32 ± 0.08 μs and an optical lifetime of the excited state of 56 ± 8 ns. The optical lifetime is about a factor two longer than that of the nitrogen-vacancy defect in diamond[12,51], indicating that the Mo defects can be applied as bright emitters (although we were not able to measure their quantum efficiency). The value of T_2^* is relatively short but sufficient for applications based on CPT[45]. Moreover, the EPR studies by Baur *et al.*[33] on various transition-metal impurities show that the inhomogeneity probably has a strong static contribution from an effect linked to the spread in mass for Mo isotopes in natural abundance (nearly absent for the mentioned vanadium case), compatible with elongating spin coherence via spin-echo techniques. In addition, their work showed that the hyperfine coupling to the impurity nuclear spin can be resolved. There is thus clearly a prospect for storage times in quantum memory applications that are considerably longer than T_2^*.

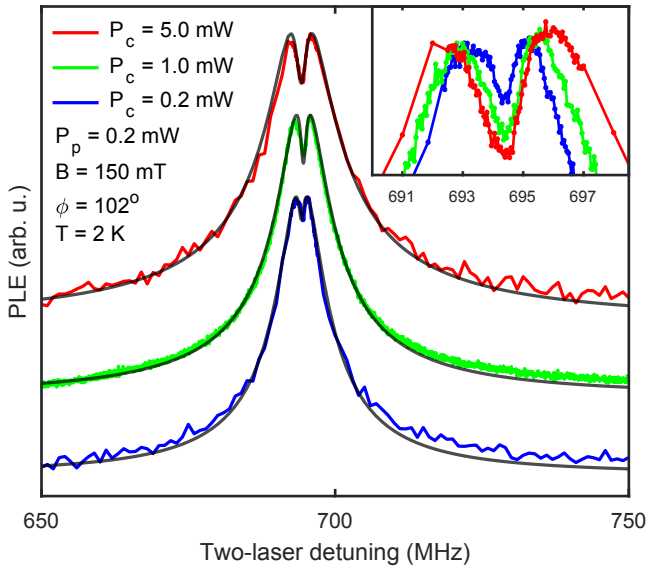

Figure 2.5: Signatures of coherent population trapping of Mo spin states in 6H-SiC. Two-laser spectroscopy of the L_1 peak in the PLE signals reveals a dipped structure in the peak at several combinations of probe-beam and control-beam power. This results from coherent population trapping (CPT) upon Λ-scheme driving. Temperature, magnetic field orientation and magnitude, and laser powers, were as labeled. The data are offset vertically for clarity. Solid lines are fits of a theoretical model of CPT (see main text). The inset shows the normalized CPT feature depths.

2.3 Discussion

The anisotropic behavior of the g-factor that we observed for Mo was also observed for vanadium and titanium in the EPR studies by Baur *et al.*[33] (they observed $g_{\parallel} \approx 1.7$ and $g_{\perp} = 0$ for the ground state). In these cases the transition metal has a single electron in its 3d orbital and occupies the hexagonal (h) Si substitutional site. We show in Appendix section A7 that the origin of this behavior can be traced back to a combination of a crystal field with C_{3v} symmetry and spin-orbit coupling for the specific case of an ion with one electron in its d-orbital.

The correspondence of this behavior with what we observe for the Mo impurity identifies that our materials have Mo impurities present as $Mo^{5+}(4d^1)$ systems residing on a hexagonal h silicon substitutional site. In this case of a hexagonal (h) substitutional site, the molybdenum is bonded in a tetrahedral geometry, sharing four electrons with its nearest neighbors. For $Mo^{5+}(4d^1)$ the defect is then in a singly ionized $+|e|$ charge state (e denotes the elementary charge), due to the transfer of one electron to the p-type SiC host material.

An alternative scenario for our type of Mo impurities was recently proposed by Ivády *et al.*[35] They proposed, based on theoretical work[35], the existence of the asymmetric split-vacancy (ASV) defect in SiC. An ASV defect in SiC occurs when an impurity occupies the interstitial site formed by adjacent silicon and carbon vacancies. The local symmetry of this defect is a distorted octahedron with a threefold symmetry axis in which the strong g-factor anisotropy ($g_{\perp} = 0$) may also be present for the $S = 1/2$ state[50]. Considering six shared electrons for this divacancy environment, the $Mo^{5+}(4d^1)$ Mo configuration occurs for the singly charged $-|e|$ state. For our observations this is a highly improbable scenario as compared to one based on the $+|e|$ state, given the p-type SiC host material used in our work. We thus conclude that this scenario by Ivády *et al.* does not occur in our material. Interestingly, niobium defects have been shown to grow in this ASV configuration[52], indicating there indeed exist large varieties in the crystal symmetries involved with transition metal defects in SiC. This defect displays $S = 1/2$ spin with several optical transitions between $892 - 897$ nm in 4H-SiC and $907 - 911$ nm in 6H-SiC[52].

Another defect worth comparing to is the aforementioned chromium defect, studied by Koehl *et al.*[37] Like Mo in SiC, the Cr defect is located at a silicon substitutional site, thus yielding a $3d^2$ configuration for this defect in its neutral charge state. The observed $S = 1$ spin state has a zero-field splitting parameter of 6.7 GHz[37]. By employing optically detected magnetic resonance techniques they measured an inhomogeneous spin coherence time

T_2^* of 37 ns[37], which is considerably shorter than observed for molybdenum in the present work. Regarding spin-qubit applications, the exceptionally low phonon-sideband emission of Cr seems favorable for optical interfacing. However, the optical lifetime for this Cr configuration (146 μs[37]) is much longer than that of the Mo defect we studied, hampering its application as a bright emitter. It is clear that there is a wide variety in optical and spin properties throughout transition-metal impurities in SiC, which makes up a useful library for engineering quantum technologies with spin-active color centers.

2.4 Conclusion

We have studied ensembles of molybdenum defect centers in 6H and 4H silicon carbide with 1.1521 eV and 1.1057 eV transition energies, respectively. The ground-state and excited-state spin of both defects was determined to be $S = 1/2$ with large g-factor anisotropy. Since this is allowed in hexagonal symmetry, but forbidden in cubic, we find this to be consistent with theoretical descriptions that predict that Mo resides at a hexagonal lattice site in 4H-SiC and 6H-SiC[35,38], and our p-type host environment strongly suggests that this occurs for Mo at a silicon substitutional site. We used the measured insight in the $S = 1/2$ spin Hamiltonians for tuning control schemes where two-laser driving addresses transitions of a Λ system, and observed CPT for such cases. This demonstrates that the Mo defect and similar transition-metal impurities are promising for quantum information technology. In particular for the highly analogous vanadium color center, engineered to be in SiC material where it stays in its neutral $V^{4+}(3d^1)$ charge state, this holds promise for combining $S = 1/2$ spin coherence with operation directly at telecom wavelengths.

2.5 Experimental methods

Materials The samples used in this study were ∼1 mm thick epilayers grown with chemical vapor deposition, and they were intentionally doped with Mo during growth. The PL signals showed that a relatively low concentration of tungsten was present due to unintentional doping from metal parts of the growth setup (three PL peaks near 1.00 eV, outside the range presented in Fig. 2.1a). The concentration of various types of (di)vacancies was too low to be observed in the PL spectrum that was recorded. For more details see Ref. [42].

Cryostat During all measurements, the sample was mounted in a helium

flow cryostat with optical access through four windows and equipped with a superconducting magnet system.

Photoluminescence (PL) The PL spectrum of the 6H-SiC sample was measured by exciting the material with an 892.7 nm laser, and using a double monochromator equipped with infrared-sensitive photomultiplier. For the 4H-SiC sample, we used a 514.5 nm excitation laser and an FTIR spectrometer.

Photoluminescence Excitation (PLE) The PLE spectrum was measured by exciting the defects using a CW diode laser tunable from 1050 nm to 1158 nm with linewidth below 50 kHz, stabilized within 1 MHz using feedback from a HighFinesse WS-7 wavelength meter. The polarization was linear along the sample c-axis. The laser spot diameter was ∼100 μm at the sample. The PL exiting the sample sideways was collected with a high-NA lens, and detected by a single-photon counter. The peaks in the PLE data were typically recorded at a rate of about 10 kcounts/s by the single-photon counter. We present PLE count rates in arb. u. since the photon collection efficiency was not well defined, and it varied with changing the angle ϕ. For part of the settings we placed neutral density filters before the single-photon counter to keep it from saturating. The excitation laser was filtered from the PLE signals using a set of three 1082 nm (for the 4H-SiC case) or 1130 nm (for the 6H-SiC case) longpass interference filters. PLE was measured using an ID230 single-photon counter. Additionally, to counter charge state switching of the defects, a 770 nm re-pump beam from a tunable pulsed Ti:sapphire laser was focused at the same region in the sample. Laser powers as mentioned in the main text.

Two-laser characterization The PLE setup described above was modified by focusing a detuned laser beam to the sample, in addition to the present beams. The detuned laser field was generated by splitting off part of the stabilized diode laser beam. This secondary beam was coupled into a single-mode fiber and passed through an electro-optic phase modulator in which an RF signal (up to ∼5 GHz) modulated the phase. Several sidebands were created next to the fundamental laser frequency, the spacing of these sidebands was determined by the RF frequency. Next, a Fabry-Pérot interferometer was used to select one of the first-order sidebands (and it was locked to the selected mode). The resulting beam was focused on the same region in the sample as the original PLE beams (diode laser and re-pump) with similar spot size and polarization along the sample c-axis. Laser powers were as mentioned in the main text. Small rotations of the c-axis with respect to the magnetic field were performed using a piezo-actuated goniometer with 7.2 degrees travel.

Data processing For all graphs with PLE data a background count rate

is subtracted from each line, determined by the minimum value of the PLE in that line (far away from resonance features). After this a fixed vertical offset is added for clarity. For each graph, the scaling is identical for all lines within that graph.

Data availability The data sets generated and analyzed during the current study are available from the corresponding author upon reasonable request.

Acknowledgments

We thank A. Gali for discussions and M. de Roosz, J. G. Holstein, T. J. Schouten and H. Adema for technical support. Early discussions with Prof. Erik Janzén leading to initiation of this study are gratefully acknowledged. Financial support was provided by ERC Starting Grant 279931, the Zernike Institute BIS program, the Swedish Research Council grants VR 2016-04068 and VR 2016-05362, and the Carl-Trygger Stiftelse för Vetenskaplig Forskning grant CTS 15:339.

Author contributions

The project was initiated by C.H.W., O.V.Z, I.G.I and N.T.S. SiC materials were grown and prepared by A.E. and B.M. Experiments were performed by T.B., G.J.J.L. and O.V.Z, except for the PL measurements which were done by A.G. and I.G.I. Data analysis was performed by T.B., G.J.J.L., C.G., O.V.Z., F.H., R.W.A.H. and C.H.W. T.B., G.J.J.L. and C.H.W. had the lead on writing the paper, and T.B. and G.J.J.L. are co-first author. All authors read and commented on the manuscript.

References

[1] Gao, W., Imamoglu, A., Bernien, H. & Hanson, R. Coherent manipulation, measurement and entanglement of individual solid-state spins using optical fields. *Nat. Phot.* **9**, 363 (2015).

[2] Togan, E. *et al.* Quantum entanglement between an optical photon and a solid-state spin qubit. *Nature* **466**, 730 (2010).

[3] Dolde, F. *et al.* High-fidelity spin entanglement using optimal control. *Nat. Commun.* **5**, 3371 (2014).

[4] Klimov, P. V., Falk, A. L., Christle, D. J., Dobrovitski, V. V. & Awschalom, D. D. Quantum entanglement at ambient conditions in a macroscopic solid-state spin ensemble. *Sci. Adv.* **1**, e1501015 (2015).

[5] Hensen, B. *et al.* Loophole-free Bell inequality violation using electron spins separated by 1.3 kilometres. *Nature* **526**, 682–686 (2015).

[6] Kalb, N. *et al.* Entanglement distillation between solid-state quantum network nodes. *Science* **356**, 928–932 (2017).

[7] Budker, D. & Romalis, M. Optical magnetometry. *Nat. Phys.* **3**, 227–234 (2007).

[8] Balasubramanian, G. *et al.* Nanoscale imaging magnetometry with diamond spins under ambient conditions. *Nature* **455**, 648–651 (2008).

[9] Dolde, F. *et al.* Electric-field sensing using single diamond spins. *Nat. Phys.* **7**, 459–463 (2011).

[10] Kraus, H. *et al.* Magnetic field and temperature sensing with atomic-scale spin defects in silicon carbide. *Sci. Rep.* **4**, 5303 (2014).

[11] Bonato, C. *et al.* Optimized quantum sensing with a single electron spin using real-time adaptive measurements. *Nat. Nanotechnol.* **11**, 247–252 (2016).

[12] Dobrovitski, V., Fuchs, G., Falk, A., Santori, C. & Awschalom, D. Quantum control over single spins in diamond. *Annu. Rev. Condens. Matter Phys.* **4**, 23–50 (2013).

[13] Childress, L. & Hanson, R. Diamond NV centers for quantum computing and quantum networks. *MRS Bull.* **38**, 134–138 (2013).

[14] Doherty, M. W., Manson, N. B., Delaney, P. & Hollenberg, L. C. The negatively charged nitrogen-vacancy centre in diamond: the electronic solution. *New J. Phys.* **13**, 025019 (2011).

[15] Maze, J. *et al.* Properties of nitrogen-vacancy centers in diamond: the group theoretic approach. *New J. Phys.* **13**, 025025 (2011).

[16] Thiering, G. & Gali, A. Ab initio calculation of spin-orbit coupling for an NV center in diamond exhibiting dynamic Jahn-Teller effect. *Phys. Rev. B* **96**, 081115 (2017).

[17] Radnaev, A. *et al.* A quantum memory with telecom-wavelength conversion. *Nat. Phys.* **6**, 894–899 (2010).

[18] Zaske, S. *et al.* Visible-to-telecom quantum frequency conversion of light from a single quantum emitter. *Phys. Rev. Lett.* **109**, 147404 (2012).

[19] Dréau, A., Tcheborateva, A., El Mahdaoui, A., Bonato, C. & Hanson, R. Quantum frequency conversion of single photons from a nitrogen-vacancy center in diamond to telecommunication wavelengths. *Phys. Rev. Appl.* **9**, 064031 (2018).

[20] Weber, J. *et al.* Quantum computing with defects. *Proc. Natl. Acad. Sci. U.S.A.* **107**, 8513 (2010).

[21] Weber, J. *et al.* Defects in SiC for quantum computing. *J. Appl. Phys.* **109**, 102417 (2011).

[22] Von Bardeleben, H. *et al.* NV centers in 3C, 4H, and 6H silicon carbide: A variable platform for solid-state qubits and nanosensors. *Phys. Rev. B* **94**, 121202 (2016).

[23] Zargaleh, S. *et al.* Evidence for near-infrared photoluminescence of nitrogen vacancy centers in 4H-SiC. *Phys. Rev. B* **94**, 060102 (2016).

[24] Friedrichs, P., Kimoto, T., Ley, L. & Pensl, G. *Silicon Carbide*, vol. 1 (Wiley, Weinheim, 2010).

[25] Song, B.-S., Yamada, S., Asano, T. & Noda, S. Demonstration of two-dimensional photonic crystals based on silicon carbide. *Opt. Express* **19**, 11084–11089 (2011).

[26] Koehl, W. F., Buckley, B. B., Heremans, F. J., Calusine, G. & Awschalom, D. D. Room temperature coherent control of defect spin qubits in silicon carbide. *Nature* **479**, 84–87 (2011).

[27] Christle, D. J. *et al.* Isolated electron spins in silicon carbide with millisecond coherence times. *Nat. Mater.* **14**, 160 (2015).

[28] Zwier, O. V., O'Shea, D., Onur, A. R. & van der Wal, C. H. All–optical coherent population trapping with defect spin ensembles in silicon carbide. *Sci. Rep.* **5**, 10931 (2015).

[29] Riedel, D. *et al.* Resonant addressing and manipulation of silicon vacancy qubits in silicon carbide. *Phys. Rev. Lett.* **109**, 226402 (2012).

[30] Kraus, H. *et al.* Room-temperature quantum microwave emitters based on spin defects in silicon carbide. *Nat. Phys.* **10**, 157 (2014).

[31] Widmann, M. *et al.* Coherent control of single spins in silicon carbide at room temperature. *Nat. Mater.* **14**, 164 (2015).

[32] Hobgood, H. M. *et al.* Semi–insulating 6H-SiC grown by physical vapor transport. *Appl. Phys. Lett.* **66**, 1364 (1995).

[33] Baur, J., Kunzer, M. & Schneider, J. Transition metals in SiC polytypes, as studied by magnetic resonance techniques. *Phys. Status Solidi A* **162**, 153–172 (1997).

[34] Magnusson, B. & Janzén, E. Optical characterization of deep level defects in SiC. *Mater. Sci. Forum* **483**, 341–346 (2005).

[35] Ivády, V., Gällström, A., Son, N. T., Janzén, E. & Gali, A. Asymmetric split-vacancy defects in SiC polytypes: A combined theoretical and electron spin resonance study. *Phys. Rev. Lett.* **107**, 195501 (2011).

[36] Son, N. T. *et al.* Electron paramagnetic resonance and theoretical studies of Nb in 4H-and 6H-SiC. *J. Appl. Phys.* **112**, 083711 (2012).

[37] Koehl, W. F. *et al.* Resonant optical spectroscopy and coherent control of Cr4+ spin ensembles in SiC and GaN. *Phys. Rev. B* **95**, 035207 (2017).

[38] Csóré, A., Gällström, A., Janzén, E. & Gali, Á. Investigation of Mo defects in 4H-SiC by means of density functional theory. *Mater. Sci. Forum* **858**, 261–264 (2016).

[39] Dombrowski, K. *et al.* Identification of molybdenum in 6H-SiC by magnetic resonance techniques. *Phys. Rev. B* **54**, 7323 (1996).

[40] Kimoto, T., Nakajima, T., Matsunami, H., Nakata, T. & Inoue, M. Formation of semi-insulating 6H-SiC layers by vanadium ion implantations. *Appl. Phys. Lett.* **69**, 1113 (1996).

[41] Gällström, A., Magnusson, B. & Janzén, E. Optical identification of Mo related deep level defect in 4H and 6H SiC. *Mater. Sci. Forum* **615**, 405–408 (2009).

[42] Gällström, A. *Optical characterization of deep level defects in SiC*. PhD dissertation No. 1674, ISSN 0345-7524 (Linköping University, 2015).

[43] Manson, N. & Wei, C. Transient hole burning in NV centre in diamond. *J. Lumin.* **58**, 158–160 (1994).

[44] Santori, C. *et al.* Coherent population trapping in diamond NV centers at zero magnetic field. *Opt. Express* **14**, 7986–7994 (2006).

[45] Fleischhauer, M., Imamoglu, A. & Marangos, J. P. Electromagnetically induced transparency: Optics in coherent media. *Rev. Mod. Phys.* **77**, 633 (2005).

[46] Kimble, H. J. The quantum internet. *Nature* **453**, 1023 (2008).

[47] Zwier, O. V. *Two-laser spectroscopy and coherent manipulation of color-center spin ensembles in silicon carbide*. Zernike Institute PhD thesis series, ISSN 1570-1530 (University of Groningen, 2016).

[48] Beha, K., Batalov, A., Manson, N. B., Bratschitsch, R. & Leitenstorfer, A. Optimum photoluminescence excitation and recharging cycle of single nitrogen-vacancy centers in ultrapure diamond. *Phys. Rev. Lett.* **109**, 097404 (2012).

[49] Wolfowicz, G. *et al.* Optical charge state control of spin defects in 4H-SiC. *Nat. Commun.* **8**, 1876 (2017).

[50] Abragam, A. & Bleaney, B. *Electron Paramagnetic Resonance Of Transition Ions*. International series of monographs on physics (Clarendon Press, Oxford, 1970).

[51] Doherty, M. W. *et al.* The nitrogen-vacancy colour centre in diamond. *Phys. Rep.* **528**, 1–45 (2013).

[52] Gällström, A. *et al.* Optical properties and Zeeman spectroscopy of niobium in silicon carbide. *Phys. Rev. B* **92**, 075207 (2015).

[53] Fox, M. *Optical properties of solids* (Oxford University Press, Oxford, 2010).

[54] Ivády, V. *et al.* Transition Metal Defects in Cubic and Hexagonal Polytypes of SiC: Site Selection, Magnetic and Optical Properties from ab initio Calculations. *Mater. Sci. Forum* **717**, 205–210 (2012).

[55] Chibotaru, L. F., Hendrickx, M. F., Clima, S., Larionova, J. & Ceulemans, A. Magnetic anisotropy of [Mo (CN) 7] 4-anions and fragments of cyano-bridged magnetic networks. *J. Phys. Chem. A* **109**, 7251–7257 (2005).

[56] Kunzer, M., Müller, H. & Kaufmann, U. Magnetic circular dichroism and site-selective optically detected magnetic resonance of the deep amphoteric vanadium impurity in 6H-SiC. *Phys. Rev. B* **48**, 10846 (1993).

[57] Dietz, R., Kamimura, H., Sturge, M. & Yariv, A. Electronic structure of copper impurities in ZnO. *Phys. Rev.* **132**, 1559 (1963).

Appendix

2.A1 Single-laser spectroscopy

Figure 2.A6 shows the photoluminescence (PL) emission spectrum of the 4H-SiC sample at 5 and 20 K, characterized using a 514.5 nm excitation laser. The Mo zero-phonon line (ZPL) at 1.1521 eV is marked by a dashed box and shown enlarged in the inset. The broader peaks at lower energies are phonon replicas of the ZPL. There is almost no dependence on temperature for both the ZPL and the phonon replicas.

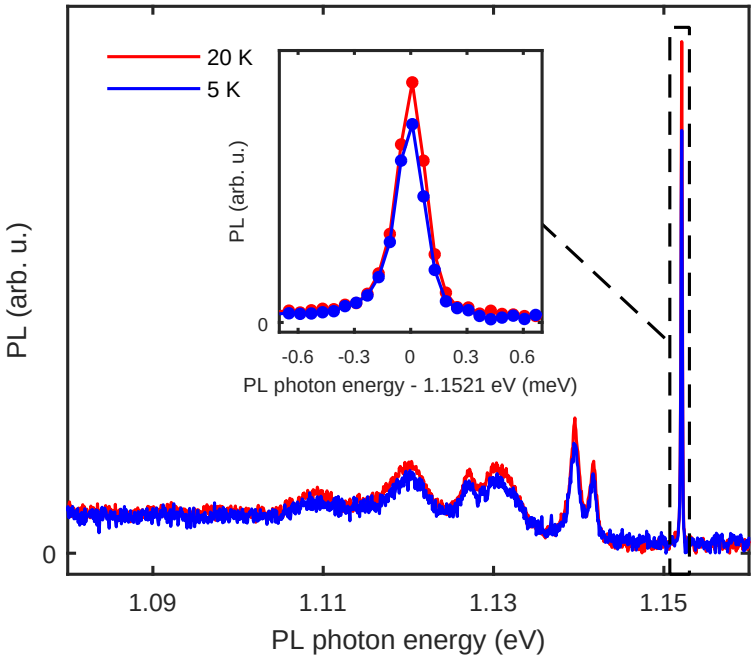

Figure 2.A6: Temperature dependence of Mo PL spectrum in 4H-SiC. PL from excitation with a 514.5 nm laser, for 5 and 20 K sample temperatures. The dashed box marks the ZPL at 1.1521 eV. The inset gives a magnified view of the ZPL. The broader peaks at lower photon energies are phonon replicas of the ZPL.

Figures 2.A7a,b show results of PLE measurements of the ZPL for Mo in 4H-SiC at 1.1521 eV and 6H-SiC at 1.1057 eV, and the temperature dependence of these PLE signals. In both measurements a remnant magnetic field of a few millitesla is present in the superconducting magnet system. When the temperature is decreased, the width of the ZPL stays roughly the same, but its height drops significantly. Combined with the near-

independence on temperature of the emission spectrum in Fig. 2.A6, this is an indication for optical spin pumping for Mo-impurity states at lower temperatures, where a single resonant laser pumps then the system into long-lived off-resonant spin states.

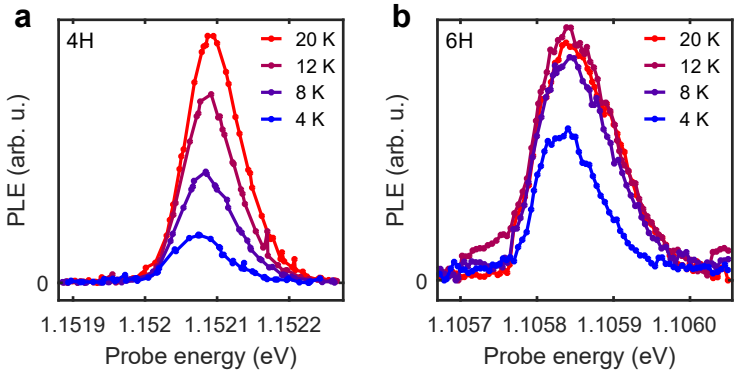

Figure 2.A7: Temperature dependence of the PLE signals from the Mo ZPL in 4H-SiC and 6H-SiC. PLE signals from scanning a single CW narrow-linewidth laser across the ZPL photon-energy range. The temperature was varied between 4 and 20 K. The ZPL for Mo in (**a**) 4H-SiC is at 1.1521 eV, and for Mo in (**b**) 6H-SiC at 1.1057 eV. In both measurements a remnant magnetic field of a few mT is present in the superconducting magnet system.

2.A2 Additional two-laser spectroscopy for Mo in 6H-SiC

Angle dependence. In addition to Fig. 2.2b,c in the main text, we also measured the magnetic field dependence of the spin related emission signatures at intermediate angles ϕ. Figure 2.A8 shows this dependence for $\phi = 37°$, $57°$ and $81°$. The spectroscopic position of emission lines L_n show a linear dependence on magnetic field, with slopes Θ_{Ln} (in Hertz per Tesla) that decrease as ϕ increases. The effective g-factors in Fig. 2.4 are acquired from the emission lines by relating their slopes to the Zeeman splittings in the ground and excited state. Using the four pumping schemes depicted in Fig. 2.3 in the main text, we derive

$$\Theta_{L1} = \frac{\mu_B}{h} g_g, \tag{2.5}$$

$$\Theta_{L2} = \frac{\mu_B}{h} |g_e - g_g|, \tag{2.6}$$

$$\Theta_{L3} = \frac{\mu_B}{h} g_e, \tag{2.7}$$

$$\Theta_{L4} = \frac{\mu_B}{h} \left(g_e + g_g\right), \tag{2.8}$$

where h is Planck's constant, μ_B the Bohr magneton and $g_{g(e)}$ the ground (excited) state g-factor.

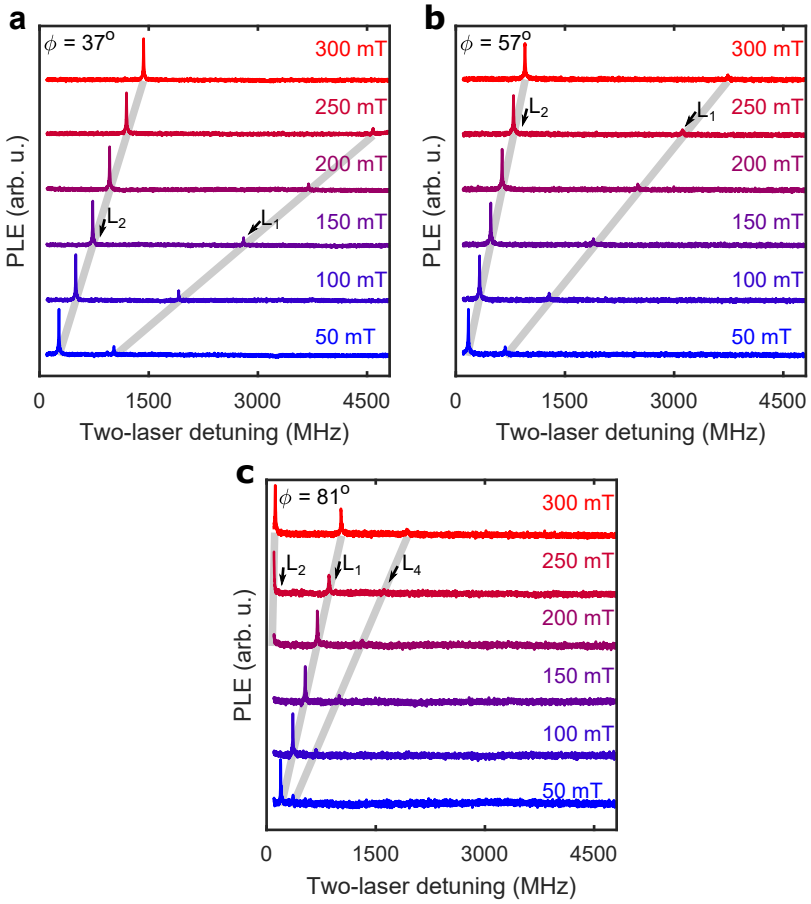

Figure 2.A8: Magneto-spectroscopy of two-laser spin signatures in PLE from Mo in 6H-SiC. Magnetic field dependence of the PLE signal as a function of two-laser detuning, for angles ϕ between the magnetic field and c-axis set to $\phi = 37°$ (**a**), $\phi = 57°$ (**b**) and $\phi = 81°$ (**c**). Results for the temperature at 4 K. The labeling of the emission lines (L_1 - L_4) is consistent with Fig. 2.2. The data are offset vertically for clarity.

Temperature and photon-energy dependence. We also measured the dependence of the two-laser PLE signal on temperature, see Fig. 2.A9a. The PLE features disappear above 8 K in a much broader PLE background that starts to emit because of more rapid thermal spin mixing in the ground state. Other Mo systems in the ensemble for which the two-laser resonance

condition is not met then also start emitting due to single-laser excitation (see also Fig. 2.A7), since the optical pumping into an off-resonant state becomes shorter lived. Notably, the linewidths of the peaks in Fig. 2.A9a do not change in the range 2 K to 8 K, indicating that the temperature does not affect the optical lifetime in this range. Above 8 K the temperature was a bit unstable during the measurements, which causes the drifting in the single-laser PLE contribution to this signal. Interestingly, the dip (L_3) is most pronounced at 6 K, since there are several competing processing responsible for this dip (see section 2.A5).

Additionally, we measured how the two-laser PLE occurred throughout the inhomogenously broadened ensemble, by varying the photon energy of the control laser and sweeping the two-laser detuning for each case (Fig. 2.A9b). For all photon energies the peaks are at the same position, indicating that all Mo atoms in the ensemble behave similarly. At 1.10561 eV the control laser is too far detuned from the ZPL to yield any two-laser PLE signal.

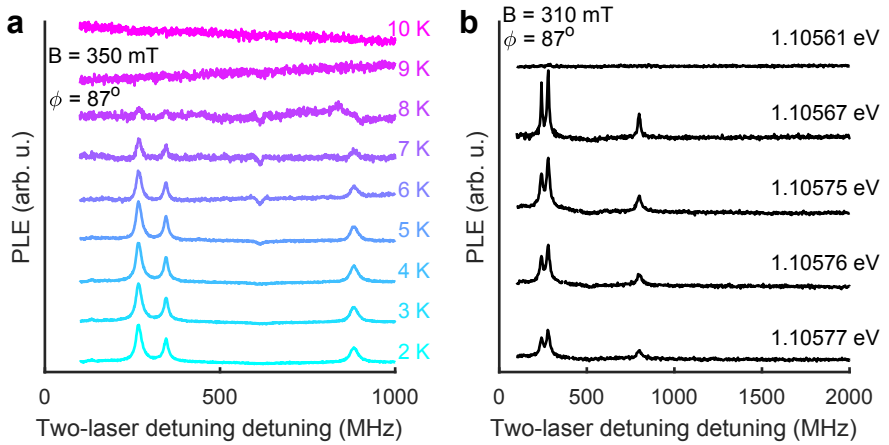

Figure 2.A9: Temperature and photon-energy dependence of two-laser emission features in 6H-SiC. Temperature (**a**) and laser photon-energy (**b**) dependence of the PLE signal as a function of two-laser detuning. Results are offset vertically for clarity.

Two-laser spectroscopy for the 5-21 GHz detuning range. In order to check for a possible presence of spin-related emission features at detunings larger than 5 GHz (checking for a possible zero-field splitting), we modified the setup such that we could control two-laser detunings up to 21 GHz. The electro-optical phase modulator (EOM) we used for generating the detuned

laser field could generate first-order sidebands up to 7 GHz. In order to check for two-laser spectroscopy emission features at larger detunings, we removed the Fabry-Pérot (FP) resonator that had the role of filtering out a single sideband. Now, all sidebands (on the same optical axis) were focused onto the sample with 2 mW total laser power. Apart from the re-pump beam, no additional laser was focused onto the sample in this experiment. In this way, the Mo defects could interact with several combinations of sidebands. Figure 2.A10a shows the spectral content of this beam (here characterized by still using the FP resonator). The first and second order sidebands at negative and positive detuning take a significant portion of the total optical power. Hence, pairs of sidebands spaced by single, double or triple frequency intervals (EOM frequency f_{EOM}) now perform two-laser spectroscopy on the Mo defects. The relevant sideband spacings are indicated in Fig. 2.A10a.

Figure 2.A10b presents results of these measurements, showing various peaks that we identified and label as $L_{n,m}$. Here n is identifying the peak as a line L_n as in the main text, while the label m identifies it as a spectroscopic response for two-laser detuning at $m \cdot f_{\mathrm{EOM}}$ (that is, $m = 1$ is for first-order EOM sideband spacing, *etc.*). Note that second-order manifestations of the known peaks L_1-L_4 (from double sideband spacings, labeled as $L_{n,2}$) are now visible at $\frac{1}{2} f_{\mathrm{EOM}}$, and third-order response of the known L_1-L_4 occurs at $\frac{1}{3} f_{\mathrm{EOM}}$ (but for preserving clarity these have not been labeled in Fig. 2.A10b).

Figure 2.A10c depicts a continuation of this experiment with f_{EOM} up to 7 GHz with the same resolution as Fig. 2.A10b. No new peaks are observed. Considering that third-order peaks were clearly visible before, we conclude that no additional two-laser emission features exist up to 21 GHz.

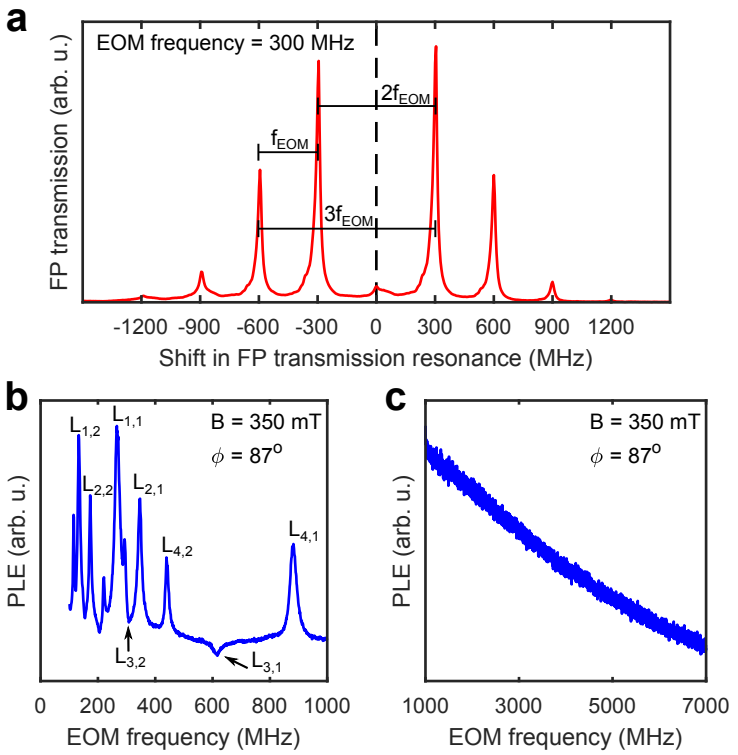

Figure 2.A10: Two-laser spin signatures of Mo in 6H-SiC at large detuning. **a**, Transmission scan of the Fabry-Pérot resonator, characterizing which optical frequencies are present in the beam after passing through the electro-optical modulator (EOM). The first-order sidebands at ±300 MHz have the highest intensity, whereas the fundamental laser frequency is suppressed (but not fully removed) by the EOM. Relevant sideband spacings are indicated. **b**, Spin signatures at low two-laser detuning. PLE is increased when two sidebands are appropriately detuned from each other. Emission features similar to those in Fig. 2.2c of the main text are visible, and labeled $L_{n,m}$ (see main text of this section). **c**, The PLE signal from two-laser spectroscopy at larger detuning. No peaked features from single, double or triple sideband spacings are visible.

2.A3 Two-laser spectroscopy for Mo in 4H-SiC

We also studied the spin-related fine structure of Mo defects in 4H-SiC. Our 4H-SiC sample suffered from large background absorption, which drastically lowered the signal-to-noise ratio. We relate this absorption to a larger impurity content (of unknown character, but giving broad-band absorption) in our 4H-SiC material as compared to our 6H-SiC material. Therefore, the lasers were incident on a corner of the sample, so as to minimize the decay

of the emitted PL. We present the results in gray-scale plots in Fig. 2.A11 for optimized contrast. The figure shows the magnetic field and two-laser detuning dependence of the PLE.

Analogous to Fig. 2.2 for 6H-SiC in the main text, the spectroscopic position features appear as straight lines that emerge from zero detuning, indicating the absence of a zero-field splitting. When the magnetic field is nearly perpendicular to the c-axis (Fig. 2.A11c), four lines are visible. This is consistent with an $S = 1/2$ ground and excited state.

The data from Fig. 2.A11c was measured at 10 K, whereas Fig. 2.A11a,b was at 4.2 K. At 10 K, all emission lines become dips, while for 6H-SiC only the V system shows a dip. The temperature dependence of L_3 and L_1 is shown in Fig. 2.A12 for the same configuration as in Fig. 2.A11c ($\phi = 83°$). At low temperatures L_1 shows a peak and L_3 shows a dip. Upon increasing the temperature, both features become dips. This phenomenon was only observed for Mo in 4H-SiC, it could not be seen in 6H-SiC. We therefore conclude that this probably arises from effects where Mo absorption and emission is influenced by the large background absorption in the 4H-SiC material.

The labels in Fig. 2.A11 are assigned based on the sum rules from equation (2.2) and (2.3) (main text), which indeed also hold for the observed emission lines observed here. Like in the main text, L_1 through L_4 indicate Λ, Π, V and X two-laser pumping schemes, respectively. The L_1 and L_3 labels are interchangeable in Fig. 2.A11c when only considering the sum rules. However, the fact that the left feature in Fig. 2.A12 shows a dip for all temperatures means that it should be related to a V scheme. Thus, the current assignment of the labels with corresponding pumping schemes is justified. Using equations 2.5 through 2.8, the effective g-factors can be determined. Fitting these to equation (2.4) gives the values for $g_{\parallel}$ and $g_{\perp}$ reported in the main text.

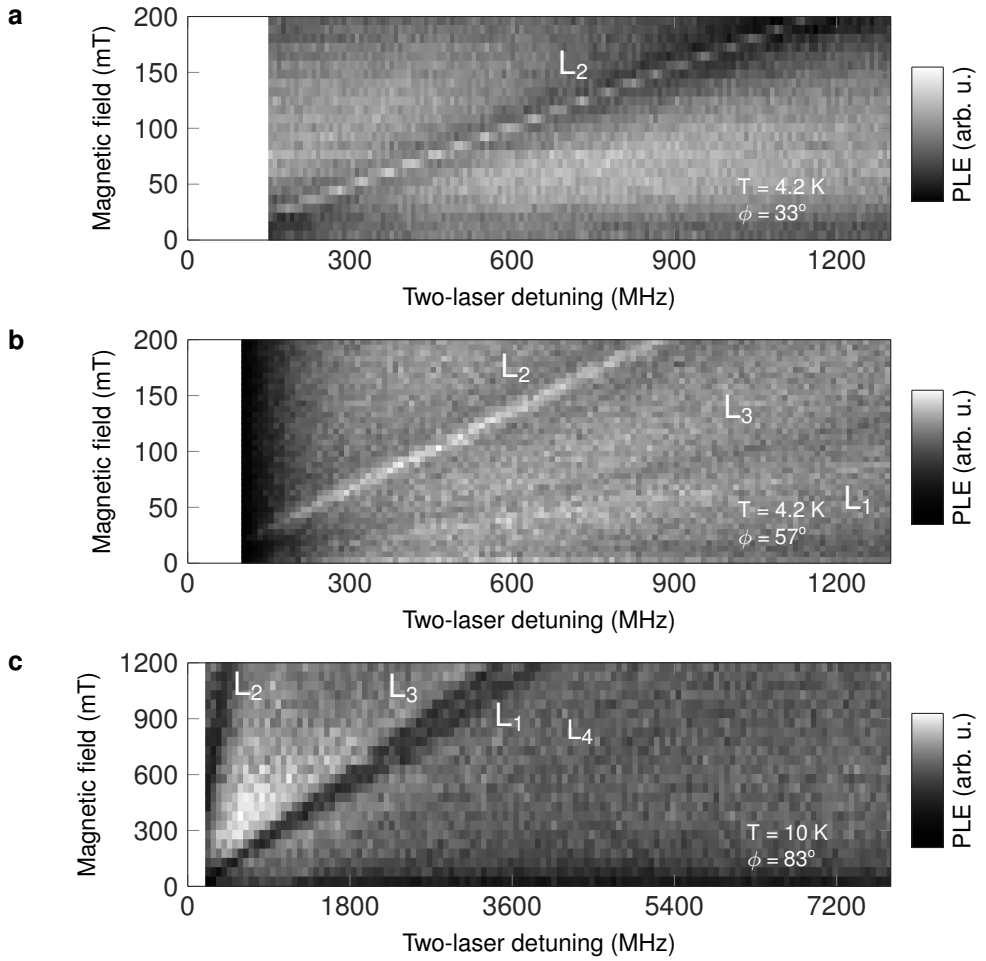

Figure 2.A11: Two-laser spin signatures of Mo in 4H-SiC. PLE signal as a function of two-laser detuning and magnetic field strength, for various angles ϕ between the magnetic field and c-axis. **a**, Measurement at 4.2 K, with $\phi = 33°$. A single emission line (peak) is visible, labeled L_2. **b**, Measurement at 4.2 K, with $\phi = 57°$. Three emission lines are visible, labeled L_1, L_2 (peaks), and L_3 (dip). **c**, Measurement at 10 K, with $\phi = 83°$. Four emission lines are visible, labeled L_1 through L_4 (all dips). Note that the measurement range of **c** is six time as large as **a** and **b**, but the plot aspect ratio is the same. The labeling is consistent with the main text. A gray-scale plot has been used for optimal contrast.

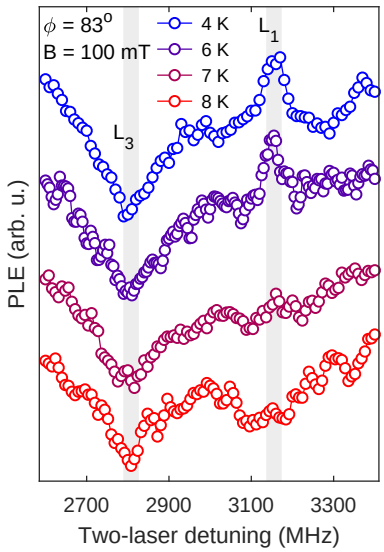

Figure 2.A12: Temperature dependence of PLE spin signatures from Mo in 4H-SiC. PLE signal as a function of two-laser detuning and temperature with magnetic field at $\phi = 83°$ from the sample c-axis at 100 mT. As the temperature increases, the signal from L_1 changes from a peak to a broad dip, while L_3 remains a dip. The labeling is consistent with the main text.

2.A4 Franck-Condon principle with respect to spin

The amplitude of the two-laser emission signatures is determined by the strength of the underlying optical transitions. For a transition $|g_i\rangle$-$|e_j\rangle$, this strength is determined by the spin overlap $\langle g_i|e_j\rangle$, according to the Franck-Condon principle with respect to spin [53]. The quantum states of the spin in the electronic ground and excited state can be described using effective spin Hamiltonian

$$H_{g(e)} = \mu_B \mathbf{B} \cdot \mathbf{g}_{g(e)} \cdot \tilde{\mathbf{S}}, \tag{2.9}$$

with μ_B the Bohr magneton, $\mathbf{B}$ the applied magnetic field vector, $\tilde{\mathbf{S}}$ the effective spin vector, and where the ground (excited) state g-parameter is a tensor $\mathbf{g}_{g(e)}$. Using Cartesian coordinates this can be written as

$$\mathbf{g}_{g(e)} = \begin{pmatrix} g_{\perp}^{g(e)} & 0 & 0 \\ 0 & g_{\perp}^{g(e)} & 0 \\ 0 & 0 & g_{\parallel}^{g(e)} \end{pmatrix}. \tag{2.10}$$

Here the z-axis is parallel to the SiC c-axis, and the x and y-axes lay in the plane perpendicular to the c-axis. Due to the symmetry of the defect, the magnetic field $\mathbf{B}$ can be written as

$$\mathbf{B} = \begin{pmatrix} 0 \\ B\sin\phi \\ B\cos\phi \end{pmatrix}, \tag{2.11}$$

where B indicates the magnitude of the magnetic field. The resulting Hamiltonian $H_{g(e)}$ may be found by substituting $\mathbf{B}$ and $\mathbf{g}_{g(e)}$ into equation (2.9), and considering that $S = 1/2$. The basis of $H_{g(e)}$ can be found from the eigenvectors.

For the ground state $g_{\perp}^{g}$ is zero, thus the bases of H_g and S_z coincide, independent of ϕ. Therefore, there is no mixing of spins in the ground state. However, in the excited state $g_{\perp}^{e}$ is nonzero, causing its eigenbasis to rotate if a magnetic field is applied non-parallel to the c-axis. The new eigenbasis is a linear combination of eigenstates of S_x, S_y and S_z, such that there will be mixing for spins in the excited state for any nonzero angle ϕ.

We calculate the spin overlap for the $|g_i\rangle$-$|e_j\rangle$ transition from the inner product of two basis states $|g_i\rangle$ and $|e_j\rangle$. The strength of a two-laser pumping scheme is then the product of the strength of both transitions. For example, the strength of the Λ scheme from Fig. 2.3a equals the inner product $\langle g_1|e_2\rangle$ multiplied by $\langle g_2|e_2\rangle$. The resulting strengths for all four pumping schemes are depicted in Fig. 2.A13.

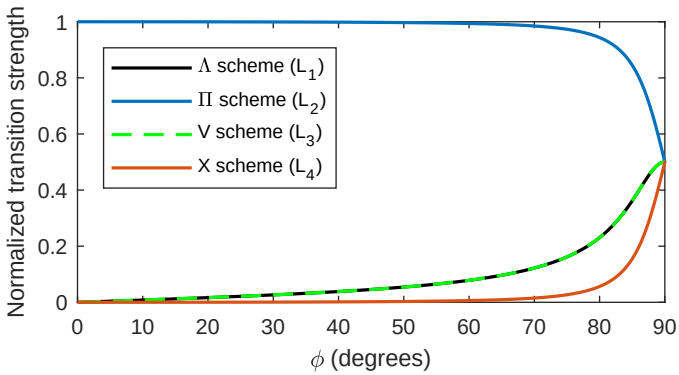

Figure 2.A13: Two-laser pumping scheme transition strengths. For each scheme the product of the spin overlaps from both underlying transitions is shown. The strength of the Π scheme is near unity for large angles and never vanishes. The strengths of the Λ and V schemes are equal, they vanish at $\phi = 0°$. The X scheme strength vanishes more rapidly than any other scheme for angles ϕ close to 0°.

We now compare these transition strengths to the data in Fig. 2.2b,c and Fig. 2.A8 and 2.A11. It is clear that the Π scheme is the strongest pumping scheme for all angles $\phi \neq 90°$. This explains the large relative amplitude of L_2 in our measurements. The Λ and V scheme transition strengths are equal, starting from zero for $\phi = 0°$ and increasing as ϕ approaches 90°. For the Λ scheme, this is consistent with the increasing relative amplitude of L_1. For ϕ close to 90° the amplitude of L_1 is even larger than for L_2. The reason for this is that a Λ scheme is emitting more effectively than a Π scheme. The V scheme is harder to observe in the background emission, such that L_3 is only visible for ϕ close to 90°. Finally, the transition strength of the X scheme is only significant for ϕ close to 90°, which is why we have not been able to observe L_4 below 81° in 6H-SiC.

2.A5 V-scheme dip

Understanding the observation of a dip for the V pumping scheme in a four-level system (Fig. 2.2c in the main text) is less trivial than for the observation of peaks from the other three pumping schemes. The latter can be readily understood from the fact that for proper two-laser detuning values both ground states are addressed simultaneously, such that there is no optical pumping into dark states. In this section we will investigate how a dip feature can occur in the PLE signals. Our modeling will be based on solving a master equation in Lindblad form with a density matrix in rotating wave approximation for a four-level system with two near-resonant lasers [45].

Table 2.A1: Parameter choices for V-scheme model

parameter	value (Hz)	parameter	value (Hz)
Γ_v	$0.9 \cdot 10^7$	γ_{g1}	0
Γ_d	$0.1 \cdot 10^7$	γ_{g2}	$5 \cdot 10^6$
Γ_g	$1 \cdot 10^4$	γ_{g3}	$5 \cdot 10^6$
Γ_e	$1 \cdot 10^4$	γ_{g4}	$5 \cdot 10^6$
Δ_c	0	Ω_c	$\sqrt{.9} \cdot 10^7$
Δ_p	$\in [-500, 500] \cdot 10^6$	Ω_p	$\sqrt{.1} \cdot 10^7$

Consider the four-level system depicted in Fig. 2.A14a. A control laser is near-resonant with the $|g_1\rangle$-$|e_1\rangle$ (vertical) transition and a probe laser near-resonant with $|g_1\rangle$-$|e_2\rangle$ (diagonal) transition. Here the two-laser detuning is defined as $\delta = \Delta_p - \Delta_c$, *i.e.* the difference between the detunings Δ of both lasers from their respective near-resonant transitions, such that the emission feature appears at zero two-laser detuning. The decay rates from the excited states are Γ_v and Γ_d for vertical and diagonal transitions, respectively. They are quadratically proportional to the spin-state overlap $\langle g_i | e_j \rangle$

$$\Gamma_v \propto |\langle g_1 | e_1 \rangle|^2 , \tag{2.12}$$

$$\Gamma_d \propto |\langle g_1 | e_2 \rangle|^2 . \tag{2.13}$$

These rates are unequal, since the spin-state overlap for diagonal transitions is generally smaller than for vertical transitions (see previous section). The decay rates Γ_e between excited-state levels and Γ_g ground-state levels are assumed very small compared to the decay rates from the excited-state levels. The decay rates from ground-state levels towards the excited-state levels are set to zero. Dephasing rates are taken relative to the $|g_1\rangle$ state ($\gamma_{g1} = 0$). The choices for parameters are listed in table 2.A1. The Rabi frequencies Ω_c and Ω_p of the driven transitions are linearly proportional to the spin-state overlap

$$\Omega_c \propto |\langle g_1 | e_1 \rangle| , \tag{2.14}$$

$$\Omega_p \propto |\langle g_1 | e_2 \rangle| . \tag{2.15}$$

Additionally, we have to consider a secondary V-scheme (Fig. 2.A14b) resonant with another part of the inhomogeneously broadened ensemble. The control and probe laser are swapped, as the former now addresses a diagonal transition, while the latter addresses a vertical one. The new Rabi frequency is taken to be $\Omega_c' = \sqrt{\frac{\Gamma_d}{\Gamma_v}} \Omega_c$ for the control beam, which is now

driving a diagonal transition (with reduced strength). The probe beam is driving a vertical transition (with increased strength), and its Rabi frequency is $\Omega_p' = \sqrt{\frac{\Gamma_v}{\Gamma_d}}\Omega_p$.

Considering both V-schemes, we calculate the total population in both excited-state levels as it reflects the amount of photoluminescence resulting from decay back to the ground states. The two-laser detuning dependence of the excited-state population is shown in Fig. 2.A14c. The black curve considers both schemes simultaneously, which represents the situation in our measurements. Here the dip indeed appears, although both separate schemes (a and b) display a dip and peak (respectively). The competition between both schemes limits the depth of the observed dip, which explains our observation of shallow dips in contrast to sharp peaks in Fig. 2.2c in the main text.

Interestingly, the black curve displays a peak within the dip, which might seem like a CPT feature. However, this feature is not visible in either curve from the two separate pumping schemes. This peak appears because the peak from the second V-scheme (green) is slightly sharper than the dip from the first one (blue). The peak might still be caused by CPT, as the blunting of the dip relative to the peak can be caused by a long dephasing time of the ground state.

Key to understanding the appearance of a dip in the total photoluminescence emission is the difference in decay rates, vertical decay being favored over diagonal decay. Consider the pumping scheme from Fig. 2.A14a. When the probe laser is off-resonant the control laser drives the $|g_1\rangle$-$|e_1\rangle$ transition. Decay will occur mostly towards the $|g_1\rangle$ state and occasionally to the dark $|g_2\rangle$ state. If the probe laser becomes resonant with the $|g_1\rangle$-$|e_2\rangle$ transition, the increased population in the $|e_2\rangle$ state will prefer to decay towards the dark $|g_2\rangle$ state. The overall decay towards the dark state is now increased. The secondary pumping scheme (Fig. 2.A14b) works the other way around, where the diagonal transition is always driven by the control beam and a resonant probe beam will counteract some of the pumping into the dark state (now $|g_1\rangle$). However, the slightly increased emission from scheme b cannot fully counteract the decreased emission from scheme a (even when $\Omega_p = \Omega_c = \Omega_p' = \Omega_c'$).

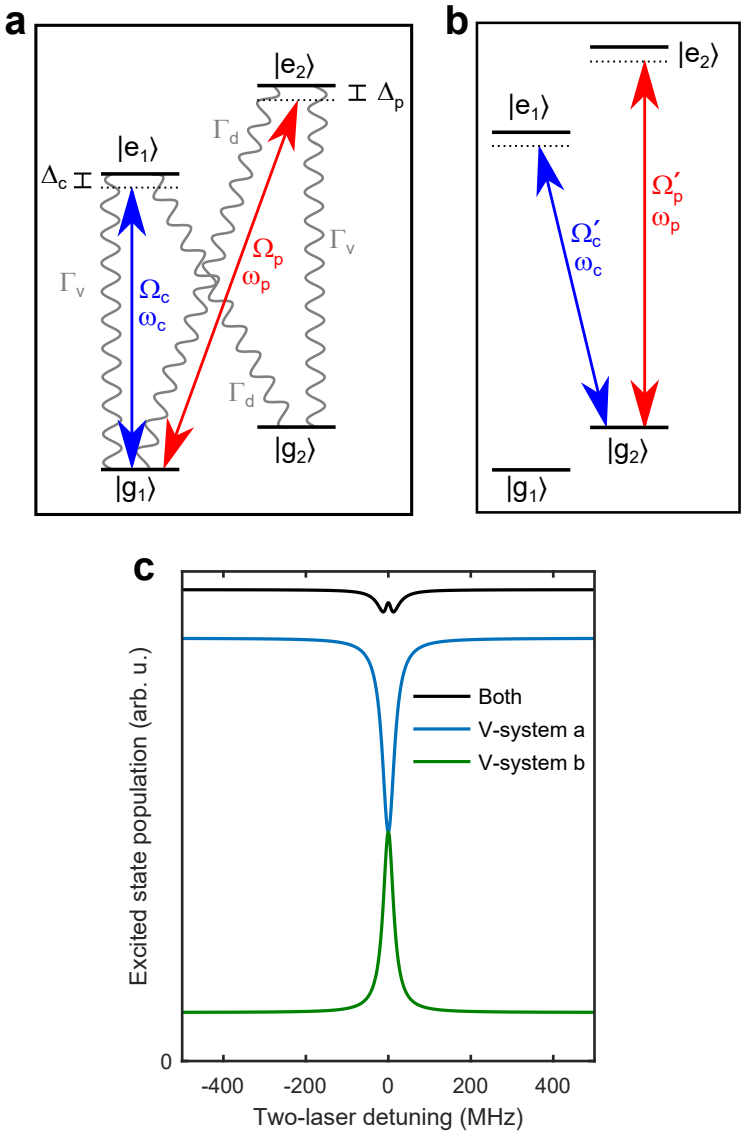

Figure 2.A14: Four-level V-scheme model. a, V pumping scheme in a four level system. Here Ω is the Rabi frequency for the control and probe lasers, and ω their (angular) frequency. Γ_v and Γ_d are the decay rates for vertical and diagonal decay, respectively. Δ represents the detuning from resonance of the control and probe beam. **b,** V-scheme simultaneously resonant (with the scheme in panel **a**) for another part of the inhomogeneously broadened ensemble. Probe and control Rabi frequencies Ω' differ from **a**, since both lasers drive other transitions with different dipole strengths. **c,** Total population in the excited-state levels ($|e_1\rangle$ and $|e_2\rangle$) for both schemes separately (blue and green) as well as their sum (black).

2.A6 Modeling of coherent population trapping

For fitting the CPT traces in Fig. 2.5 in the main text, we use a standard CPT description [45], extended for strong inhomogeneous broadening of the optical transitions, and an approach similar to the one from the previous section. However (as compared to the previous section), the behavior of CPT has a more pronounced dependence on parameters, such that almost no assumptions have to be made. When taking the spin Hamiltonians as established input (section 4), the only assumption made is that the spin relaxation time in the ground state and excited state is much slower than all other decay process. This allows for setting up fitting of the CPT traces with only two free fit parameters, which correspond to the optical lifetime and the inhomogeneous dephasing time T_2^*.

Since two lasers couple both ground-state levels to a single common excited-state level, the other excited-state level will be empty. Therefore, we may describe this situation with a three-level system, where the PL is directly proportional to the excited-state population. The decay rates and Rabi frequencies are proportional to the Franck-Condon factors for spin-state overlaps $\langle g_i|e\rangle$ in the same way as before (equations (2.12)-(2.15)). At this angle ($\phi = 102°$) we calculate these factors to be

$$\langle g_1|e\rangle = 0.9793, \tag{2.16}$$

$$\langle g_2|e\rangle = 0.2022, \tag{2.17}$$

according to the reasoning in section 2.A4. We take that the $|g_1\rangle$-$|e\rangle$ is a vertical transition and $|g_2\rangle$-$|e\rangle$ a diagonal one.

In order to account for inhomogeneous broadening throughout the ensemble, the solution of the master equation is computed for a set of control-laser detunings Δ_c (see Fig. 2.A14a) around zero, its range extending far beyond the two-laser detuning values δ (since we experimentally observed an inhomogeneous broadening much in excess of the spin splittings). In this case the probe-laser detuning becomes $\Delta_p = \Delta_c + \delta$. The resulting excited-state populations are integrated along the inhomogeneous broadening Δ_c (up to the point where the signal contribution vanishes) to give the PL emission as a function of two-laser detuning δ. Analogous to the previous section, we have to consider a secondary Λ-scheme in order to fully account for the inhomogeneous broadening. The total PL emission is found by adding together the excited-state populations from both schemes.

We fit this model to the data presented in Fig. 2.5 after subtracting a static background. We extract the inhomogeneous dephasing time $T_2^* = 0.32 \pm 0.08$ μs and an optical lifetime of 56 ± 8 ns. The errors are estimated

from the spread in extracted dephasing times and lifetimes throughout the data sets.

2.A7 Anisotropic g-factor in the effective spin-Hamiltonian

Relationship between effective spin Hamiltonian and local configuration of the defect

An effective spin-Hamiltonian as the one used in the main text is a convenient tool which allows us to describe the behavior of the system in a wide range of configurations, as long as the effective parameters are experimentally determined and all relevant states are considered. It is often the meeting point between experimentalists, who measure the relevant parameters, and theoreticians, who attempt to correlate them to the Hamiltonian that describes the configuration of the system. A careful description of the latter, and how it modifies the parameters at hand, allows us to rationalize our choices when investigating defects with varying characteristics (such as a different charge state or element). This task is more approachable when we consider the group-theoretical properties of the system at hand. Here we combine group-theoretical considerations with ligand field theory in order to qualitatively describe the features observed in our experiment. In particular, we aim at explaining the large Zeeman splitting anisotropy observed in both ground and excited states, and correlating it to the charge and spatial configuration of the defect.

In our experiments, we observe a single zero-phonon line (ZPL) associated with optical transitions between two Kramers doublets (KD, doublets whose degeneracy is protected by time-reversal symmetry and is thus broken in the presence of a magnetic field) in defects which contain Mo. The presence of a single zero-phonon line in both 4H and 6H-SiC samples indicates that the defect occupies a lattice site with hexagonal symmetry. The lattice of 6H-SiC has two inequivalent sites with cubic symmetry. Thus, if the defect were to occupy sites of cubic symmetry, we would expect to observe two ZPLs closely spaced in this sample. The absence of the ZPL associated with this defect in samples of 3C-SiC[54] further corroborates this assumption. Additionally, we observe strong anisotropy in the Zeeman splitting of the ground and excited states. Specifically, when the magnetic field is perpendicular to the symmetry axis of the crystal, the Zeeman splitting of the ground state goes to zero, whereas that of the excited state is very small. This feature is observed in other transition-metal defects in SiC situated at Si substitutional sites of hexagonal symmetry and with one electron in its 3d orbital[33], but we are not aware of a clear explanation of

the phenomenon.

In our experiments, we observed transitions between sublevels of doubly degenerate ground and excited states, whose degeneracy is broken in the presence of a magnetic field. Thus, we note that ground and excited states are isolated KDs, indicating that the defect contains an odd number of electrons. A Mo atom has 6 electrons in its valence shell. The atom can occupy a Si substitutional site (Mo_{Si}), where it needs to bond to 4 neighboring atoms, or an asymmetric split vacancy (ASV) site ($Mo_{V_{Si}-V_C}$), where it bonds to 6 neighboring atoms. These defects can, respectively, be described by a Mo ion in the configurations $4d^2$ and $4d^0$, indicating that the defect must be ionized in order to contain an odd number of electrons. Its charge state, which could be ±1, ±3, *etc.*, is determined by the Fermi level in the crystal of interest. We note that the ZPL could only be observed in p-doped samples, which indicates that the features investigated here are unlikely to arise from negatively charged defect. The defect Mo_{Si}^{+1} (where +1 represents the charge state of the defect, not the Mo atom) can be approximately described by a Mo in a configuration $4d^1$, which facilitates the treatment of its configuration in terms of d orbitals. In contrast, the defect $Mo_{V_{Si}-V_C}^{+1}$ is described by an electronic configuration containing a hole in the bonding orbitals. These orbitals show strong hybridization between the d orbitals of the Mo and the orbitals of the ligands, and cannot be straightforwardly analyzed using the formalism described below. Nonetheless, inspired by the similarities between our system and other transition-metal defects reported in SiC[33], we investigate the effect of the crystal field of C_{3v} symmetry –which is expected to be significant in hexagonal lattice sites in 4H-SiC and 6H-SiC– on the one-electron levels of the 5 sublevels (10, if spin multiplicity is included) of the 4d shell of a Mo atom. We qualitatively predict the spin-hamiltonian parameters expected for a Mo ion in a $4d^1$ configuration, and compare our analysis to the experimental results.

Ion in $4d^1$ configuration in the presence of crystal field of C_{3v} symmetry and spin-orbit coupling

The 5 degenerate sublevels of a 4d-orbital are split by a crystal field of C_{3v} symmetry[50]. The energy splittings induced by this field are much smaller than the energy difference between the 4d shell and the next orbital excited state (5s). This allows us to, initially, consider the 5 orbitals of the 4d shell as a complete set. Since Mo is a heavy atom, we cannot disregard the effect of spin-orbit interaction. However, we assume that the crystal field is larger than the effect of SOC, that is, $\Delta E_{free} \gg \Delta E_{crystal} \gg \Delta E_{spin-orbit} \gg \Delta E_{Zeeman}$, where ΔE denotes the energy splitting induced by each term

(see Fig. 2.A15).

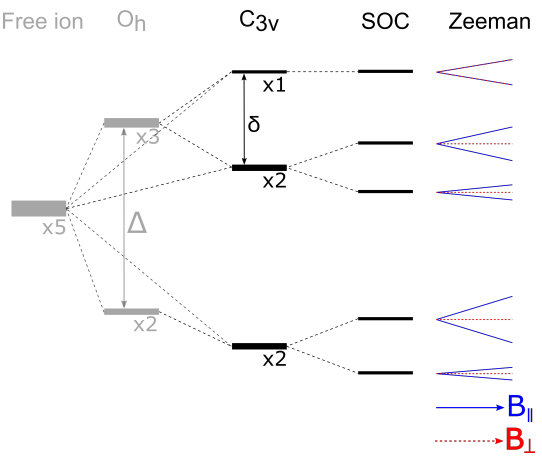

Figure 2.A15: Splitting of one-electron energy levels of a 4d orbital, under the action of a crystal field and spin-orbit coupling. In the free atom, the 5 orbitals corresponding to the 4d shell (disregarding the spin) are degenerate. A crystal field of cubic symmetry breaks this degeneracy, generating an orbital triplet and a doublet, whereas a crystal field of C_{3v} symmetry, splits the 5 orbitals into one singlet and two doublets. In the text, we focus on a crystal field of C_{3v} symmetry, and disregard the cubic term. Although we recognize that this is an approximation, we argue that this approach clarifies the physics governing the strong magnetic anisotropy observed, and is thus justified. Spin-orbit coupling is responsible for splitting the doublets, generating in total 5 sets of Kramers doublets (here, the spin of the electron is taken into account). The energy splittings caused by a magnetic field within these KD give rise to the effective spin Hamiltonian parameters considered. We note that a group-theoretical approach alone is not capable of providing the order of the energy levels shown in the figure. We take this order to be the one observed in transition-metal defects in a tetrahedral crystal field with strong trigonal distortion [50].

The 5 orbital states of the d-orbital form a 5-dimensional irreducible representation (irrep) of the full rotation group SO(3). When the symmetry is lowered by the crystal field to C_{3v}, the 5-dimensional representation is split into 2 doublets (E_1, E_2) and 1 singlet (A) that are irreps of C_{3v}. Writing the 5 components of the 4d orbital in terms of the quadratic functions z^2, x^2-y^2, xy, xz, yz allows us to identify which orbitals are degenerate in the presence of a crystal field of trigonal symmetry. We find that the singlet A is composed of the orbital $4d_{z^2}$. Furthermore, the orbitals $4d_{xz}$ and $4d_{yz}$ are degenerate upon action of the crystal field and make up doublet E_1. Finally the orbitals $4d_{x^2-y^2}$ and $4d_{xy}$ correspond to doublet E_2. Group-theoretical considerations alone are not capable of elucidating which irrep corresponds

to the ground state, that is, it does not provide information about the order of the energy levels.

Comparison between the Cartesian form of these 5 orbitals and the spherical harmonics which span a 5-dimensional space (that is, the spherical harmonics Y_l^m with $l = 2$) allows us to rewrite the relevant orbitals as linear combinations of the eigenstates of the operators L^2, L_z. This yields a new basis for each irrep considered above:

$$E_1 : Y_2^{-2} = |d_{-2}\rangle \, ; Y_2^2 = |d_2\rangle \qquad \text{1st orbital doublet,} \tag{2.18}$$

$$E_2 : Y_2^{-1} = |d_{-1}\rangle \, ; Y_2^1 = |d_1\rangle \qquad \text{2nd orbital doublet,} \tag{2.19}$$

$$A : Y_2^0 = |d_0\rangle \qquad \text{orbital singlet.} \tag{2.20}$$

When the spin multiplicity is considered, each orbital doublet yields 4 possible states, whereas the orbital singlet yields 2 possible states. Spin-orbit coupling (represented by the operator $H_{SO} = -\lambda \mathbf{L} \cdot \mathbf{S}$) is responsible for splitting these states into 5 different Kramers doublets:

$$\text{KD1} : \left|d_{+2}, +\tfrac{1}{2}\right\rangle ; \left|d_{-2}, -\tfrac{1}{2}\right\rangle , \tag{2.21}$$

$$\text{KD2} : \left|d_{+2}, -\tfrac{1}{2}\right\rangle ; \left|d_{-2}, +\tfrac{1}{2}\right\rangle , \tag{2.22}$$

$$\text{KD3} : \left|d_{+1}, +\tfrac{1}{2}\right\rangle ; \left|d_{-1}, -\tfrac{1}{2}\right\rangle , \tag{2.23}$$

$$\text{KD4} : \left|d_{+1}, -\tfrac{1}{2}\right\rangle ; \left|d_{-1}, +\tfrac{1}{2}\right\rangle , \tag{2.24}$$

$$\text{KD5} : \left|d_{0}, +\tfrac{1}{2}\right\rangle ; \left|d_{0}, -\tfrac{1}{2}\right\rangle , \tag{2.25}$$

where the basis vectors are given in terms of the quantum numbers m_l and m_s which denote the projection of the orbital and spin angular momentum along the quantization axis, respectively (Fig. 2.A15). Here, the spin-orbit coupling is considered up to first order in the energy correction, whereas the wave function is corrected up to zeroth order.

A magnetic field lifts the degeneracy between the two components of each KD. This splitting is usually described phenomenologically by an effective Zeeman Hamiltonian in a system with pseudospin $\tilde{\mathbf{S}} = \frac{1}{2}$.

$$H_{eff} = -\mu_B \mathbf{B} \cdot \mathbf{g} \cdot \tilde{\mathbf{S}}_{1/2}, \tag{2.26}$$

where μ_B is the Bohr magneton, $\mathbf{B}$ the magnetic field vector, $\tilde{\mathbf{S}}_{1/2}$ the pseudo spin $\frac{1}{2}$ operator and $\mathbf{g}$ the g-tensor. In the presence of axial symmetry, $\mathbf{g}$ can be diagonalized such that equation (2.26) can be rewritten in terms of the symmetry axis of the crystal

$$H_{eff} = -\mu_B \Big(g_{\parallel} B_z \tilde{S}_{1/2,z} + (g_{\perp} B_x \tilde{S}_{1/2,x} + g_{\perp} B_y \tilde{S}_{1/2,y}) \Big). \tag{2.27}$$

In terms of the eigenstates belonging to each KD, the splitting is described by the Zeeman Hamiltonian given by

$$H_{Zee} = -\mathbf{B}\cdot\boldsymbol{\mu} = -\mu_B\mathbf{B}\cdot(g_0\mathbf{S} + k\mathbf{L}), \tag{2.28}$$

where $\boldsymbol{\mu}$ is the magnetic moment operator, g_0 the g-factor for a free electron, $\mathbf{S}$ the total spin operator, k the orbital reduction factor, and $\mathbf{L}$ the orbital angular momentum operator [50,55]. The orbital reduction factor k, is a factor between 0 and 1 which corrects for partial covalent bonding between the electron and the ligands [50] (note that the value of k differs for each of the 5 KDs in equations (2.21-2.25)). Comparison of equations (2.27) and (2.28) shows that

$$g_{\parallel} = 2\langle g_e S_z + kL_z\rangle = \frac{2\langle\mu_z\rangle}{\mu_B}, \tag{2.29}$$

$$g_{\perp} = 2\langle g_e(S_x + S_y) + k(L_x + L_y)\rangle = \frac{2\langle\mu_x + \mu_y\rangle}{\mu_B}. \tag{2.30}$$

As long as the magnitude of this Zeeman splitting is small compared to the spin-orbit interaction we can consider, to first order, the effect of the magnetic field in the sets formed by each KD independently. That is, we consider that the magnetic field does not mix states pertaining to two different KDs.

In order to calculate the values of $g_{\parallel}$ and $g_{\perp}$ for each KD defined by trigonal symmetry and spin-orbit coupling, we rewrite equation (2.28) as

$$H_{Zee} = -(B_z\mu_z + B_x\mu_x + B_y\mu_y) = -(B_z\mu_z + \tfrac{1}{2}(B_+\mu_- + B_-\mu_+)), \tag{2.31}$$

where the $+$ and $-$ subindices denote the raising and lowering magnetic moment operators and the linear combinations $B_x \pm iB_y$, respectively. When we consider the basis given in equations (2.21-2.24), the matrix elements of both μ_+ and μ_- are zero between two eigenvectors pertaining to one KD. This arises from the fact that the operator μ_+ couples states with (m_l, m_s) to states with $(m_l + 1, m_s)$ or $(m_l, m_s + 1)$. Since, within a KD, there is a change in both m_l and m_s when going from one eigenvector to the other, the operators μ_+ and μ_- cannot couple these states to each other. Explicitly, for KD1 for example, we obtain

$$\left\langle d_{+2}, -\tfrac{1}{2}\middle|\mu_{\pm}\middle|d_{+2}, -\tfrac{1}{2}\right\rangle = 0, \tag{2.32}$$

$$\left\langle d_{+2}, -\tfrac{1}{2}\middle|\mu_{\pm}\middle|d_{-2}, +\tfrac{1}{2}\right\rangle = 0, \tag{2.33}$$

$$\left\langle d_{-2}, +\tfrac{1}{2}\middle|\mu_{\pm}\middle|d_{-2}, +\tfrac{1}{2}\right\rangle = 0, \tag{2.34}$$

and in a similar way for KDs 2 through 4. Thus, up to first order, a magnetic field applied perpendicular to the crystal c-axis is not capable of lifting the degeneracies of the 4 KDs given in equations (2.21)-(2.24). Comparing these results to equation (2.30) we conclude that, for the 8 sublevels of the KDs 1 through 4, $g_\perp = 0$. This arises from the effect of both the crystal field of C_{3v} symmetry and SOC in decoupling and isolating KDs with the properties mentioned above. This is not the case for KD5, given in equation (2.25). In this case,

$$\left\langle d_0, -\tfrac{1}{2}\middle|\mu_\pm\middle|d_0, +\tfrac{1}{2}\right\rangle \neq 0 \tag{2.35}$$

and the degeneracy of this KD is broken in the presence of a magnetic field perpendicular to the c-axis of the crystal.

We can consider in addition the effect of spin-orbit coupling in mixing the eigenstates presented in equations (2.21-2.25). Spin-orbit coupling is responsible for mixing between the eigenstates of KD2 and KD3 (equations (2.22) and (2.23)). Since both of these KDs show $g_\perp = 0$, this mixing does not modify the expected value of $g_\perp$ in neither KD. In contrast, the SOC induced mixing between KD4 and KD5 causes some deviation of $g_\perp$ from 0 in KD4, since $g_\perp \neq 0$ in KD5. The values of $g_\parallel$ and $g_\perp$ for one electron in each of the KDs described in this section are presented in table 2.A2.

From the 5 KDs in equations (2.21-2.25), one KD is the ground state and one KD is the excited state that we address in our experiments. As said before, our group-theoretical approach cannot identify the ordering in energy of these 5 KDs. However, by looking at the g-factor properties of the KDs in table 2.A2 we can check which ones show consistent behavior with that of the observed ground and excited state. For the observed ground state, we found $|g_\parallel| < 2$ and $g_\perp = 0$. Concerning possible values for the orbital reduction factor k, by definition $k < 1$, and we must have $k > 0.1$ since $|g_\parallel|$ deviates substantially from 2. This suggests that KD2 is the ground state. For the excited state, we also have $|g_\parallel| < 2$, but with $g_\perp \gtrapprox 0$. This suggests KD4 is the excited state we observed in our experiments. In addition, the optical transition observed is mainly polarized along the crystal c-axis of the defect. Careful analysis of the selection rules associated with the double trigonal group (which includes, besides the spatial symmetry, the spin of the electron) has been reported by Kunzer *et al.*[56]. Comparing their results to the considerations presented in the previous paragraphs confirms that the transition between KD2 and KD4 is predominantly polarized along the crystal c-axis, as observed. Finally, we note that we could not experimentally identify secondary ZPLs corresponding to transitions between other sets of KDs, even though they are allowed by symmetry. This could be explained by a series of factors. On the one hand, some of the KDs treated could

Table 2.A2: The g-factors of the Kramers doublets originated due to spin-orbit coupling within each subspace of the electronic eigenstates in a field of C_{3v} symmetry. Spin-orbit coupling is added as a perturbation, and included up to first order. The parameters λ and δ are as defined in the text and in Fig. 2.A15. Note that the g-factor values in this table can take on negative values, while in our experimental analysis we can only extract $|g_{\parallel}|$ and $|g_{\perp}|$.

C_{3v}	Spin-Orbit	$g_{\parallel}$	$g_{\perp}$
Doublet, $m_l = \pm 2$	KD1, eq. 2.21	$2(2k+1)$	0
	KD2, eq. 2.22	$2(2k-1)$	0
Doublet, $m_l = \pm 1$	KD3, eq. 2.23	$2(k+1)$	0
	KD4, eq. 2.24	$2(k-1)$	$0 + \propto \frac{\lambda}{\delta}$
Singlet, $m_l = 0$	KD5, eq. 2.25	2	$2 - \propto \frac{\lambda}{\delta}$

have energies above the conduction band edge in the crystal, which would impede the observation of optical transitions from and into these levels. On the other hand, the presence of these lines could be masked by the intense phonon sideband at the red side of the ZPL, or the associated photon energies fall outside our detection window.

Validity of our assumptions

The model considered here is capable of qualitatively informing us about the behavior of orbitals with d character in the presence of trigonal crystal field and spin orbit coupling. It is clear that the full description of the configuration of the defect is far more subtle than the simple model applied here. We intend to comment on this in the next paragraphs.

Symmetry of the crystal field. In our derivation, we assume that the trigonal crystal field is the prevailing term in the Hamiltonian describing the defect. This assumption is not rigorously correct, since the symmetry of defects in SiC is more accurately described by a ligand field of cubic symmetry – which determine most of its ground and excited state properties. This field is modified in the presence of axial symmetry, as is the case for defects in hexagonal lattice sites, which is generally included as a first-order perturbation term in the Hamiltonian. Nonetheless, it can be shown [50,57] that the large anisotropy in the Zeeman response described above, with the cancelation of $g_{\perp}$, is also observed in the case of a cubic field with trigonal distortion and spin-orbit coupling of similar magnitudes. The analysis, in this case, is more laborious due to the fact that mixing of the orbitals is

involved, and calculating the matrix elements of the operators $L_{\pm}$, $S_{\pm}$, L_z and S_z is less trivial. Furthermore, this analysis would not increase our level of understanding of the system at this point, since we were only capable of observing transitions between the sublevels of two KDs in this experiment. This approach would be more profitable if transitions between other sets of KDs were observed, allowing us to unravel several parameters associated with the system, such as the strength of the spin-orbit coupling and trigonal crystal field.

Charge state of the defect. Similarly, it can be shown that the considerations presented here can be expanded to configurations where the 4d orbitals are filled by multiple electrons (for instance, a defect in a configuration $4d^3$). In this case, a doubly degenerate orbital configuration (in symmetry terms, a configuration of the kind ^{m}E, where m is the spin multiplicity) in the presence of a crystal field of C_{3v} symmetry gives rise to at least one KD with $g_{\perp} = 0$ when SOC is taken into account. Nonetheless, only a negatively charged Mo in a Si substitutional site would give rise to a defect in the configuration $4d^3$. The absence of the ZPL in n-doped samples indicates that this is unlikely.

In addition, a similar group theoretical analysis can show that one hole in a bonding orbital of symmetry E would also give rise to $g_{\perp} = 0$. Thus, the features observed here could also correspond to a positively charged $Mo_{V_{Si}-V_C}$ defect (where one of the six Mo electrons that participate in bonding is lost to the crystal lattice). Due to the strong hybridization between the Mo and the divacancy orbitals in this case, the description of this case is more subtle and will not be performed here.

Summary We showed that an analysis of the effect of the defect symmetry on the Zeeman energy splittings of its ground and excited states, combined with the experimental observations, helps us unravel the configuration of the defect studied in this work. We show that, in C_{3v} symmetry, a combination of the crystal field and spin-orbit interaction is responsible for the strong magnetic anisotropy observed experimentally. Furthermore, the fact that the defect studied in this work is only observed optically in samples which are p-doped indicates that the charge of the defect is more likely positive than negative. In this way, we conclude that the most probable configuration of our defect is a Mo ion on a Si substitutional site of h symmetry, with a charge +1, which can be approximately described by a Mo atom in a $4d^1$ configuration. The absence of other lines associated with the defect prevents us from providing a more accurate description of the system. Nonetheless, we have developed a qualitative description based on symmetry,

which explains the Zeeman splittings observed. The considerations presented here allow us to predict and rationalize the presence of strong anisotropy in other transition-metal defects in SiC. We expect neutrally charged vanadium defects in hexagonal lattice sites to show a magnetic behavior similar to the one observed in the Mo defects investigated in this work.

CHAPTER 3

Spin-relaxation times exceeding seconds for color centers with strong spin-orbit coupling in SiC

This chapter is based on: C. M. Gilardoni*, T. Bosma* *et al.* Spin-relaxation times exceeding seconds for color centers with strong spin-orbit coupling in SiC. *New Journal of Physics*, **22**, 103051 (2020)

Abstract

Spin-active color centers in solids show good performance for quantum technologies. Several transition-metal defects in SiC offer compatibility with telecom and semiconductor industries. However, whether their strong spin-orbit coupling degrades their spin lifetimes is not clear. We show that a combination of a crystal-field with axial symmetry and spin-orbit coupling leads to a suppression of spin-lattice and spin-spin interactions, resulting in remarkably slow spin relaxation. Our optical measurements on an ensemble of Mo impurities in SiC show a spin lifetime T_1 of 2.4 s at 2 K.

3.1 Introduction

Spin-active color centers in semiconductors have attracted significant interest for the implementation of quantum technologies, since several of these systems combine long-lived spin states with a bright optical interface[1–4]. Long distance spin entanglement has been achieved for a variety of defects as stationary nodes[5–8]. However, finding suitable emitters that combine long-lived spins, short excited-state lifetimes and optical transitions compatible with telecommunication fiber-optic infrastructure in an industrially established material has remained elusive. Silicon carbide, a wide band-gap semiconductor with mature fabrication technology, hosts a range of defect centers with optical transitions near or at the telecom range[9,10], including several defects containing transition metal (TM) impurities[11–17]. The electronic and spin properties of these defects derive largely from the character of the d-orbitals of the TM under the action of a crystal field determined by the lattice site[18–20]. Furthermore, the presence of a heavy atom in the defect implies that spin-orbit coupling (SOC) plays a significant role in the electronic structure of these color centers. Generally, as widely demonstrated by the solid state spin-qubit community, combining favorable spin properties and strong SOC can be challenging[17,21–23]. However, the extent to which the spin lifetimes of TM defects in SiC are limited by the strong influence of SOC is not clear.

We report here on slow spin relaxation with T_1 exceeding seconds below 4 K for a molybdenum defect ensemble in 6H-SiC, indicating that the defect spin is surprisingly robust with respect to spin relaxation despite the presence of strong SOC. In order to understand this, we measure the spin-relaxation time of the Mo defect in SiC between 2 and 7 K and identify the main processes leading to spin relaxation in this temperature range. We analyze the manifestation strength of these processes, while considering the electronic structure of the defect, and find that a combination of axial rotational symmetry and SOC suppresses several spin-relaxation mechanisms in this system, leading to unexpectedly long T_1. The analysis leading to these conclusions is general, relying on the character of the d-orbitals of the TM and the particular symmetry of the defect. Thus, a similar approach could be relevant in the interpretation of experiments on other point defects in crystals with analogous symmetries, such as vanadium defects in SiC (with optical transitions compatible with telecom infrastructure), group IV defects in diamond and point-defects in transition metal dichalcogenides[14,16,18,24–26].

3.2 Methods

We focus on the Mo defect associated with an optical transition line at 1121.3 nm in 6H-SiC, which consists of a Mo impurity in a Si substitutional site of quasi-hexagonal symmetry (Fig. 3.1(a), h site)[13,15]. The defect is positively ionized, such that after binding to four neighboring carbons, the TM is left with one active unpaired electron in its 4-d shell. In this lattice site – and only considering the rotational symmetry of the defect – both ground and excited states are two-fold orbitally degenerate, such that the orbital angular momentum is not quenched[20]. In the presence of SOC, the orbital degeneracy is broken, giving rise to two Kramer's doublets (KD) in the ground and two KDs in the excited state (Fig. 3.1(b))[13,15], resembling what is observed for the group IV defects in diamond[25].

Each KD is a doublet composed of a time-reversal pair: the doublet splits as an effective spin-1/2 system in the presence of a magnetic field, but its degeneracy is otherwise protected by time-reversal symmetry (see Appendix section 3.A4). The energy difference between the two spin-orbit split KDs in the ground state, Δ_{orb} in Fig. 3.1(b), is expected to be approximately 1 meV[15], in accordance with the appearance of a second zero-phonon line (ZPL) in resonant photoluminescence excitation (PLE) experiments at approximately 8 K (Fig. 3.1(c)). Finally, the presence of sharp phonon replicas of the ZPL in the photoluminescence spectrum indicates that the defect center couples strongly to localized vibrational modes (Fig. 3.1(b,d)).

We measure the spin-relaxation time of this defect by means of a pump-probe experiment as shown in Fig. 3.2. Experiments are performed on an esemble of defects in a 6H-SiC sample previously investigated in Ref.[13]. The sample showed p-doped character, and the defect concentration was estimated to be between 10^{14} and 10^{16} cm^{-3}. We create pulses out of a CW laser beam by using a combination of an electro-optical phase modulator (EOM) and a Fabry-Pérot (FP) cavity. The EOM generates sidebands from our CW laser at frequency steps determined by an RF input signal; by tuning the FP cavity to transmit this sideband only, we create pulses that turn on/off as the RF generator turns on/off. These pulses resonantly drive optical transitions between ground and excited states, and we measure the photon emission into the phonon sideband with a single-photon counter after filtering out the laser line. We apply a magnetic field non-collinear with the c-axis of the sample such that spin-flipping transitions between ground and optically excited states are allowed (Fig. 3.2(a-b))[13]. In order to counteract slow ionization of the defects (see Appendix section 3.A3 for further details), we apply a repump laser in between measurements[13,27–29].

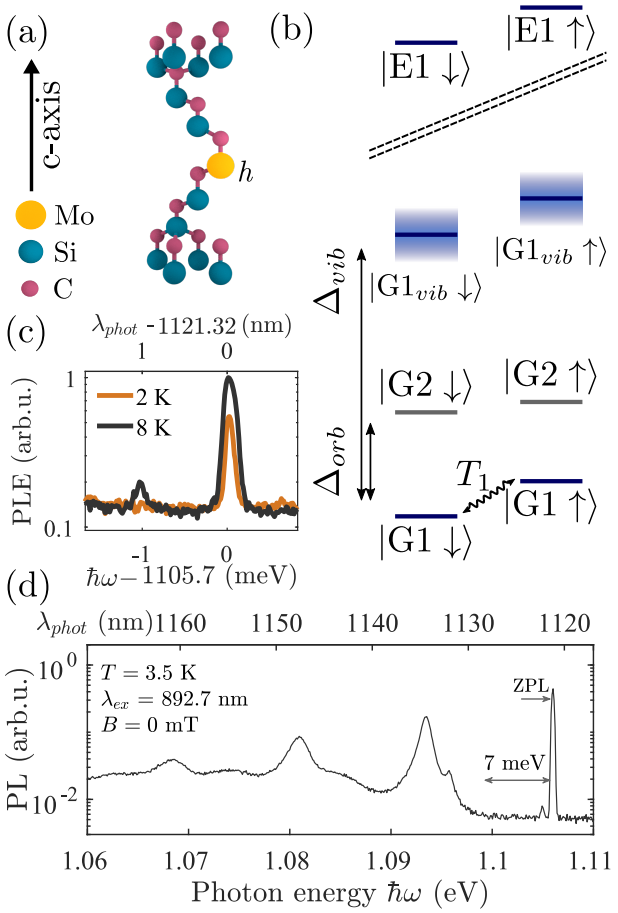

Figure 3.1: Defect and electronic structure. (color online) (a) The defect is composed of a Mo atom positively ionized substituting a Si at a quasi-hexagonal (h) lattice site. (b) Both ground ($|G1\rangle$) and optically excited ($|E1\rangle$) states are characterized by a spin doublet which is split by a magnetic field. Additionally, a second ground-state Kramer's doublet ($|G2\rangle$) is present approximately 1 meV above the ground state doublet. (c) When this second doublet is thermally occupied, a second zero-phonon line (ZPL) appears in the photoluminescence excitation (PLE) spectrum, where the light emitted in the phonon sideband is measured as a function of the laser photon energy $\hbar\omega$. (d) The electronic ground state can couple to localized vibrational modes, giving rise to vibronic states $|G1_{vib}\rangle$, as evidenced by the phonon replicas observed in the photoluminescence (PL) spectrum.

3.3 Results

In the pump-probe experiment (Fig. 3.2(c)), the initial response of the sample to pulse P1, h_1, provides a measure of the population in the bright

spin state $|G1\downarrow\rangle$ at thermal equilibrium (see the caption of Fig. 3.2 for an explanation of the terms dark and bright spin sublevels in this work). The sharp increase (decrease) of the PL signal as the pulse turns on (off) indicates that both the optical decay rate and the Rabi frequency are relatively fast (see Appendix section 3.A5 for further details). Optical excitation provided by P1 polarizes the spin ensemble in a dark spin sublevel ($|G1\uparrow\rangle$ in Fig. 3.2(b)) within the first few microseconds, as evidenced by the decrease and subsequent saturation of the PLE signal (the saturation level shows that the effective T_1 is lower when the laser is on, see Appendix section 3.A5). The leading-edge response of the ensemble to a second (probe) pulse P2, h_2, reflects the recovery of the population in the bright spin sublevel ($|G1\downarrow\rangle$ in Fig. 3.2(b)) during the time τ between the two optical pulses. Between 2 K and 7 K, we observe a monoexponential recovery of h_2 towards h_1 as a function of τ (Fig. 3.2(d)), which must correspond to the spin-relaxation time T_1 given the considerations presented below.

We repeat this experiment at zero magnetic field in order to confirm that the PL darkening observed within the first few microseconds of optical excitation corresponds to optical pumping of the ensemble into a dark spin sublevel. In this case, we observe no leading-edge peak in the PLE signal, indicating that no optical pumping occurs at this timescale if the spin sublevels are degenerate (see Appendix Fig. 3.A5). The absence of PL darkening at zero magnetic field implies that we cannot trap Mo centers in state $|G2\rangle$ for observable times. This is the case if the optical decay rate between states $|E1\rangle$ and $|G2\rangle$ is smaller than the relaxation rate between the two ground state KDs $|G1\rangle$ and $|G2\rangle$ in the temperature range investigated. (We expect the optical decay rate between $|E1\rangle$ and $|G2\rangle$ to be small, since we observe no lines corresponding to this transition in PL and PLE scans.) Thus, we conclude that after optical pumping in the presence of a magnetic field, no significant population is trapped in state $|G2\rangle$, and that relaxation dynamics via this level do not affect the signals used to derive T_1. Furthermore, we investigate the timescale associated with bleaching due to ionization[28,29], which is found to be several orders of magnitude slower than the one associated with spin dynamics (see Appendix section 3.A3).

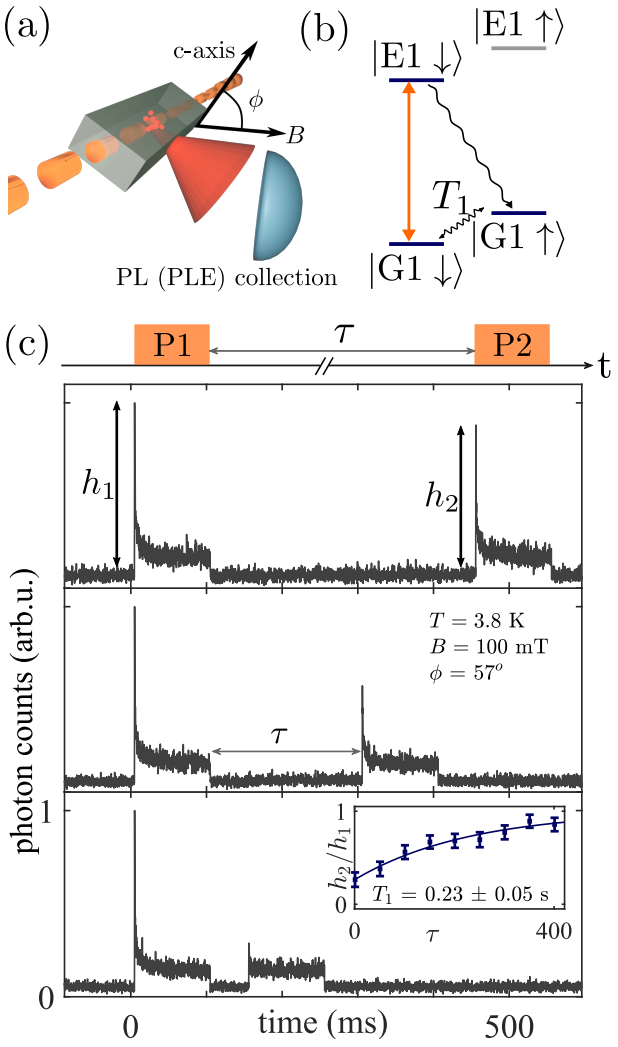

Figure 3.2: Time-resolved hole burning experiment. (color online) (a) In order to investigate T_1, we perform time-resolved pump-probe experiments where we resonantly excite the sample in the presence of a magnetic field and collect the phonon-sideband emission. (b) When the magnetic field is non-collinear with the symmetry axis of the defect, spin-flipping transitions between ground and optically excited states are allowed. (c) The first pulse P1 probes the population at thermal equilibrium in the ground-state spin sublevel $|G1\downarrow\rangle$ (which we call bright state in this work, since it can be optically excited), and polarizes the spin population into a spin sublevel that cannot be optically excited, $|G1\uparrow\rangle$ (which we here call dark state). After a variable delay τ, a second pulse P2 probes the recovery of the population in the bright state. (inset) The ratio of the leading-edge peaks in the PLE signal (h_2/h_1) recovers monoexponentially as a function of the delay between the two pulses.

The temperature dependence of the spin-relaxation time spans several orders of magnitude, going from 2.4 s at 2 K to 83 μs at 7 K (Fig. 3.3). Concerning phonon mediated spin relaxation, the mechanisms leading to spin relaxation are well established [20,30]. One (direct) and two-phonon (Raman, Orbach) processes are relevant when transitions between the levels involved are thermally accessible. Direct spin-flip processes are expected to lead to spin-relaxation rates ($\Gamma = T_1^{-1}$) that grow linearly with temperature ($\Gamma_{direct} \propto T$). In contrast, two-phonon processes mediated by an excited state give rise to spin-relaxation rates that grow superlinearly with temperature ($\Gamma_{Raman} \propto T^{5<n<11}$ and $\Gamma_{Orbach} \propto e^{-\Delta/k_B T}$, where Δ is the energy of the relevant excited state) [20,30–32]. Additionally, interaction with paramagnetic moments in the material is expected to lead to temperature-independent spin relaxation. We fit the data presented in Fig. 3.3 to a combination of these processes and identify the temperature regimes where they are relevant (see Appendix section 3.A7 for additional details concerning the fitting procedure).

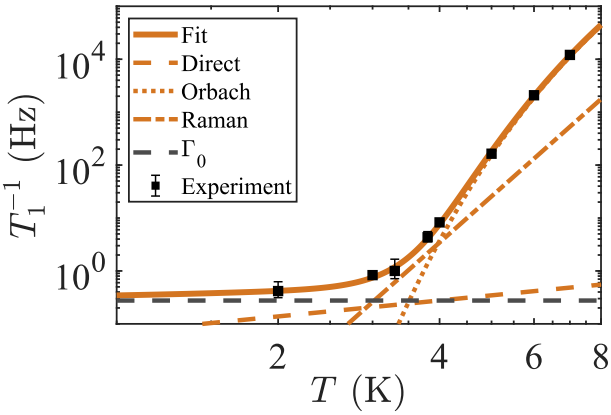

Figure 3.3: Temperature dependence of spin relaxation. (color online) The variation of $\Gamma = T_1^{-1}$ with temperature can be accurately described by a combination of direct (one-phonon), Raman and Orbach processes (two-phonon processes). The two-phonon processes happen due to coupling to an excited state approximately 6.5 meV above the ground state KD, compatible with coupling of the electronic state of the defect to localized vibrational modes. Error bars are extracted from the exponential fits of the data presented in the inset of Fig. 3.2(c) (for details, see Appendix section 3.A7), and are smaller than the data points when not visible.

The defect has a rich electronic structure, with orbital and vibrational degrees of freedom at energies that are thermally accessible between 2 and 7 K (Fig. 3.1(b)). Thus, we expect two-phonon processes involving

transitions into both orbital and vibrational excited states to contribute to the temperature dependence of Γ. Surprisingly, we find that not all available states contribute significantly to spin relaxation, leading to unexpectedly long spin lifetimes below 4 K.

Above 4 K, we identify an exponential growth of Γ as a function of temperature, indicating the prevalence of spin relaxation via Orbach processes in this temperature range. From the fit presented in Fig. 3.3, we extract $\Delta = 6.5 \pm 1$ meV for the energy of the excited state involved in these spin flips. This energy matches the difference observed in PL experiments between the ZPL and the onset of the phonon-sideband emission (Fig. 3.1(d)). The first phonon replica is observed 10 meV above the ZPL, but its broadened line indicates that the first available vibrational levels are lower in energy. Thus, we identify vibronic levels where the spin is coupled to localized vibrational modes as the relevant excited state for two-phonon mediated spin-relaxation processes that degrade T_1 above 4 K. As expected, these spin-relaxation mechanisms do not depend on the magnitude of the magnetic field (see Appendix Fig. 3.A6e).

We note that we cannot observe Orbach processes involving states $|G2\rangle$. Between 2 and 7 K, the contribution of these processes to the spin relaxation is expected to be close to saturation, giving a flat temperature dependence in this range. Thus, the long spin-relaxation times observed at 2 K provide an upper bound to the spin-relaxation rates due to two-phonon processes mediated by $|G2\rangle$, and are evidence that these processes are slow. This leads us to conclude that transitions between $|G1\rangle$ and $|G2\rangle$ are strongly spin-conserving. Based on this, we can estimate the timescale of phonon-induced transitions between the two doublets $|G1\rangle$ and $|G2\rangle$ to be on the order of milliseconds [33]. This process is orders of magnitude slower than the same process in SnV in diamond, a group IV defect with similar mass to the Mo defect in SiC, [26,34]. We note that, for this class of defects in diamond, the active electrons participate in bonding to the neighboring carbon atoms [25], which may change the character of the phonons responsible for spin-lattice interactions. In fact, the gap observed between the ZPL and the PSB for the Mo defect is absent in the PL spectrum of group IV defects in diamond [35], indicating that the latter are more sensitive to low-energy phonons.

Spin-conserving phonon mediated transitions between the two orbital states are expected to contribute to decoherence [36], limiting the spin coherence time T_2 of the $|G1\rangle$ spin to millisecond timescales at 4 K. This is significantly larger than the experimentally observed ensemble T_2^* [13], likely due to an inhomogeneus distribution of Zeeman splittings [18].

Below 4 K, the slow spin-relaxation rates observed must result from three mechanisms: *i*) processes whose temperature dependence is saturated in this

range (as treated above); *ii*) direct one-phonon transitions between the two spin sublevels $|\mathrm{G1}\downarrow\rangle$ and $|\mathrm{G1}\uparrow\rangle$ and *iii*) temperature independent processes (such as spin-spin paramagnetic coupling). The long T_1 observed below 4 K is evidence that all three processes are relatively slow for this particular system. The first contribution has been discussed above. Below, we elaborate on how the electronic structure of this defect leads to a suppression of the latter two processes.

The two spin-sublevels pertaining to a KD are strictly time-reversal symmetric with respect to each other, such that they must be degenerate eigenstates of any external field that preserves time-reversal symmetry. Thus, to first order, phonons or electric fields cannot cause a direct spin-flip within pure KD pairs (but note that this does not concern transitions between levels belonging to different KDs, see Appendix section 3.A4). A magnetic field or the interaction with nearby nuclear spins leads to mixing between spin sublevels pertaining to different KDs, enabling direct spin-flips via interactions with single phonons. This mixing is inversely proportional to the energy separation between the various KDs, which is in turn largely determined by the spin-orbit splitting. Thus, large SOC protects the KD character of the ground state spin doublet, suppressing direct spin-flipping processes within the spin doublet.

Additionally, SOC leads to a highly anisotropic Zeeman splitting of the ground-state spin sublevels[13], which hinders its interaction with a bath of paramagnetic impurities in the SiC crystal. Firstly, the spins are insensitive to magnetic fields perpendicular to their quantization axis, such that small fluctuations in the local magnetic field are not likely to induce a spin flip. Secondly, the spin doublet has a Zeeman splitting governed by a g factor that is at maximum 1.6[13], suppressing resonant spin flip-flop interactions with neighboring paramagnetic impurities with $g \approx 2$.

The same arguments presented above to explain the long spin-relaxation times observed in this defect indicate that obtaining control of the defect spin via microwave fields is a challenge. Driving spin resonances between the two ground state spin sublevels requires mixing of the various KDs by a perturbation that breaks time-reversal symmetry, such as a strong magnetic field (see Appendix section 3.A3). This is necessary to control the ground state spin via microwaves, and is expected to contribute to spin-relaxation mechanisms.

3.4 Discussion and conclusion

As discussed above, in the particular case of a TM at a quasi-hexagonal site, such as the Mo center, a combination of rotational symmetry and strong SOC protects the effective spin from flipping: it gives rise to ground state effective spin which is an isolated KD, protected by time-reversal symmetry and magnetically isolated from other paramagnetic centers in the crystal due to its unique Zeeman structure. In this doublet, the crystal field locks the orbital angular momentum along the axis of rotational symmetry of the defect. Via the strong SOC, the electronic spin is stabilized, giving rise to robust effective spin states with long spin-relaxation times.

Considering these processes alone, stronger SOC is thus expected to lead to slower spin-relaxation rates in TM color centers with an odd number of electrons and rotational symmetry. Nonetheless, our work shows that the presence of localized vibrational modes is pivotal in generating spin-flips, their energy determining the temperature where the onset of two-phonon relaxation mechanisms happens. Since the energy and density of states of the localized vibrational modes depend non-trivially on the mass of the defect, whether or not defects containing heavier TMs (where SOC is more prevalent) will exhibit longer spin-relaxation times remains a question. In fact, the class of group IV defects in diamond show significantly faster spin relaxation, which depends non-trivially on the mass of the defect [26,34]. Thus, it would be relevant to investigate these processes in defects containing 5-d electrons in SiC. Tungsten defects, for example, have been observed with an optical transition at 1240 nm and an odd number of electrons, although their microscopic configuration is still unknown [37].

More generally, SOC should not be regarded as a detrimental feature when investigating solid-state defects for quantum communication applications. Transition metal defects in SiC offer interesting opportunities, such as charge-state switching [38,39], emission in the near-infrared [14] and long spin lifetimes [17]. The maturity of the SiC-semiconductor industry means that a wide range of defects has been identified [18]. Nonetheless, their characterization with respect to optical and spin properties is still vastly unexplored.

Data availability

The data sets generated and analyzed during the current study are available from the corresponding author upon reasonable request.

Acknowledgements

We thank A. Gali, A. Csóré and P. Wolff for discussions. Technical support

from H. de Vries, J. G. Holstein, T. J. Schouten, and H. Adema is highly appreciated. Financial support was provided by the Zernike Institute BIS program, the EU H2020 project QuanTELCO (862721), the Swedish Research Council grants VR 2016-04068 and VR 2016-05362, the Knut and Alice Wallenberg Foundation (KAW 2018.0071), and the Carl Tryggers Stiftelse för Vetenskaplig Forskning grant CTS 15:339.

Author Contributions

The project was initiated by C.H.v.d.W. and T.B. SiC materials were grown and prepared by A.E. and B.M. Experiments were performed by T.B., D.v.H. and C.G, except for the PL measurements which were done by I.G.I. Data analysis was performed by C.G., T.B., D.v.H., F.H. and C.H.W. C.G., T.B., and C.H.W. had the lead on writing the paper, and C.G. and T.B. are co-first author. All authors read and commented on the manuscript.

References

[1] Weber, J. *et al.* Quantum computing with defects. *Proc. Natl. Acad. Sci. U.S.A.* **107**, 8513 (2010).

[2] Awschalom, D. D., Bassett, L. C., Dzurak, A. S., Hu, E. L. & Petta, J. R. Quantum Spintronics: Engineering and Manipulating Atom-Like Spins in Semiconductors. *Science* **339**, 1174 (2013).

[3] Aharonovich, I., Englund, D. & Toth, M. Solid-state single-photon emitters. *Nat. Phot.* **10**, 631 (2016).

[4] Atatüre, M., Englund, D., Vamivakas, N., Lee, S.-Y. & Wrachtrup, J. Material platforms for spin-based photonic quantum technologies. *Nat. Rev. Mat.* **3**, 38–51 (2018).

[5] Gao, W., Imamoglu, A., Bernien, H. & Hanson, R. Coherent manipulation, measurement and entanglement of individual solid-state spins using optical fields. *Nat. Phot.* **9**, 363 (2015).

[6] Hensen, B. *et al.* Loophole-free Bell inequality violation using electron spins separated by 1.3 kilometres. *Nature* **526**, 682–686 (2015).

[7] Sipahigil, A. *et al.* Indistinguishable Photons from Separated Silicon-Vacancy Centers in Diamond. *Phys. Rev. Lett.* **113**, 113602 (2014).

[8] Klimov, P. V., Falk, A. L., Christle, D. J., Dobrovitski, V. V. & Awschalom, D. D. Quantum entanglement at ambient conditions in a macroscopic solid-state spin ensemble. *Sci. Adv.* **1**, e1501015 (2015).

[9] Magnusson, B. & Janzén, E. Optical Characterization of Deep Level Defects in SiC. *Mater. Sci. For.* **483**, 341 (2005).

[10] Zargaleh, S. *et al.* Evidence for near-infrared photoluminescence of nitrogen vacancy centers in 4H-SiC. *Phys. Rev. B* **94**, 060102 (2016).

[11] Gällström, A. *et al.* Optical properties and Zeeman spectroscopy of niobium in silicon carbide. *Phys. Rev. B* **92**, 075207 (2015).

[12] Koehl, W. F. *et al.* Resonant optical spectroscopy and coherent control of Cr^{4+} spin ensembles in SiC and GaN. *Phys. Rev. B* **95**, 035207 (2017).

[13] Bosma, T. *et al.* Identification and tunable optical coherent control of transition-metal spins in silicon carbide. *npj Quantum Inf.* **4** (2018). 48.

[14] Spindlberger, L. *et al.* Optical Properties of Vanadium in 4H Silicon Carbide for Quantum Technology. *Phys. Rev. App.* **12**, 014015 (2019).

[15] Csóré, A. & Gali, A. *Ab initio* determination of pseudospin for paramagnetic defects in SiC. *arXiv:1909.11587* (2019).

[16] Wolfowicz, G. *et al.* Vanadium spin qubits as telecom quantum emitters in silicon carbide. *Science Advances* **6** (2020).

[17] Diler, B. *et al.* Coherent control and high-fidelity readout of chromium ions in commercial silicon carbide. *npj Quantum Inf.* **6** (2020).

[18] Baur, J., Kunzer, M. & Schneider, J. Transition metals in SiC polytypes, as studied by magnetic resonance techniques. *Phys. Status Solidi A* **162**, 153–172 (1997).

[19] Kaufmann, B., Dörnen, A. & Ham, F. S. Crystal-field model of vanadium in 6H silicon carbide. *Phys. Rev. B* **55**, 13009 (1997).

[20] Abragam, A. & Bleaney, B. *Electron Paramagnetic Resonance Of Transition Ions*. International series of monographs on physics (Clarendon Press, Oxford, 1970).

[21] Tokura, Y., van der Wiel, W. G., Obata, T. & Tarucha, S. Coherent single electron spin control in a slanting Zeeman field. *Phys. Rev. Lett.* **96**, 047202 (2006).

[22] Beaudoin, F., Lachance-Quirion, D., Coish, W. A. & Pioro-Ladriere, M. Coupling a single electron spin to a microwave resonator: controlling transverse and longitudinal couplings. *Nanotechnology* **27**, 464003 (2016).

[23] Kobayashi, T. *et al.* Engineering long spin coherence times of spin-orbit qubits in silicon. *Nat. Mater.* (2020).

[24] Khan, M. A., Erementchouk, M., Hendrickson, J. & Leuenberger, M. N. Electronic and optical properties of vacancy defects in single-layer transition metal dichalcogenides. *Phys. Rev. B* **95**, 245435 (2017).

[25] Hepp, C. *et al.* Electronic Structure of the Silicon Vacancy Color Center in Diamond. *Phys. Rev. Lett.* **112**, 036405 (2014).

[26] Bradac, C., Gao, W., Forneris, J., Trusheim, M. E. & Aharonovich, I. Quantum nanophotonics with group IV defects in diamond. *Nat. Commun.* **10**, 5625 (2019).

[27] Beha, K., Batalov, A., Manson, N. B., Bratschitsch, R. & Leitenstorfer, A. Optimum photoluminescence excitation and recharging cycle of single nitrogen-vacancy centers in ultrapure diamond. *Phys. Rev. Lett.* **109**, 097404 (2012).

[28] Wolfowicz, G. *et al.* Optical charge state control of spin defects in 4H-SiC. *Nat. Commun.* **8**, 1876 (2017).

[29] Zwier, O. V., O'Shea, D., Onur, A. R. & van der Wal, C. H. All–optical coherent population trapping with defect spin ensembles in silicon carbide. *Sci. Rep.* **5**, 10931 (2015).

[30] Stevens, K. W. H. The theory of paramagnetic relaxation. *Rep. Prog. Phys.* **30**, 189 (1967).

[31] Kiel, A. & Mims, W. B. Paramagnetic Relaxation Measurements on Ce, Nd, and Yb in $CaWO_4$ by an Electron Spin-Echo Method. *Phys. Rev.* **161**, 386 (1967).

[32] Shrivastava, K. N. Theory of SpinLattice Relaxation. *Phys. Status Solidi B* **117**, 437 (1983).

[33] Harris, E. A. & Yngvesson, K. S. Spin-lattice relaxation in some iridium salts I. Relaxation of the isolated $(IrCl_6)^{2-}$ complex. *J. Phys. C* **1**, 990 (1968).

[34] Trusheim, M. E. *et al.* Transform-Limited Photons From a Coherent Tin-Vacancy Spin in Diamond. *Phys. Rev. Lett.* **124**, 023602 (2020).

[35] Thiering, G. & Gali, A. *AbăInitio* Magneto-Optical Spectrum of Group-IV Vacancy Color Centers in Diamond. *Phys. Rev. X* **8**, 021063 (2018).

[36] Jahnke, K. D. *et al.* Electron-Phonon Processes of the Silicon Vacancy centre in Diamond. *New J. Phys.* **17**, 043011 (2015).

[37] Gällström, A. *et al.* Optical identification and electronic configuration of tungsten in 4H and 6H-SiC. *Physica B: Condensed Matter* **407**, 1462–1466 (2012).

[38] Kunzer, M., Müller, H. D. & Kaufmann, U. Magnetic circular dichroism and site-selective optically detected magnetic resonance of the deep amphoteric vanadium impurity in 6H-SiC. *Phys. Rev. B* **48**, 10846 (1993).

[39] Dalibor, T. *et al.* Deep Defect Centers in Silicon Carbide Monitored with Deep Level Transient Spectroscopy. *Phys. Stat. Sol. A* **162**, 199 (1997).

[40] Dresselhaus, M. S., Dresselhaus, G. & Jorio, A. *Group Theory* (Springer-Verlag Berlin Heidelberg, 2008).

Appendix

3.A1 Experimental methods

Setup The laser power is 200 μW for the resonant pulsed beam at 1121.32 nm. It is polarized linearly along the 6H-SiC c-axis. The repump beam accounting for charge state switching has 2 mW power at 770 nm, it is pulsed with 80 MHz repetition rate.

Reinitialization time After the pump-delay-probe sequence thermal equilibrium should be recovered before the next sequence can be started. To this end a reinitialization time needs to be considered. We chose sufficiently low repetition rates to account for this reinitialization time. For the measurements at 6 K and 7 K we kept the repetition rate fixed throughout the measurement (at 35.7 Hz and 243.9 Hz resp.). In this way the reinitialization time was always well beyond 20 times the observed T_1 time. This renders any errors due to incomplete reinitialization negligible. In order to save time and to keep a consistent reinitialization time at all delay times, we scaled the repetition rate along with the delay for the measurements at 2 - 5 K. Here, the reinitialization time was always larger than 5 times the observed T_1 time. This limits the error in T_1 to 3%. Moreover, the error in this method is such that the measured T_1 value will always be lower than the true T_1 value, thus not affecting the integrity of our lower-bound measurement. Table 3.A1 shows the reinitialization times for all temperatures for which T_1 was measured.

Fitting routine We extract the T_1 lifetimes from the time-resolved PLE experiments as in Fig. 2(c) (main text) by comparing the leading edge response from the first pulse h_1 to that from the second pulse h_2. These are determined by taking the average of the first 20 bins (of varying size, dependent on the timescale at a certain temperature) of the responses to the pulses. The behavior of the fraction of h_2 and h_1 can be described as

$$\frac{h_2}{h_1} = \frac{h_0(1 - e^{-t/T_1}) + \delta}{h_0 + \delta}, \tag{3.1}$$

where δ is the baseline height, h_0 is the peak height at thermal equilibrium minus the baseline δ, and t is the delay between both pulses. This allows us to create a fit function

$$\frac{h_2}{h_1} = q(1 - e^{-t/T_1}) + 1 - q, \tag{3.2}$$

Table 3.A1: Reinitialization times used

Temperature	T_1	Reinitialization time
2.0 K	2.4 ± 0.8 s	30 s
3.0 K	1.2 ± 0.1 s	10 s
3.3 K	1.0 ± 0.4 s	10 s
3.8 K	0.23 ± 0.05 s	10 s
4.0 K	121 ± 8 ms	800 ms
5.0 K	6.1 ± 0.2 ms	70 ms
6.0 K	0.48 ± 0.03 ms	$26 - 23$ ms
7.0 K	83 ± 13 μs	$2.1 - 1.8$ ms

with only two free parameters: T_1 and q, which represents the fraction $\frac{h_0}{h_0+\delta}$.

For the uncertainty in the T_1 (and q) fit parameters we take the 95% confidence interval from fitting. However, for the 2 K and 3.3 K measurements this method yields unrepresentative large error bars due to the small size of these data sets. For these measurements we estimate the error by first only deriving a value for the q parameter (with error bar), directly from the PLE traces in Fig. 3.A12. The q parameter is determined by reading h_0 and δ from the PLE response traces of the initial pulses for those temperatures. Next, we use this range (set by error bar) of q values as input in an approach that only fits T_1, where we take for the uncertainty in T_1 again the 95% confidence interval. The way in which the error in determining h_0 and δ carries over into an error for T_1 is thus considered, but this is found to give a negligible contribution to the reported error.

Deadtime pile-up effect For the experiments in this work we used an avalanche photodiode single-photon counter (SPC) for detection. After every detection event the detector has to reset its state, for which a predefined deadtime is used (10 μs in our case). This creates a pile-up effect in our experiments when integrating many pulse sequences. We investigated how this causes an error in determining T_1.

The probability of having a count at time t can be described by the combined probability that a photon is present and detected at the counter P_{photon} multiplied by the probability of not having measured a photon before for the duration of the deadtime Δt. We get the equation

$$P_{\text{count}}(t) = P_{\text{photon}}(t) \left(1 - \int_{t-\Delta t}^{t} P_{\text{count}}(\tau) d\tau\right). \tag{3.3}$$

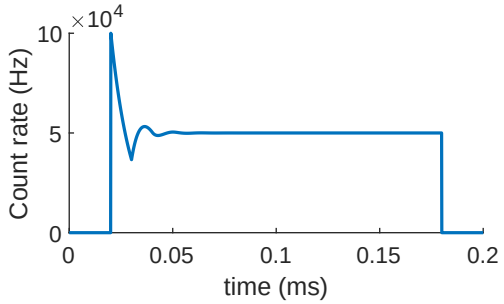

Figure 3.A4: Simulated count rate at the single-photon counter for signal above saturation values. Probability of counting a photon at time t, for a square PLE signal above saturation ($1/(10\mu s)$).

The outcome is plotted in Fig. 3.A4 for a square PLE response to a pulse where $P_{\text{photon}}(t) = 100$ kHz during the pulse, which saturates the SPC. Before the pulse, the detector is always ready to receive a photon, thus the initially measured count rate relates accurately to the number of photons present. For the duration of the deadtime (10 μs) the detector will be recovering and thus the count rate drops. This is periodic, but it clearly damps out to a steady-state count rate due to a spread in the actual detection times. This behavior is consistent with what we observe experimentally when illuminating the SPC with constant, intense light. This effect becomes less relevant, however, when illumination conditions are far from the saturation of the avalanche photodiode, and we used these findings to minimize the effect of the saturation of the SPC while maximizing the signal to noise ratio obtained.

Generally, this pile-up effect will give a positive error ϵ_1 (ϵ_2) for the measured value of h_1 (h_2). At small t the magnitude of the error ϵ_2 is low and increases to ϵ_1 as $t \gg T_1$. If we rewrite Eq. 3.2 to represent the measured values it becomes

$$\frac{h_2}{h_1} = q'(1 - e^{-t/T_1}) + 1 - q' + \frac{\epsilon_1 - \epsilon_2}{h_0 + \delta - \epsilon_1}, \tag{3.4}$$

where q' is represents the corrected fraction $\frac{h_0}{h_0+\delta-\epsilon_1}$. The final term in this equation makes the measured $\frac{h_2}{h_1}$ approach its asymptote faster than in reality. Thus, fitting $\frac{h_2}{h_1}$ to Eq. 3.2 will always yield shorter T_1 values compared to the true spin-flip times. Simulating the pile-up effect for our measurements yields errors in T_1 varying from 2% to 7%. We choose to not correct for this and report the lower-bound values for the T_1 spin-flip times. Background PLE and dark counts have been neglected in this analysis as we

found them to be of little influence so long as they remain below 10% of the peak count rate.

Total error of h_2/h_1 data points The error in the estimation of the ratio h_2/h_1 in the insets of Fig. 2c in the main text and Fig. 3.A12 is obtained from a combination of several contributions:

- Effects from saturation of SPC, treated in Sec. I*d*, and which contribute errors of approximately $2-7\%$ when the intensity of the signal is large compared to the saturation threshold of the SPC. This is only relevant for the data set at 7 K;
- At low temperatures, when the full measurement sequence time is above seconds, a drift in the resonance frequency of the Fabry-Pérot cavity during the measurement causes the intensity of the second pulse to be different than the intensity of the first pulse. This difference can be estimated from the difference in the steady state emission (the height of the trailing edge of the PLE). For the data set presented in the main text, that is, at 3.8 K, it contributes a maximum error of 7% to the value of h_2/h_1;
- When analyzing the data, we choose a time interval for which photon counts contribute to h_1, h_2. Varying this time interval changes the values of h_1, h_2 slightly, introducing errors to the ratio h_2/h_1. This error is also limited to 3%.

3.A2 Zero-field measurement

To confirm that the T_1 lifetimes measured are actually from the spin from the $|G1\rangle$ and not influenced by some other process, we performed zero-field experiments. Both ground-state spins are then degenerate and no spin pumping is expected. The results are shown in Fig. 3.A5. The leading-edge peak in PLE as seen in Fig. 2(c) in the main text vanishes in Fig. 3.A5(a). We note that thermal effects from laser driving at high intensities become more prominent at zero magnetic field, since darkening of the PLE no longer occurs. Additionally, we checked again the optical polarization dependence for these conditions at $B = 0$ mT, but this confirmed that the driving was still only sensitive to the component parallel to the c-axis.

In Fig. 3.A6 we show the evolution of the PLE response with magnetic field strength. Figure 3.A6(e) summarizes this experiment, depicting the steady-state baseline of the PLE response together with the leading-edge peak heights (baseline subtracted) upon ramping the field. Up to 4 mT the baseline decreases, indicating that spin-pumping occurs to an increasing degree. Beyond 4 mT it stabilizes. At this field the spin-splitting (49 MHz at 4 mT) is well beyond the homogeneous linewidth (15 MHz[13]) of the spin-states, and a single laser can no longer drive transitions from both spin states.

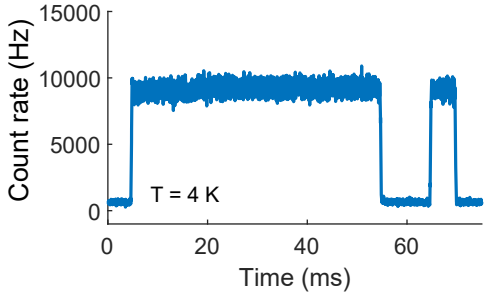

Figure 3.A5: Zero field measurement. Time-resolved PLE measurement at $B = 0$ T, $T = 4$ K and 200 μW excitation power. For this particular experiment, the excitation pulses were right-circularly polarized, but we found no unexpected dependence on polarization: the PLE response was always proportional to the component of linear driving along the c-axis.

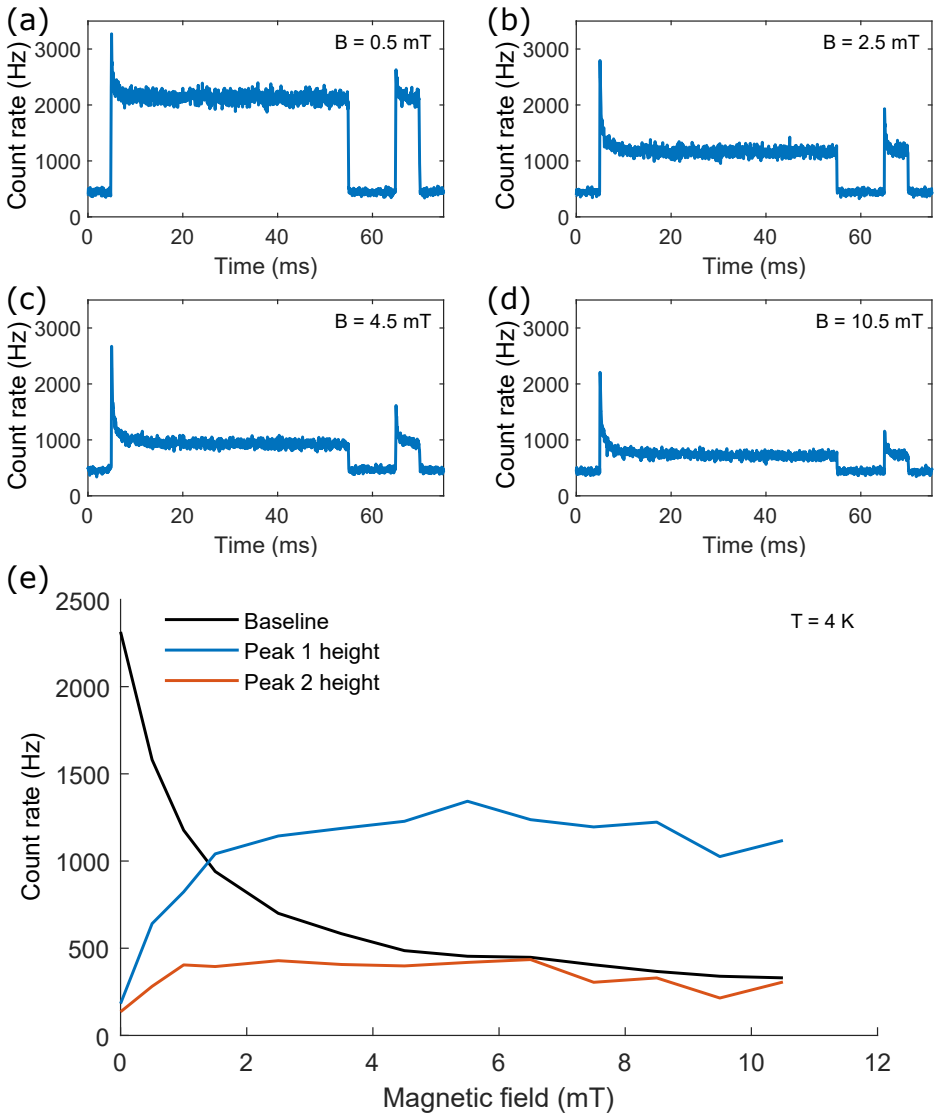

Figure 3.A6: Magnetic field dependence (a-d) Time resolved measurements at various magnetic fields. (e) Baseline and leading-edge peak heights (baseline subtracted) versus magnetic field. A repump laser counteracting any bleaching was always present in these experiments. All measurements at $T = 4$ K.

3.A3 Charge-state switching

When resonantly addressing optical transitions in the Mo defect in SiC, the PLE response drops over time. This is ascribed this to charge-state switching of the defect. We investigate the timescales of this bleaching in order to rule out its influence on the measurements of the T_1 spin-flip times.

The experimental approach is depicted in Fig. 3.A7(a). First, a repump beam (770 nm, pulsed) counteracts any prior bleaching[13], resetting the charge state for 60 seconds. Next, a probe beam resonant with the ZPL illuminates the sample, slowly bleaching the Mo defects. We can track the bleaching timescale by measuring the PLE response as function of time. After another 1000 seconds the repump beam is incident on the sample together with the probe beam, which allows us to track the recovery timescale. Finally, the repump is switched off for 60 seconds to check the initial decay of the PLE response. This sequence is repeated four times. We use a 2 mW repump beam and a 200 μW probe focused to approximately 100 μm diameter in the sample. The magnetic field strength is 100 mT at an angle of 57° with the c-axis.

The results are shown in Fig. 3.A8. The bleaching between 60 and 1060 seconds occurs according to two timescales, both are fit with an exponential decay for the orange and blue curve. The yellow curve is an exponential fit to the recovery by the repump laser. All three timescales are plotted versus temperature in Fig. 3.A7(b). For the T_1 experiments, where the repump beam was only on in between measurement runs, the two bleaching scales are most relevant. Both occur at rates that are at least one order of magnitude slower than the observed spin-flip times. Any bleaching occurring at faster timescales should have been visible in the zero-field measurements from section 3.A2. Thus, the effect of bleaching on measuring T_1 can be deemed negligible.

Note the fast decay of PLE for 4 K (Fig. 3.A8(a)) after the repump laser is blocked at 1300 seconds. We ascribe this to fast spin flips induced by the repump laser. When performing the experiments to measure T_1 with an omnipresent repump laser, we observe that T_1 is reduced by an order of magnitude (for similar laser powers). This fast decay is not visible in Fig. 3.A8(b-f) since the spin-flip times are already quite short at higher temperatures.

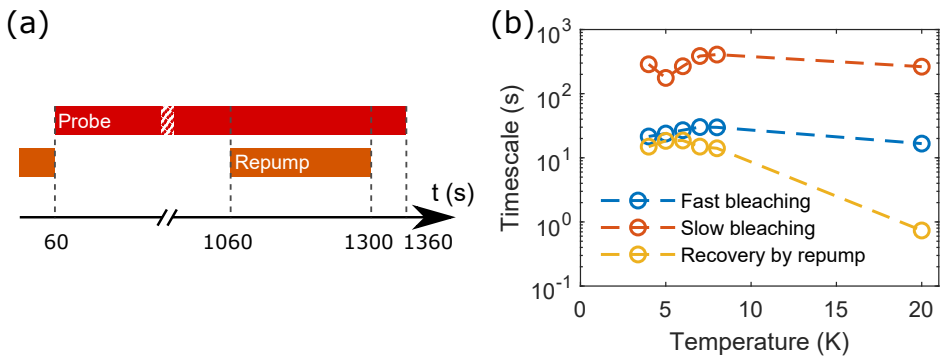

Figure 3.A7: Bleaching experiment (a) Sequence of lasers used to measure the bleaching/repump timescales. (b) The acquired timescales versus temperature.

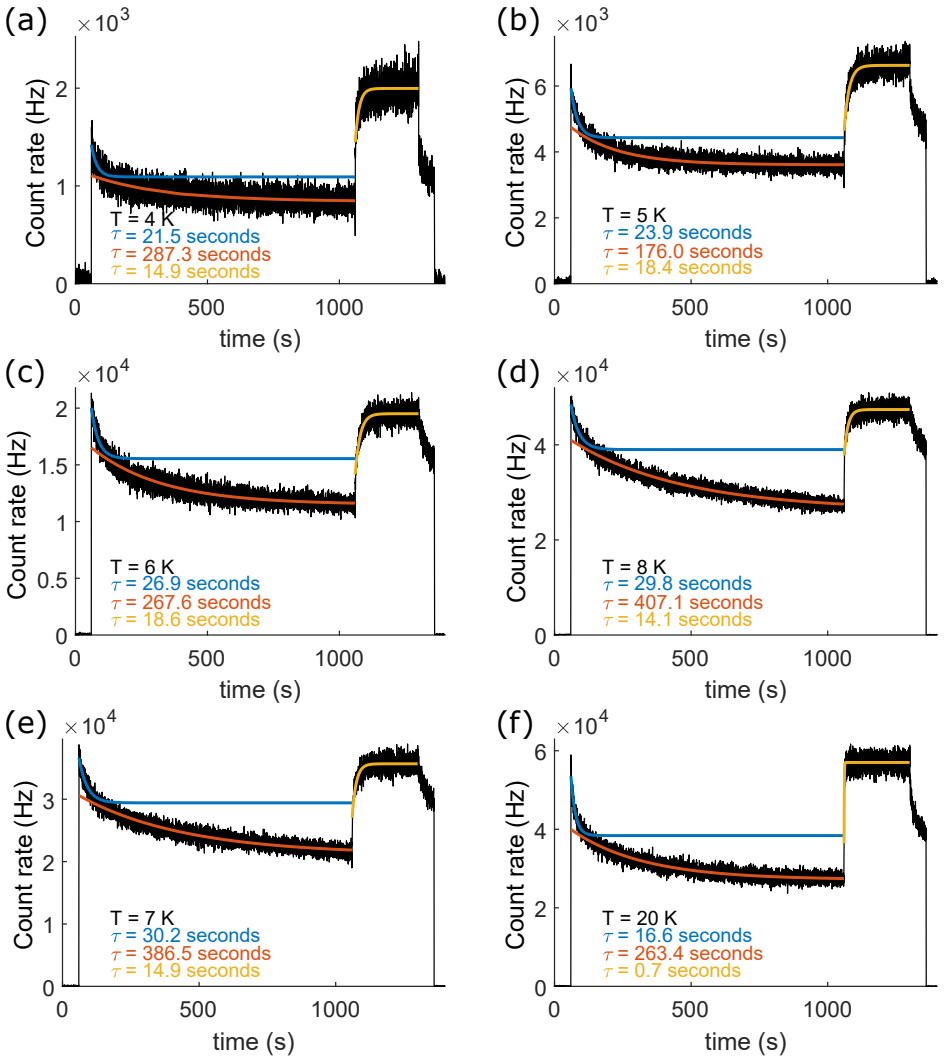

Figure 3.A8: Detailed bleaching results (a-f) Dynamics of the resonant photoluminescence signal (PLE) over long time periods, at various temperatures. A static background is subtracted as well as a fluorescence background induced by the repump when it is on (measured during the first 60 seconds). When the repump is off, but the system is being renonantly driven, the PLE signal decays exponentially with two characteristics time constants (blue and red fits). As the repump is turned on, the PLE signal recovers quickly, with a single time constant (yellow fit).

3.A4 Electronic structure - group theoretical approach

The Mo defect is characterized by a single active spin in the 4d shell of a molybdenum impurity at a Si substitutional lattice site[13]. In this configuration, the Hamiltonian of the defect has a three-fold rotational symmetry and three vertical mirror planes, such that the eigenfunctions of the electronic orbital state transform according to the symmetry group C_{3v}. Despite the extensive literature available on the effect of crystal field and spin-orbit coupling on the electronic states of these defects[19,38], we are unaware of a comprehensive report on the effect of symmetry on the coupling terms between the various specific spin sublevels and external fields based on the double group representations of the defect symmetry, and we present this analysis here. We apply a group-theoretical approach to obtain the symmetry of the eigenfunctions associated with a defect center in a crystal field of C_{3v} symmetry in the presence of spin-orbit coupling. Furthermore, we obtain and explain the selection rules governing the interaction of the electronic spin with magnetic and electric fields.

The group theoretical rules governing the selection rules presented in the end of this work do not rely on a particular basis set for the description of the electronic wavefunction. By this, we mean that even if we consider hybridization of the wavefunction of the bare transition metal atom/ion with the nearest carbon atoms due to covalent bonding, the symmetry of the crystal field Hamiltonian is preserved such that the new, modified wavefunctions will still obey the selection rules arising from a group-theoretical analysis. Nonetheless, it is instructive to start from an analysis of the effect of the Hamiltonian on the 10 spin-orbital states arising from a single electron sitting in one of the d-orbitals of the transition metal.

The transition metal at a silicon substitutional site shows tetrahedral coordination due to bonding to the 4 nearest carbons. In this configuration, the 5 d orbitals split into an orbital doublet and an orbital triplet (which transform as the irreps E and T_2 of the symmetry group T_d), where the triplet lies highest in energy. Due to the hexagonal character of the lattice, the tetrahedral symmetry of these sites is lowered to C_{3v}, with the rotational axis aligned parallel to the growth axis of the crystal. Upon this symmetry reduction, the triplet further splits giving rise to an orbital doublet and a singlet, which transform respectively as E and A_2. The effect of this symmetry lowering operation is expected to be largest in the lattice sites of quasi-hexagonal symmetry (h), and to only modestly affect the lattice sites of quasi-cubic symmetry (k) (Fig. 3.A9(a)).

A wavefunction transforming as a *non-degenerate* irrep of a given point-group cannot have an effective orbital angular momentum (in other words,

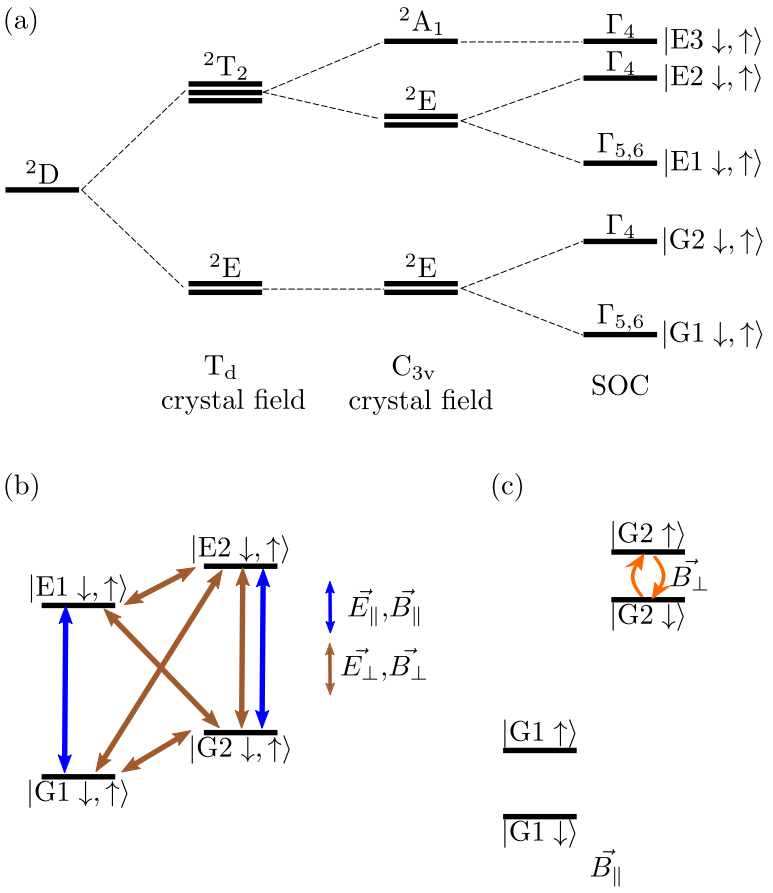

Figure 3.A9: Electronic Structure and selection rules based on group-theoretical analysis (a) The 10 spin-orbital states corresponding to the ^{2}D configuration of the free ion are split into 5 Kramer's doublets under the action of the crystal field and SOC, of which three transform as irrep Γ_4 and two transform as irrep $\Gamma_{5,6}$ of the double group $\bar{C}_{3v}$ (see main text). (b) Coupling between 2 KD transforming as $\Gamma_{5,6}$ is allowed under the action of an electric or magnetic field parallel to the symmetry axis; coupling between 2 KD transforming as Γ_4 is allowed under the action of an electric or magnetic field pointing in any direction; coupling between a KD transforming as $\Gamma_{5,6}$ and a KD transforming as Γ_4 is allowed under the action of an electric or magnetic field perpendicular to the symmetry axis. (c) A KD transforming as $\Gamma_{5,6}$ does not interact with a magnetic field perpendicular to the symmetry axis, whereas this is not the case for a KD transforming as Γ_4.

the orbital angular momentum is quenched)[20]. However, this requirement is lifted in the presence of degeneracies, such that the eigenfunctions of the Hamiltonian transforming as E are allowed to have a non-zero orbital angular momentum. Thus, in order to fully describe our system, we must consider

Table 3.A2: Character table of the double group $\bar{\mathrm{C}}_{3\mathrm{v}}$. The upper bar represents an operation followed by a 2π rotation that brings a spin $\uparrow$ into $\downarrow$.

	E	$\bar{\mathrm{E}}$	$2\mathrm{C}_3$	$2\bar{\mathrm{C}}_3$	$3\sigma_v$	$3\bar{\sigma}_v$		
A_1	1	1	1	1	1	1	z	z^2, x^2+y^2
A_2	1	1	1	1	-1	-1	R_z	
E	2	2	-1	-1	0	0	(x,y), (R_x,R_y)	$(x^2-y^2, 2xy)$, (xz,yz)
Γ_4	2	-2	1	-1	0	0		
$\Gamma_{5,6}$	1	-1	-1	1	i	$-i$		
	1	-1	-1	1	$-i$	i		

the effect of spin-orbit coupling. In a group-theoretical approach, this is done by extending the group of interest to include 2π rotations which bring a spin $\uparrow$ into a spin $\downarrow$[40]. That is, this is done by considering the eigenfunctions as basis states of the irreps of the double group associated with the $\mathrm{C}_{3\mathrm{v}}$ group, here denoted by $\bar{\mathrm{C}}_{3\mathrm{v}}$.

In the double group including the effect of spin-orbit coupling, three irreps describing how odd spin wavefunctions transform are added to the group. These irreps are Γ_4, which is doubly degenerate, and $\Gamma_{5,6}$, two irreps that are connected by time-reversal symmetry and must thus be degenerate in the presence of time-reversal symmetry. The orbital singlet transforming as A_2 gives rise to a Kramer's doublet (KD) transforming as Γ_4, whereas an orbital doublet transforming as E splits into two KDs, of which one transforms as irrep Γ_4, and the other transforms as irreps $\Gamma_{5,6}$. Thus, the symmetries mentioned above split the 10 states arising from an electronic configuration ^{2}D into 5 Kramer's doublets, of which 2 transform as $\Gamma_{5,6}$, and 3 transform as Γ_4 (Fig. 3.A9(a)). The character table of the double group $\bar{\mathrm{C}}_{3\mathrm{v}}$ is given in Tab. 3.A2. Additionally, we explicitly show what are the transformation properties of the vectors x, y, z and the axial vectors R_x, R_y, R_z, as well as how the cubic harmonics z^2, x^2-y^2, xy, xz, yz transform under the operations of the group.

We can investigate the role of small magnetic and electric fields in driving transitions between different KD (coupling between different KDs), and spin resonances (coupling between the two eigenstates pertaining to a single KD) in the framework of group-theory, given that these fields are small enough that the symmetries of the Hamiltonian H_0 are preserved. The selection rules between two wavefunctions can be obtained in a straight-forward way. If $|\psi_i\rangle$ and $|\phi_{i'}\rangle$ are two eigenstates of the Hamiltonian H_0 transforming

Table 3.A3: Product tables of the double irreps of $\bar{C}_{3v}$ and corresponding selection rules.

	Γ_4	Γ_5	Γ_6
Γ_4^*	$A_1 + A_2 + E$ $\vec{E}_\parallel$, $\vec{B}_\parallel$, $\vec{E}_\perp$, $\vec{B}_\perp$	E $\vec{E}_\perp$, $\vec{B}_\perp$	E $\vec{E}_\perp$, $\vec{B}_\perp$
$\Gamma_5^* = \Gamma_6$	E $\vec{E}_\perp$, $\vec{B}_\perp$	A_1 $\vec{E}_\parallel$	A_2 $\vec{B}_\parallel$
$\Gamma_6^* = \Gamma_5$	E $\vec{E}_\perp$, $\vec{B}_\perp$	A_2 $\vec{B}_\parallel$	A_1 $\vec{E}_\parallel$

respectively as irreps Γ_i, $\Gamma_{i'}$, the selection rules with respect to a perturbative Hamiltonian H' are given by the product $\langle\psi_i| H' |\phi_{i'}\rangle$. In order for this matrix element to be non-zero, it must transform as a scalar, that is, as the totally symmetric irrep A_1 [40]. Thus, the product of the representations $\Gamma_i^* \otimes \Gamma_j \otimes \Gamma_{i'}$, where the perturbation H' transforms as Γ_j and * denotes complex conjugation, must contain the totally symmetric irrep A_1.

Table 3.A3 gives the decomposition of the various products of Γ_4, $\Gamma_{5,6}$, in terms of irreps of the C_{3v} group, and translates this into the selection rules governing the coupling between various spin states.

Optical transitions between various sets of KDs are allowed due to coupling to $\vec{E}_\parallel$, $\vec{E}_\perp$, which belong to irreps A_1 and E, respectively. We can extract polarization selection rules from table 3.A3. Electric field driven transitions between two KDs transforming as $\Gamma_{5,6}$ will be polarized along the symmetry axis of the defect; transitions between two KDs transforming as Γ_4 can be polarized along any direction; transitions between a KD transforming as $\Gamma_{5,6}$ and a KD transforming as Γ_4 are only allowed for light polarized perpendicular to the symmetry axis. These properties are summarized in Fig. 3.A9(b). This means that only electric or magnetic fields of E symmetry (that is, in the xy plane) are capable of coupling and mixing states $|G1\rangle$ (which transforms as $\Gamma_{5,6}$) and $|G2\rangle$ (which transforms as Γ_4).

Transitions and energy splittings within each of the KDs can also be understood based on the symmetry of the defect. The anisotropic Zeeman structure observed for the ground state spin doublet, which is insensitive to magnetic fields perpendicular to the crystal symmetry axis [13] can be understood purely based on the properties of the group. A magnetic field along the symmetry axis of the defect transforms as R_z, whereas a magnetic field perpendicular to this axis transforms as R_x, R_y. Within a doublet which transforms as $\Gamma_{5,6}$, no coupling is allowed with a magnetic field perpendicular

to the symmetry axis since $\Gamma^*_{5,6} \otimes \mathrm{E} \otimes \Gamma_{5,6} = \mathrm{E} \not\supset \mathrm{A}_1$. This is not the case for a doublet transforming as Γ_4, such that the spin sublevels that transform as Γ_4 are allowed to couple to magnetic fields in the plane, and will not have $g_\perp = 0$. Thus, we conclude that the ground state doublet belongs to the irrep $\Gamma_{5,6}$ (Fig. 3.A9(c)). As long as the quantization axis of the defect spin (states $|G1\rangle$, belonging to irrep $\Gamma_{5,6}$) points parallel to the symmetry axis of the defect, we cannot rotate the spin via microwave spin resonances, since these spins are insensitive to magnetic or electric fields perpendicular to this axis.

If two spin sublevels are strictly connected by time-reversal symmetry (that is, they are a pure KD), they cannot be connected by operators that preserve time-reversal symmetry. This was proven by Kramer and became what is known as Kramer's theorem [40]. Thus, within a pure KD, electric fields are not capable of driving transitions between the two spin-sublevels.

Finally, we note that effect of electric fields on the optical transition energy is more subtle. Strictly speaking, from Kramers Theorem alone, we can say that the two spin-sublevels pertaining to a KD must have the same energy when subject to an electric field, but the actual value of this energy can change depending on the electrostatic environment of the defect. Additionally, if the electronic wavefunctions were composed by the d-orbitals exclusively, we would observe no optical transition (due to the spatial parity of the d-orbitals and of the electric dipole moment operator). Thus, the fact that the defects are optically active means that the optically excited state shows some hybridization of the d-orbitals with the lattice wavefunctions, and is thus sensitive to a spatially extended electrostatic environment. These two factors combined lead us to conclude that the excited state wavefunction can show some spectral diffusion.

3.A5 Simulation of raw data

Due to the large number of available states for defect (vibrational levels, orbital state $|G2\rangle$ in Fig.1 of the main text, ionized states), it is not straight forward to obtain quantitative information from the shape of the raw data plots presented in the main text. Nonetheless, we can apply a rate equation model to reproduce the data and, upon carefully taken assumptions, obtain a bound for the values of the optical decay time and Rabi driving frequency in our experiments.

In order to minimize the set of free parameters and facilitate the analysis of the behavior of the system, we simulate this defect center as a three-level system (Fig. 3.A10(a)), where the ground (state 1) and excited (state 3) states can be coupled by an optical field with Raby frequency Ω_R. From the optically excited state, the system can decay either back into the ground state with a rate Γ_{31}, or into a shelving state 2 with a rate Γ_{32}. Additionally, population can be transferred between states 2 and 1 at a rate Γ_{21}, and between 1 and 2 at a rate $\Gamma_{12} = e^{-\Delta/kT}\Gamma_{21}$, where Δ is the energy difference between 2 and 1 and kT denotes the thermal energy of the system. We simulate the system with a simple set of rate equations for the populations of each state (P_1, P_2, P_3), without treating coherences explicitly. Finally, we consider that the photoluminescence observed is proportional to the population of the optically excited state, P_3.

We try to reproduce the typical shape of the raw PL data obtained experimentally (Fig. 3.A10(b)) in order to obtain a set of reasonable values for the Rabi driving frequency and optical decay rates in our system. We assume that states 1 and 2 correspond to the ground state spin sublevels, $|G1_\downarrow\rangle$ and $|G1_\uparrow\rangle$ respectively. In this way, we can write Γ_{32} in terms of Γ_{31} by assuming that the branching ratios correspond to the overlap of the spin states in ground and optically excited state[13]. This gives $\Gamma_{32} \sim 0.003\ \Gamma_{31}$. Previous experiments revealed an excited state lifetime of ~ 56 ns, resulting in $\Gamma_{31} \sim 20$ MHz. Similar TM defects have been recently reported with optical excited state lifetime of ~ 100 ns. Thus, we simulate the experiment for values of Γ_{31} of 2 and 20 MHz. For Γ_{21}, we use the values presented in the main text for the spin lifetime (Fig. 3).

We note that differences based on the exact value of Γ_{31} are barely noticeable. Thus, we cannot restrict our estimate for Γ_{31} further. Nonetheless, we can restrict the expected values of Ω_R by comparing the calculated traces presented in Fig. 3.A10(c,d) and the raw trace presented in Fig. 3.A10(b). We not that if Ω_R is very small, of the order of a kHz, PL darkening is almost absent, unlike what is seen in experiment, where PL darkening is significant.

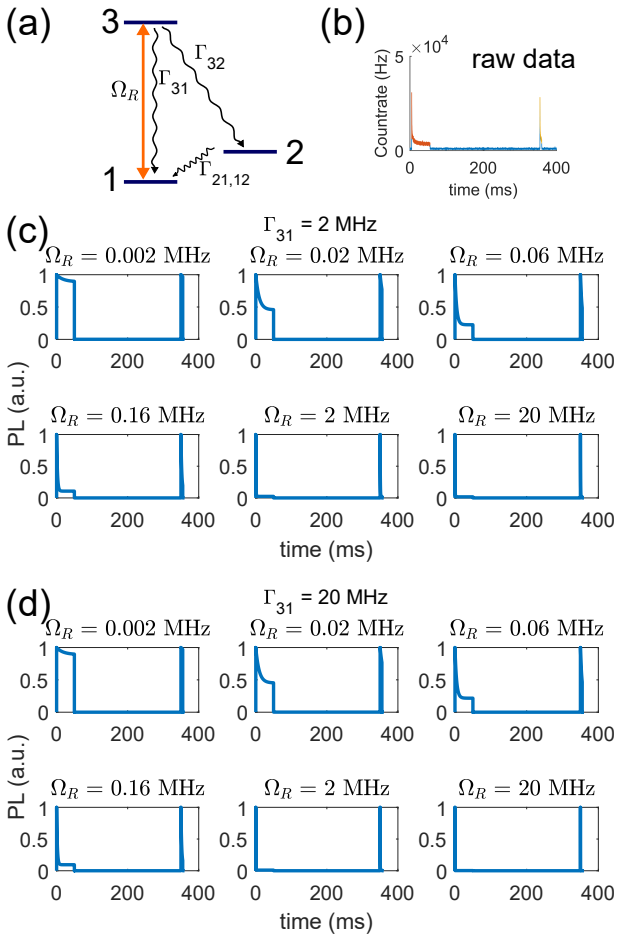

Figure 3.A10: Three-level model describing dynamics of defect in ms timescale (a) The three level model inclued a ground and optically excited states that are connected via optical driving with Rabi frequency Ω_R. The optically excited state can decay into the ground state or into a shelving state, with rates Γ_{31} and Γ_{32}. Population can decay back from the shelving state into the ground state with a rate Γ_{21}. The photoluminescence excitation signal obtained is assumed to be proportional to the population in the optically excited state. (b) Typical experimental data in the presence of a magnetic field consists of PLE signal with sharp on and offset as the laser turns on and off. After a leading edge peak, the PLE signal decays back to a constant non-zero value, indicative of PL darkening due to optical pumping into shelving states within the first few microseconds of illumination. (c,d) Simulating the dynamics of the population in the excited state upon illumination and comparing these curves to the experimental data, we can determine that the Rabi frequencies observed in these experiments are of the order of a few tens of kHz.

In contrast, if Ω_R is of the order of a few MHz, the defect darkens completely within the time of the driving pulse. This is also in disagreement with the experimental data. Thus, we conclude that the Rabi frequency in our experiments is of a few tens to hundreds of kHz.

Furthermore, section 3.A2 shows that we do not see any PL darkening when we perform the time-resolved measurements described in the main text at zero magnetic field. In this case, state 2 in our model corresponds to the orbital state $|G2\rangle$ from the main text. We calculate the population in state 2 after optically driving the system for approximately 500 ms, with Rabi frequencies of the order of a few tens of kHz, and present these results in Fig. 3.A11. We only transfer significant population into 2 (leading to PL darkening) when the optical decay rate into state 2, Γ_{32} is larger than the rate at which the system leaves state 2, Γ_{21}. Since we do not observe any PL darkening, we conclude that $\Gamma_{32} \ll \Gamma_{21}$ such that, within the time of our measurements, no significant population is transferred into the orbital state $|G_2\rangle$, and the presence of this state does not influence our measured value for the spin T_1.

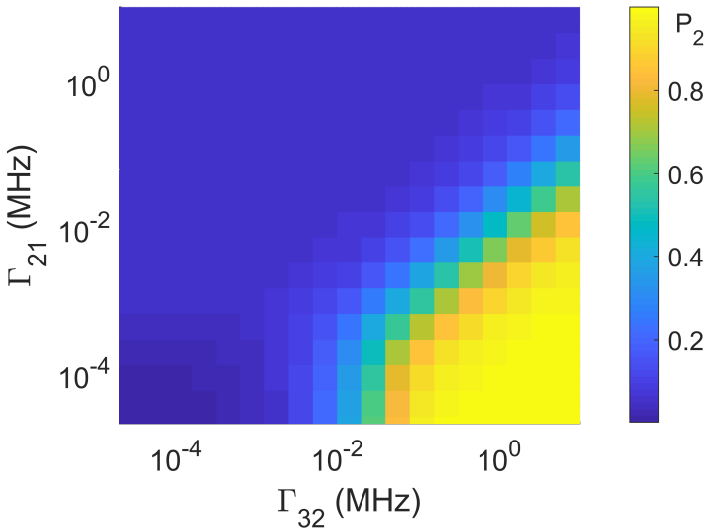

Figure 3.A11: Optical pumping into orbital state $|G2\rangle$ Significant population is only transferred into $|G2\rangle$ when $\Gamma_{32} \gg \Gamma_{21}$.

3.A6 T_1 vs Temperature

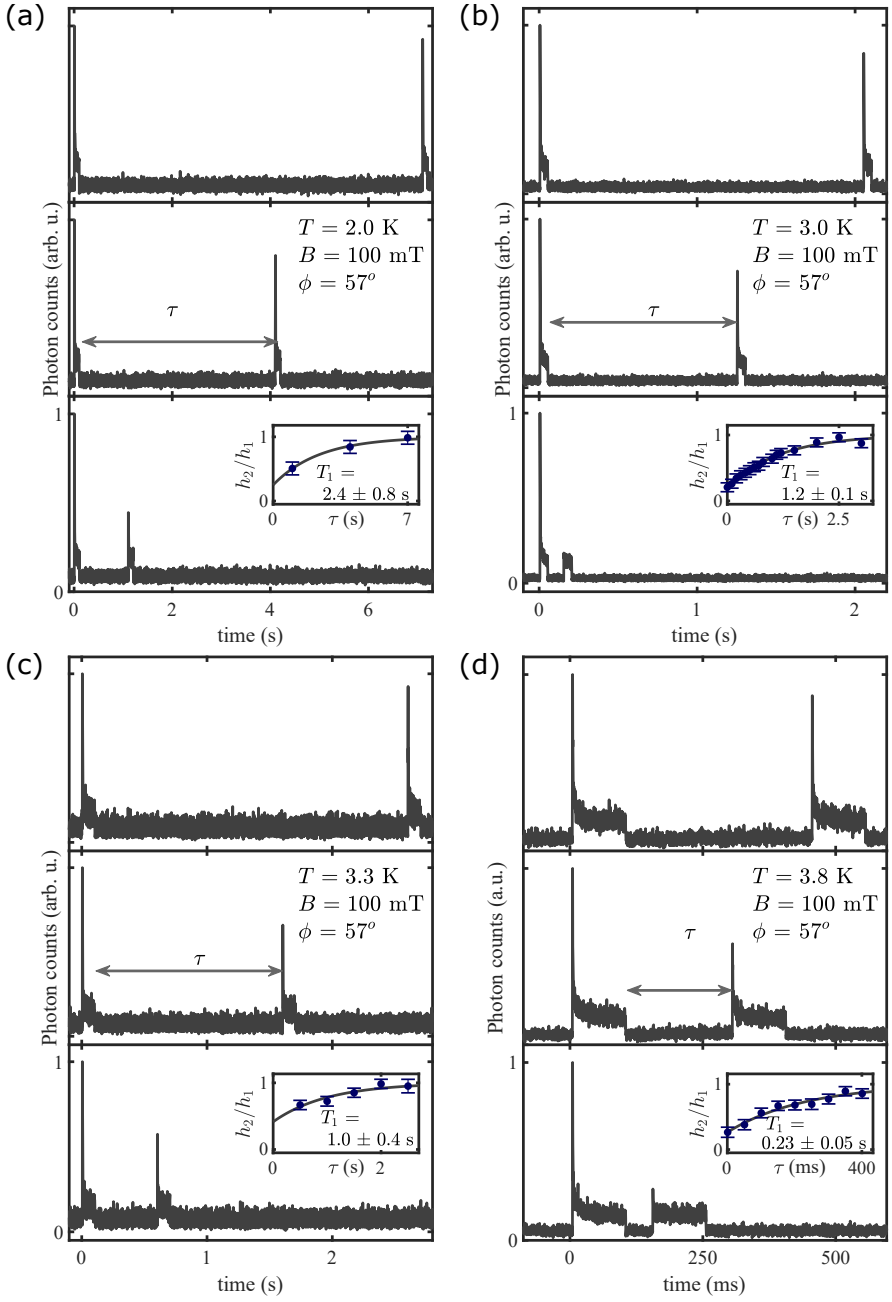

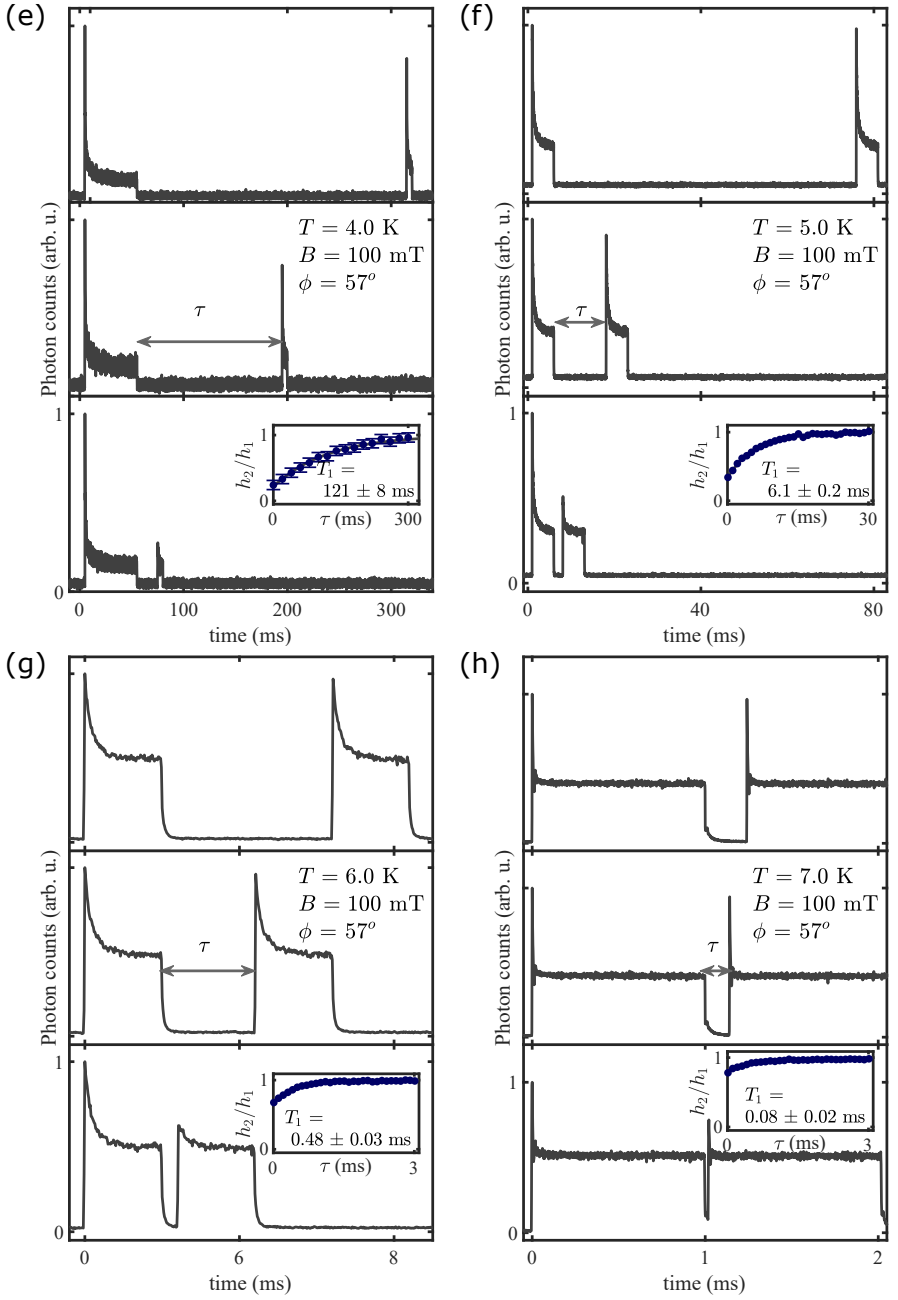

Figure 3.A12: Spin-flip times at various temperatures. For the 5-7 K measurements the error bars on the h_2/h_1 datapoints in the inset are smaller than the marker size and thus not shown.

3.A7 Fitting of T_1^{-1} vs temperature

The spin-lattice relaxation of single spins of substitutional defects in solid state materials arises from a modulation of the crystal field potential in time due to the presence of phonons, which perturbs the stationary crystal field ($V^{(0)}$) and couples various eigenstates of the time-independent Hamiltonian to each other[20]. Thus, the probability of a spin flip to occur depends largely on the matrix elements of the time-dependent crystal field $V^{(1)}$ between the various electronic levels accessible to the defect. We thus define the terms V_{orb} and V_{vib}, which indicate the order of magnitude of the matrix elements of $V^{(1)}$ connecting $\{|G1\downarrow\rangle, |G1\uparrow\rangle\}$ to $\{|G2\downarrow\rangle, |G2\uparrow\rangle\}$ and $\{|G1_{vib}\downarrow\rangle, |G1_{vib}\uparrow\rangle\}$ respectively (see Fig.1 in main text for definitions).

The direct process, a one phonon interaction driving transitions between states $|G1\downarrow\rangle$ and $|G1\uparrow\rangle$ directly, is expected to show a temperature dependence of the kind $T_1^{-1} \propto (\hbar\omega)^2 |\langle G1\downarrow| V^{(1)} |G1\uparrow\rangle|^2 T$ when $k_B T \gg \hbar\omega$, where $\hbar\omega$ is the Zeeman splitting between the spin sublevels $|G1\downarrow\rangle$ and $|G1\uparrow\rangle$. Since the states $|G1\downarrow\rangle$ and $|G1\uparrow\rangle$ are each other's time-reversal pair and $V^{(1)}$ preserves time-reversal symmetry, the matrix elements $|\langle G1\downarrow| V^{(1)} |G1\uparrow\rangle|$ are identically zero (see section 3.A4). Nonetheless, the presence of a magnetic field or hyperfine interaction perturbs states $|G1\downarrow\rangle$ and $|G1\uparrow\rangle$ by mixing in states higher in energy, in such a way that we expect the direct process to be present with a magnitude roughly proportional to $(\hbar\omega)^4 \frac{|V^{(1)}|^2}{\Delta^2} T$, where $V^{(1)}$ is now the matrix element of the time-dependent crystal field coupling states $|G1\downarrow\rangle$, $|G1\uparrow\rangle$ to a generic excited state $|E\rangle$ lying an energy Δ above $|G1\downarrow\rangle$, $|G1\uparrow\rangle$. All of the excited states shown in Fig. 1(b) are expected to contribute to this process, such that mixing with both the higher KD ($|G2\downarrow\rangle$, $|G2\uparrow\rangle$) and the vibronic states ($|G1_{vib}\downarrow\rangle$, $|G1_{vib}\uparrow\rangle$) should be considered. In this way, we expect a dependence of the kind $T_1^{-1} \propto (\hbar\omega)^4 (\frac{|V_{orb}|^2}{\Delta_{orb}^2} + \frac{|V_{vib}|^2}{\Delta_{vib}^2}) T$.

Additionally, a spin polarization in the defect can decay back to its equilibrium value via two-phonon processes comprising transitions into real (Orbach process) or virtual (Raman process) excited states. The former gives rise to an exponential temperature dependence of the type $T_1^{-1} \propto |\langle G1\downarrow| V^{(1)} |E\rangle \langle E| V^{(1)} |G1\uparrow\rangle| \Delta^3 \exp(-\Delta/k_B T)$ in the limit of $\Delta \gg k_B T$, where Δ is the energy difference between a generic excited state $|E\rangle$ and the KD $|G1\downarrow\rangle$, $|G1\uparrow\rangle$. Orbach processes relative to transitions into states $|G2\downarrow\rangle$, $|G2\uparrow\rangle$ are expected to give rise to a strong temperature dependence at temperatures below 1 K and saturate at higher temperatures, when $\Delta_{orb} \sim k_B T$, and its exponential behavior is thus not visible in our data. In contrast, Orbach processes relative to transitions into vibronic levels are expected to contribute significantly to the temperature dependence of T_1^{-1} at

a few K, since $\Delta_{vib} \sim 10$ meV $\gg k_B T$ between 2 and 8 K (Fig. 1(d)) .Thus, we expect the Orbach process to give rise to a temperature dependence of the kind $T_1^{-1} \propto |V_{vib}|^2 \Delta_{vib}^3 \exp(-\Delta_{vib}/k_B T)$.

Finally, second order Raman processes give rise to a temperature dependence of the kind $T_1^{-1} \propto |V^{(1)}|^4 T^5$ when $\Delta \ll k_B T$, or $T_1^{-1} \propto (\frac{|V^{(1)}|}{\Delta})^4 T^9$ when $\Delta \gg k_B T$, where Δ is the energy difference between levels $\{|G1\downarrow\rangle, |G1\uparrow\rangle\}$ and a generic level $|E\rangle$ which is coupled to $|G1\downarrow\rangle$, $|G1\uparrow\rangle$ via $V^{(1)}$. Thus, since $\Delta_{orb} \sim k_B T$, Raman processes involving states $|G2\downarrow\rangle$, $|G2\uparrow\rangle$ are expected to show a $|V_{orb}|^4 T^5$ dependence, whereas Raman processes involving virtual transitions into the vibronic levels $|G1_{vib}\downarrow\rangle$, $|G1_{vib}\uparrow\rangle$ are expected to contribute a term $(\frac{|V_{vib}|}{\Delta_{vib}})^4 T^9$ to T_1^{-1}.

We fit the data in Fig. 3 of the main text to a model of the type $T_1^{-1} = C_D T + C_R T^n + C_O \exp(-\Delta/k_B T) + \Gamma_0$, where $C_{D,R,O}$, Δ and Γ_0 are fitting parameters, and $n = 5, 9$. The parameter Γ_0 is included to account for temperature independent processes of spin relaxation. The fit quality does not improve significantly if we consider $n = 9$ instead of $n = 5$ for the Raman process involved. Thus, we are unable to determine which levels are involved in the Raman transitions responsible for spin relaxation between 3 and 4 K. In either case, however, the exponential increase of the spin relaxation rate above 4 K is accounted for by an Orbach process where two phonons drive transitions between the ground state $|G1\rangle$ and the its vibrational excited state $|G1_{vib}\rangle$ flipping its spin. From the fit, we extract $\Delta_{vib} \approx 6.5 \pm 1$ meV, consistent with the energies of the phonon-coupled states responsible for the PSB emission in the photoluminescence spectrum.

Whereas the parameters C_O and Δ can be determined with large accuracy (errors of $\sim 0.1\%$) due to the undisputable exponential behavior of the relaxation rate at higher temperatures, this is not the case for parameters C_D, Γ_0 and C_R. At low temperatures, there is a large trade-off between the coefficients C_D and Γ_0 – which in turn modify the magnitude of C_R – and various combinations of direct, temperature independent, and Raman processes can fit our data well. For example, a fit with C_D fixed to zero yields an increase of 6% in the root-mean-squared value of the residuals of the fit, and an increase of 62% in the value of Γ_0 and 15% in the value of C_R. On the other hand, a fit with Γ_0 fixed to zero yields an increase of 13% in the rms of the residuals of the fit, an increase of 250% in the value of C_D and a decrease of 30% in the value of C_R. Nonetheless, this uncertainty in the fit does not change the fact that, owing to the long spin-relaxation times in this range, all of the three processes must be relatively slow for these defects.

Finally, we note that the data can also be fit by a power law model of the type $T_1^{-1} = \alpha T + \beta T^\gamma$, with $\gamma \approx 13$. Spin-lattice relaxation of this type

has been previously reported for heavy ions in solid state environments [31]. In that work, a Raman process is observed with a power dependence with $\gamma \approx 11 > 9$. They justify the large power observed by noting that the spin sublevels in the KD are not exactly each other's time-reversal conjugate, in such a way that the 'Van Vleck' cancellation does not happen completely [20]. We exclude this as a relevant model in our case due to the fact that the power dependence necessary to explain our data is much higher, with $\gamma \approx 13$. Additionally, the consistency of Δ_{vib} observed by fitting the data with the energies observed in the PSB of the PL spectrum indicates that the rapid increase of the relaxation rate observed above 4 K is indeed related to exponential Orbach processes involving $|G1_{vib}\downarrow\rangle$, $|G1_{vib}\uparrow\rangle$.

3.A8 Estimating T_2

Our goal here is to estimate the rate of decoherence induced by phonon-driven transitions between the two orbital states, $|G1\rangle$ and $|G2\rangle$. We know that transitions between these levels are largely spin conserving. Nonetheless, these transitions introduce decoherence in the ground-state spin sublevels $|G1\downarrow\rangle$, $|G1\uparrow\rangle$ since the Zeeman splitting and, therefore, the Larmor precession rate of the electronic spin differs between states $|G1\rangle$ and $|G2\rangle$. Thus, the spin-coherence time of the defect will be limited by phonon-driven transitions between the two orbital states, which happen at a rate $\nu_{G1\rightarrow G2}$. In order to obtain an estimate for the contribution of this process to $T_{2,lim}$, we must obtain an estimate for the transition rate between the two orbital states, $\nu_{G1\rightarrow G2}$, given by

$$\nu_{G1\rightarrow G2} = \frac{B_{G1-G2}}{\exp(\Delta_{orb}/k_B T) - 1}, \tag{3.5}$$

where Δ_{orb} is the energy difference between $|G1\rangle$ and $|G2\rangle$, and B_{G1-G2} is the Einstein coefficient for transitions between the two orbital doublets.

We can obtain an estimate for the value of B_{G1-G2} from the T_1 data presented in Fig. 3 of the main text. In order to do this, we start out by estimating a limit to the order of magnitude of the Orbach processes involving the orbital excited state $|G2\rangle$. Subsequently, we compare these values with the expression obtained by Harris and Yngvesson in Ref. [33] to describe Orbach processes where the upwards and downwards transition rates into the relevant excited state differ significantly. This is compatible with our model, if we assume that one of those transitions is spin conserving (fast rate), whereas the other one is spin flipping (slow rate).

Based on their model, we obtain an expression for the rate of Orbach transitions between the two spin eigenstates of $|G1\rangle$ given by

$$\nu_{relaxation} = 2\Big(\frac{B_{1\downarrow-2\downarrow}B_{1\uparrow-2\downarrow}}{B_{1\downarrow-2\downarrow}+B_{1\uparrow-2\downarrow}}\frac{B_{1\downarrow-2\uparrow}B_{1\uparrow-2\uparrow}}{B_{1\downarrow-2\uparrow}+B_{1\uparrow-2\uparrow}}\Big) \frac{1+0.5\exp(-\Delta_{orb}/k_BT)}{\exp(\Delta_{orb}/k_BT)+\exp(-\Delta_{orb}/k_BT)}, \tag{3.6}$$

which reduces to the familiar $\exp(-\Delta_{orb}/k_BT)$ when $k_BT \ll \Delta_{orb}$. Here, $B_{1\downarrow-2\downarrow}$ and $B_{1\uparrow-2\uparrow}$ correspond to the Einstein coefficients for spin-coserving transitions, whereas $B_{1\uparrow-2\downarrow}$ and $B_{1\downarrow-2\uparrow}$ correspond to Einstein coefficients for spin-flipping transitions. We rewrite this in terms of the Einstein coefficient for the total transition probability between $|G1\rangle$ and $|G2\rangle$ B_{G1-G2}, and factors that represent the proportion of spin-flipping (f) and spin-conserving (c) transitions, such that $f + c = 1$

$$\nu_{relaxation} = 4fcB_{G1-G2}\frac{1+0.5\exp(-\Delta_{orb}/k_BT)}{\exp(\Delta_{orb}/k_BT)+\exp(-\Delta_{orb}/k_BT)}. \tag{3.7}$$

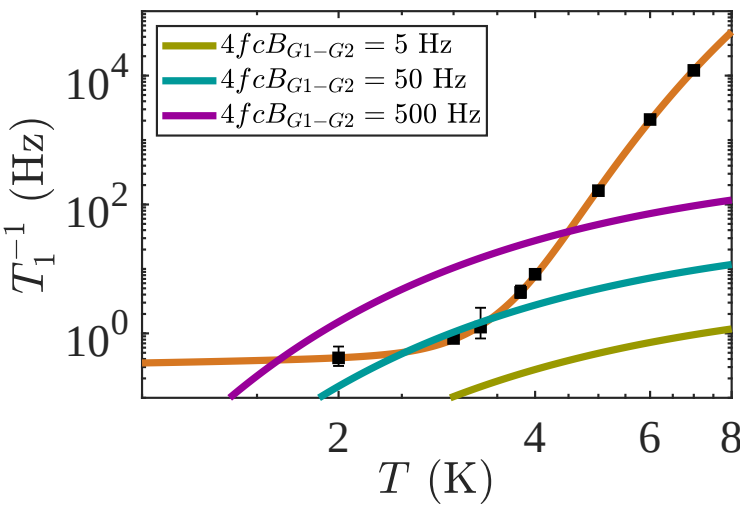

Figure 3.A13: Estimating a limit for T_2 from T_1. Orbach processes between $|G1\rangle$ and $|G2\rangle$ happen with a prefactor $4fcB_{G1-G2}$ smaller than 50 Hz (see main text).

Figure 3.A13 shows the T_1 temperature dependence of the Mo defect, compared to the contribution of Orbach processes involving $|G2\rangle$ with various prefactors $4fcB_{G1-G2}$. In our experimental data, we see no signature

of exponential increase of the spin-flip rate at the relevant temperatures (that is, between 2 and 4 K), leading us to conclude that Orbach processes involving $|G2\rangle$ do not contribute significantly to T_1. These Orbach processes must happen with a prefactor that is at most $4fcB_{G1-G2} = 50$ Hz.

We conservatively assume that $4fcB_{G1-G2} = 50$ Hz. To obtain the product fc, we use the data and model presented in the appendix of chapter 2 (section 2.A4) to describe the ratio of the peaks in two-laser spectroscopy experiments. There, the product fc for spin-flipping and spin-conserving transitions between ground and optically excited state corresponds to the intensity of the Λ line squared, $\sim 0.05^2$ for this configuration of magnetic field. We recognize that the excited state of interest here, $|G2\rangle$, is different from the excited state of interest in that work, $|E\rangle$. Nonetheless, we expect from our model that taking this value leads to an underestimation of the product fc. Since B_{G1-G2} is inversely proportional to both fc and $T_{2,lim}$, this will lead to an underestimation of the limit of $T_{2,lim}$. Taking $fc = 0.05^2$, yields $B_{G1-G2} \approx 5$ kHz. Based on Eq. 3.5, this corresponds to a limit of $T_{2,lim}$ on the order of milliseconds at 4 K.

CHAPTER 4

Electromagnetically induced transparency in inhomogeneously broadened divacancy defect ensembles in SiC

O. V. Zwier*, T. Bosma*, X. Yang, W. J. Brinkhuis, D. O'Shea, A. R. Onur, T. Oshima, N. T. Son, C. H. van der Wal

Abstract

Electromagnetically induced transparency (EIT) is a phenomenon that can provide strong and robust interfacing between optical signals and quantum coherence of electronic spin. In its archetypical form, mainly explored with atomic media, it uses a (near-)homogeneous ensemble of three-level systems, in which two low-energy spin-$\frac{1}{2}$ levels are coupled to a common optically excited state. We investigated the implementation of EIT with c-axis divacancy color centers in silicon carbide. While this material system has attractive properties for quantum device technologies with near-IR optics, implementing EIT needs addressing of new issues. In particular, the ground and optically excited state have a spin-1 level structure, the optical transition shows a relatively large inhomogeneity, and it is unknown whether the solid-state environment provides additional spin dephasing upon strong optical driving. We could establish EIT in weak static magnetic fields. We modeled the observed EIT spectrums using a master equation in Lindblad form with up to five levels. This provides values for the optical and spin decay parameters, and insight in how three-level EIT is influenced by additional levels. Our work provides understanding of EIT in a multi-level system with significant inhomogeneity, and we show that EIT with the divacancy material system can be applied for quantum technologies.

4.1 Introduction

The phenomenon of electromagnetically induced transparency (EIT) is well-studied for atomic media. It allows for applications in areas such as sensing[1–5], atomic clocks[6], low intensity non-linear optics[7–11], topological photonics[12] and coherent photon storage for quantum memories[13–19]. Although many examples of near-perfect EIT exist for atomic ensembles[20–23], achieving this for solid-state system is more challenging due to material inhomogeneities and interactions with the more complex environment. However, solid-state systems promise easier scalability and compatibility with existing technology platforms and may offer an advantage from the fact that quantum emitters in solids are at fixed locations in space. EIT can be established in solid-state systems by *e.g.* using defect ensembles in crystal lattices as artificial atoms. Examples are rare-earth doped crystals[24–26] and the nitrogen-vacancy center in diamond[27,28].

Here we show signatures of EIT in divacancy defect ensembles in silicon carbide. Its mature status in the semiconductor device industry and high compatibility with silicon-based electronics make SiC a promising platform for many electro-optical applications. Divacancies in SiC have been shown to exhibit long spin-coherence times[29] and they allow mapping of electronic spin states onto nuclear spins[30,31], both at room temperature. Divacancy quantum emitters can be addressed in many ways. In recent years examples have been demonstrated of optical control[29,32,33], charge-state control[31], spin-phonon interaction[34] and electrical and mechanical control[35]. However, implementing EIT control for divacancies in SiC may still provide challenges. For instance, it known that these defect ensembles have significant inhomogeneous broadening for the optical transition, even for the highest material quality currently envisioned[36–40]. The zero-phonon lines can be considered narrow for a solid-state system, but the inhomogeneous width still exceeds the natural linewidth by about a factor thousand. Moreover, the triplet ground state enforces the use of additional optical fields to prevent the system from getting optically pumped into a dark level. Generally, such auxiliary fields add to the total dephasing of the system. Here we provide an experimental check whether EIT of sufficient quality for quantum technologies can be engineered in this material system.

We study EIT in an ensemble of c-axis divacancy spins in 4H-SiC with inhomogeneous broadening of the zero-phonon line that we indeed observe to be a factor thousand larger than the natural linewidth, while this ratio is often close to one for atomic systems[20,23]. We apply a weak static magnetic field to tune the spin splittings of the $S = 1$ ground state and the excited states. This enables us to employ the EIT control laser to also counteract any

unwanted optical spin-pumping into the third ground-state level. A three-level Λ system can then be formed from the remaining two ground-state spin levels and one of the excited-state levels. For studies on ensembles of quantum emitters the c-axis divacancy in SiC is of unique interest given that all defects in the ensemble have identical orientation when one works with a single crystal (this is not the case for NV centers in diamond, or the basal plane divacancy studied in the work of Ref. [32]).

In order to extract relevant decay and dephasing parameters from these measurements we analyze models for EIT by solving the master equation in Lindblad form, where inhomogeneous broadening is taken into account. We show that in many cases the probe absorption for a multi-level system can be reliably modeled by considering only a three-level system. Obviously, this analogy loses accuracy when multiple Λ systems are addressed simultaneously in the ensemble of even a single defect. We find experimental signatures of such cases, that come forward as double EIT features within a single homogeneous absorption feature (see below), or asymmetries for EIT features that would be symmetric for a three-level system with only strong inhomogeneous broadening. We can use these observations for more accurate determination of system parameters from fitting. For this, we fit the traces obtained with a five-level model, and extract the ensemble averaged ground-state dephasing rate and excited-state decay rate.

We will start by introducing our experimental methods and the sample. Next, the experimental manifestation of EIT in inhomogeneous systems with a complex level structure is presented. These results will be analyzed in detail using models based on three-level and five-level systems. Finally, we will demonstrate the occurrence of double EIT where multiple windows for coherent population trapping exist within the absorption linewidth of a homogeneous subensemble. We end this work with a discussion of the question whether high-quality EIT can be engineered for quantum technologies in this material system.

4.2 Samples and methods

The sample under study here is a 4H-SiC crystal, which has been electron irradiated and annealed after growth to get an increased divacancy defect concentration. We estimated that the resulting c-axis divacancy concentration was in the range of 10^{15} to 10^{17} cm^{-3} (detailed procedures in Appendix 4.A1). The crystal was inserted into a liquid-helium flow cryostat with windows for optical access, and equipped with a superconducting

magnet system.

The inhomogeneous broadening of the optical transition frequency can be revealed by scanning-laser absorption spectroscopy, where the sample absorption is measured as function of the frequency of a narrow-line excitation laser. Figure 4.1b shows the resulting spectrum where the absorption is measured as a reduction in transmission of the excitation beam (calibrated on non-absorbing parts in the spectrum). Two zero-phonon lines are visible: one at 1.0950 eV (1132 nm) from divacancies at the *(hh)* site[29] (see Fig. 4.1a), and another at 1.0965 eV (1130 nm) from divacancies at the *(kk)* site. Both ZPLs are inhomogeneously broadened by 140 GHz (about a factor 5 broader than the ZPL width for as-grown divacancy ensembles in commercial wafers[32]). In this work we focus on the c-axis divacancies at the *(kk)* sites. Further away in the spectrum, at higher energies, several more ZPLs are visible from *(hk)* and *(kh)* basal-plane divacancies (at 1.12 eV and 1.15 eV, respectively). These are not shown here[35].

Figure 4.1c depicts our method for establishing EIT in the defect ensemble by coherent population trapping (see section 1.4) in the $|g_1\rangle$ and $|g_2\rangle$ spin levels. First of all, signal loss due to optical spin pumping to the $|g_3\rangle$ level needs to be avoided. For an approach that does not rely on adding a third laser field this can be achieved by tuning to conditions where a single control laser simultaneously addresses two transitions close to resonance, *i.e.* the $|g_2\rangle - |e_2\rangle$ and $|g_3\rangle - |e_3\rangle$ transitions in the left panel of Fig 4.1c. In our case we set the magnetic field angle φ relative to the sample c-axis to 57° to achieve this. At this angle the relevant transitions overlap for a broad range of magnetic field magnitudes[41]. Now the control laser prepares the population in the $|g_1\rangle$ spin state. A small misalignment of the magnetic field may cause a nonzero detuning Δ_k for the $|g_3\rangle - |e_3\rangle$ transition. Finally, a probe laser with variable frequency detuning relative to the control laser is used to excite from $|g_1\rangle$ to the shared excited state $|e_2\rangle$, completing the Λ system and enabling the establishment of EIT upon two-photon resonance. See Appendix 4.A2 for details on measuring the probe absorption. Throughout this chapter we will use the wording *two-laser detuning* to indicate the frequency difference between the probe and control laser. Additionally, we use *two-photon detuning* δ to indicate the detuning from two-photon resonance.

The inhomogeneous broadening of the transition frequency causes the control-laser detuning Δ to be distributed throughout the ensemble. Moreover, due to this broadening there is also a part of the ensemble that is closer to resonance the with Λ_2 system depicted in the right panel of Fig. 4.1c. This system has a different Δ_k^* value for the additional detuning from the $|g_3\rangle - |e_2\rangle$ transition. Both the Λ_1 and Λ_2 systems will always be

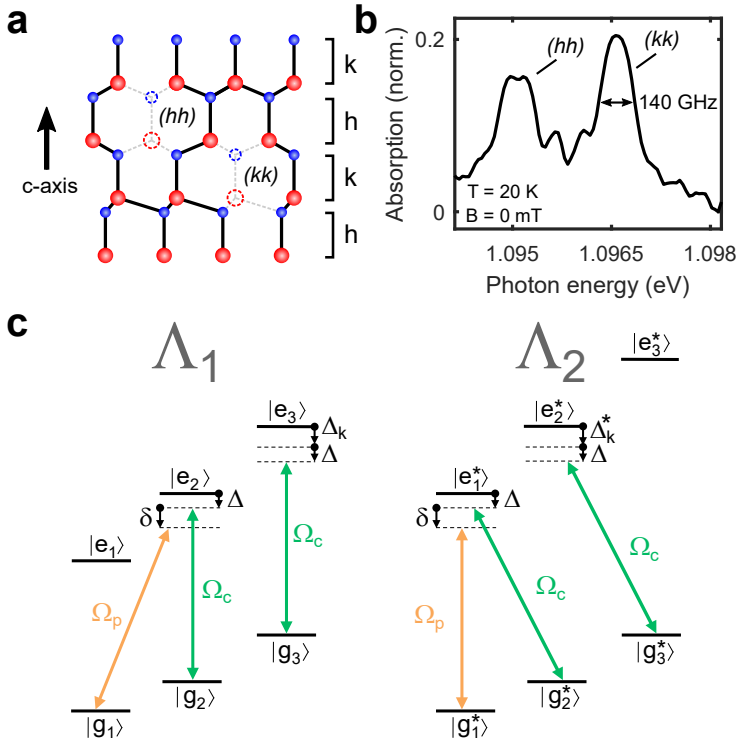

Figure 4.1: The c-axis divacancies in 4H-SiC. a) Schematic of the 4H-SiC lattice along the growth axis (c-axis), illustrating the occurrence of (hh) and (kk) c-axis divacancy defect centers. Ensembles of (kk) divacancies are under study in this work. **b)** Results of scanning-laser absorption spectroscopy that show the zero-phonon lines of the (hh) and (kk) c-axis divacancies. The (kk) divacancy shows an inhomogeneous broadening of 140 GHz. **c)** Schematic of two Λ schemes that occur in our experiments. These can be driven such that optical spin pumping into a third ground-state level is counter acted. Due to the relatively large inhomogeneous broadening of the optical transition in our system, Λ_1 and Λ_2 occur in different subensembles and are driven simultaneously. Here Ω_p and Ω_c denote the probe- and control-laser Rabi frequency, respectively (simplified notation, the actual values differ for each transition). The control-laser detuning for the transition to the common excited state upon Λ-scheme driving is denoted as Δ, and the probe-laser detuning from two-photon resonance as δ. Finally, Δ_k and Δ_k^* depict the additional detunings for parallel laser driving from $|g_3\rangle$ and $|g_3^*\rangle$ to the most strongly coupled excited state, for the scheme with Λ_1 and Λ_2, respectively.

addressed simultaneously, albeit in different subensembles.

4.3 EIT in two-laser spectroscopy

In order to identify the lambda systems we perform a two-laser magnetospectroscopy scan where the absorption is measured versus both two-laser detuning and magnetic-field strength for fields at angle $\varphi = 57°$ with the c-axis. Here we set the frequency of one laser in the middle of the ZPL, while scanning the second laser frequency relative to the first. Note that throughout this work we always consider the absorption of the probe laser unless specified otherwise. The results are shown in Fig. 4.2a. In this range three clear two-laser absorption features (TLAF) are visible with linewidths close to the homogeneous linewidth of the underlying transitions (about a factor 1000 narrower than the inhomogeneous ZPL width). Earlier spectroscopy work on this material systems[41] established that the c-axis ZPLs concern a transition between levels with a $S = 1$ spin structure, with spin Hamiltonians in a form that is set by the symmetry of the defect. Upon relating the detuning and magnetic field values of the TLAF peaks to the energy eigenvalues of the theoretical Hamiltonian (see Appendix 4.A3), we identify the features labeled L_1 and L_2 as resulting from two Λ driving schemes, where two ground-state levels are coupled to one excited state. The L_3 feature results from driving a scheme where the lasers couple the ground-state levels to separate excited-state levels, so EIT does not occur here.

Figure 4.2b shows a two-laser scan around the L_1 feature at higher resolution. A sharp EIT dip becomes visible in the center of the absorption peak. Figure 4.2c shows a similar result, but here the EIT feature appears asymmetrically in the TLAF line. Below we will discuss that this occurs when the magnetic field is not perfectly at the angle that gives optimal overlap for two transitions. Figure 4.2d shows the TLAF for the L_3 absorption line. Here no EIT feature was observed (also not upon increasing the power).

The lower limit for the control-laser Rabi frequency for complete EIT is well-established, *i.e.* $\Omega_c^2 > \Gamma_e \gamma_g$ with Γ_e the excited-state decay rate and γ_g ground-state dephasing rate[42] (we assume the pure dephasing of the excited state γ_e to be small). Upon considering inhomogeneous broadening beyond Γ_e this limit becomes[20]

$$\Omega_c^2 > \Delta_I \gamma_g \tag{4.1}$$

with Δ_I the FWHM inhomogeneous broadening. To test the power dependence of EIT in our inhomogeneously broadened ensemble we scan around L_1 with several control-laser powers while keeping the probe-laser power fixed. The results are shown in Fig. 4.2e. The EIT dip becomes deeper at larger control-beam power, but the limit for complete EIT was

not reached. Additionally, power broadening is visible, both for the TLAF and the EIT dip.

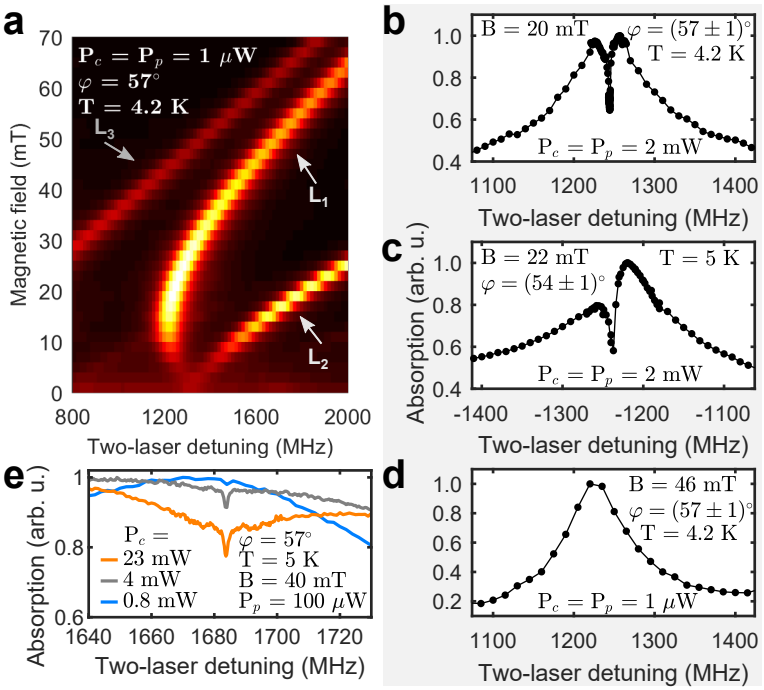

Figure 4.2: EIT in two-laser absorption spectroscopy. **a)** Two-laser magneto-spectroscopy scan at low laser powers revealing three clear absorption lines for the probe beam. Lines L_1 and L_2 correspond to Λ driving schemes, whereas L_3 corresponds to a non-Λ type of driving scheme. **b-d)** Absorption versus two-laser detuning for several scenarios: **b)** For a magnetic field angle $\varphi = 57^o$ that yields an optimal Λ system with $\Delta_k \approx 0$ (L_1 in panel **a**), resulting in a symmetric EIT dip. **c)** For a slightly misaligned magnetic field $\varphi = 54^o$ where $\Delta_k \neq 0$, resulting in an asymmetric EIT dip. **d)** For a magnetic field where a non-Λ system is driven resonantly (L_3 in panel **a**). **e)** Control-beam power dependence of EIT in probe-beam absorption (for the Λ system corresponding the L_1 in panel **a**). At larger control-beam power the EIT becomes more pronounced.

4.4 Model for inhomogeneous broadening

We now first turn to modeling the influence of the large inhomogeneous broadening of the optical transition on EIT, in an approach that assumes an ensemble of three-level systems. The five-level Λ_1 system of Fig. 4.1c can often be accurately depicted by a three-level system with an additional ground-state dephasing term to account for population transfer between $|g_1\rangle$

Table 4.1: Parameter choices for three-level Λ scheme model.

parameter	value (Hz)
Γ_e	10^7
γ_e	0
Γ_g	10^4
γ_g	10^5
Ω_c	$3 \cdot 10^6$
Ω_p	10^4
Δ	variable
δ	variable

or $|g_2\rangle$ and $|g_3\rangle$, and an additional excited-state decay term to account for the decay from the excited states towards the $|g_3\rangle$ level. We will focus on the effect that the large inhomogeneous broadening has on the EIT lineshape. Note that we will later show later that this three-level approach is too simplified for describing EIT features that occur when the magnetic field is not perfectly aligned ($\Delta_k \neq 0$) or when more than the three laser couplings (two within the three-level system, and one for counter-acting optical pumping into $|g_3\rangle$) in Fig 4.1c play a role.

For the Λ system made up by $|g_1\rangle$, $|g_2\rangle$ and $|e_2\rangle$ we set up a Master equation in Lindblad form. We solve for the density matrix considering the parameters listed in table 4.1. It is assumed that the decay rate Γ_e from the excited state towards either ground state is equal.

A comparison between absorption traces with EIT features for a homogeneous ensemble and an inhomogeneous one, where the optical transition is normally distributed with a FWHM of 100 GHz, is shown in Fig 4.3a. The overall absorption peak for the inhomogeneous ensemble broadens by a factor 2.66. This width is saturated, as increasing the FWHM of the distribution does not increase this factor any further. Additionally, the EIT dip becomes shallower and narrower. This is clear from the EIT limits in Eq. 4.1, but we will demonstrate its origin in more detail in the next paragraph.

The fading of the EIT dip can be clarified by looking at the separate homogeneous subensembles that make up the inhomogeneous ensemble. Figure 4.3b shows probe-absorption traces for several values of the optical transition detuning Δ throughout the ensemble. Note that Δ is defined zero when the control laser is resonant with the $|g_2\rangle - |e_2\rangle$ transition (see Fig. 4.1c). The inhomogeneous trace of Fig. 4.3a is summation of these

separate traces for all Δ values, weighted with the distribution throughout the ensemble.

In the case of an ensemble of actual three-level systems with large inhomogeneity for the optical transition, that is addressed near the middle of its inhomogeneous optical line, an EIT feature will always be symmetric in a TLAF. This is unlike EIT with a homogeneous ensemble, where (for detunings $\Delta \lessapprox \Gamma_e$) the EIT dip will appear asymmetrically in the homogeneous line when Δ is nonzero. The inhomogeneous case remains symmetric because there are effectively equal amounts of blue- and red-detuned subensembles, averaging out the asymmetry. Still, the results in Fig. 4.3 show that the EIT line shape for the inhomogeneous case is strongly influenced by the homogeneous subensembles that contribute with a detuning $\Delta > \Gamma_e$. For the EIT spectrum of such a homogeneous subensembles, the lineshape splits up. Around $\delta = -\Delta$ a linear absorption peak appears as the probe laser becomes resonant with the $|g_1\rangle - |e_2\rangle$ transition. Close to two-photon resonance ($\delta = 0$) an asymmetric peak with both Raman and EIT characteristics appears[42]. Since this peak edge is closer to $\delta = 0$ than the edge of the homogeneous EIT dip, the effect for the total inhomogeneous EIT dip is that it gets narrowed. The tail of the Raman-EIT peak at $\delta = 0$ causes the shallower EIT dip for the inhomogeneous ensemble. In Fig. 4.3c the Δ dependence of the probe-absorption traces is shown at higher resolution (darker means higher absorption), revealing the evolution of the absorption line along Δ and δ.

4.5 Model for asymmetric EIT in TLAF lines

Although the appearance of off-center EIT is quite common for ensembles with small inhomogeneous broadening[20], its occurrence in the TLAFs of ensembles with large broadening is less trivial. As discussed above, all asymmetry will be averaged out when considering the response of the full ensemble. Still, Fig. 4.2c shows an example of how we observed asymmetric EIT features in TLAFs. We ascribe this to to imperfect overlap of the $|g_2\rangle - |e_2\rangle$ and $|g_3\rangle - |e_3\rangle$ transitions in the Λ_1 system in Fig. 4.1c. Here we explain how this is possible

As a result of the imperfect overlap, the Δ_k detuning becomes nonzero. This gives two subensembles where the population in the $|g_1\rangle$ state is highest, and thus the overall probe absorption as well. These are the subensembles around $\Delta = 0$ and $\Delta = -\Delta_k$. For small nonzero Δ_k this causes an asymmetry in the TLAF lineshape. This can be seen in Fig. 4.4. Here inhomogeneous probe-laser absorption traces, as obtained from solving the

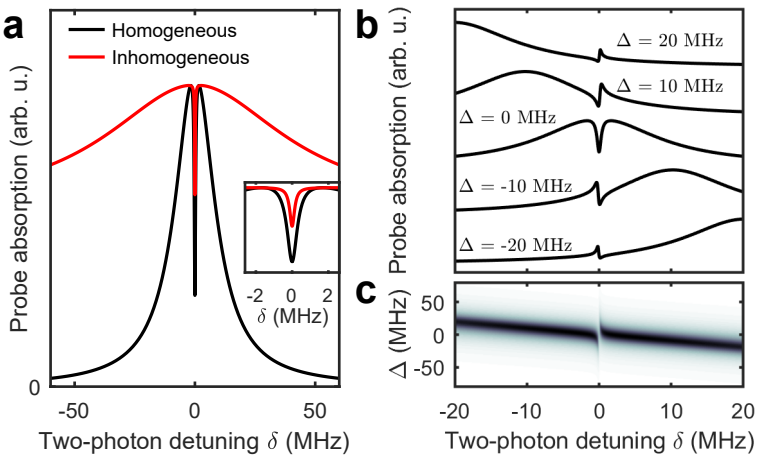

Figure 4.3: Simulation results for effect of inhomogeneous broadening on EIT lineshapes. In an ensemble where the optical transition frequency is inhomogeneously broadened (Gaussian distribution), the control-laser detuning Δ is distributed accordingly. The total response is then probe absorption integrated over all defects with their respective detuning Δ. **a)** Simulated EIT traces for (black) a homogeneous ensemble on resonance ($\Delta = 0$), and for (red) an inhomogeneously broadened ensemble (FWHM = 100 GHz). The inset shows the EIT dip at higher resolution. **b)** Traces for homogeneous ensembles at various control-laser detunings Δ (vertical offset for clarity). At larger Δ the peak splits up in a linear probe-laser absorption peak at $\delta = -\Delta$, and a small absorption feature with both EIT and enhanced Raman characteristics close to two-photon resonance. A weighted summation of these traces for all Δ values yields the red curve in panel **b**. **c)** Probe-laser absorption, calculated for a homogeneous ensemble, as a function of control-laser detuning Δ and detuning from two-photon resonance δ (given a certain Δ). Darker means increased absorption. The traces in panel **b** are horizontal sections of this panel.

Master equation for a five-level system, are shown for several values of Δ_k. At larger Δ_k the two peaks separate, resulting in an absorption peak around $\delta = 0$ with an on-center EIT dip, and a linear absorption peak around $\delta = \Delta$. For cases where Δ_k is comparable to the homogeneous linewidth Γ_e the TLAF lineshape becomes asymmetric with an off-center EIT dip.

4.6 Double EIT in five-level system

We will now demonstrate and study the occurrence of double EIT features within a single TLAF line . For this we tuned to conditions where coherent population trapping occurs for two sets of ground states within the same TLAF width. Since this addresses two Λ schemes in parallel, it allows

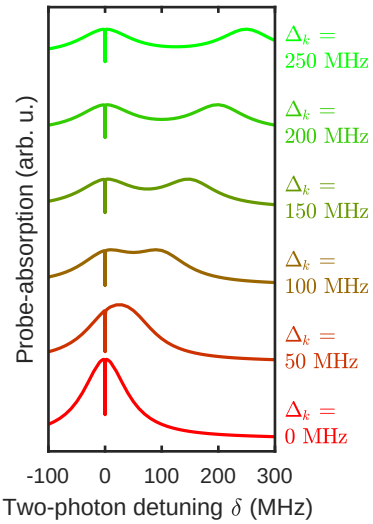

Figure 4.4: Asymmetric EIT in five-level system. Simulated probe-absorption traces for an inhomogeneously broadened ensemble (FWHM = 100 GHz) at various Δ_k values (vertical offset for clarity). Imperfect matching of the $|g_2\rangle - |e_2\rangle$ and $|g_3\rangle - |e_3\rangle$ transition frequency defines the Δ_k value (see the Λ_1 scheme in Fig. 4.1c). For nonzero Δ_k, there are two subensembles in the range of control-laser detuning values Δ where high probe-laser absorption occurs: One at $\Delta = 0$, yielding the absorption peak with EIT feature around $\delta = -\Delta = 0$, and another at $\Delta = -\Delta_k$, showing a linear absorption peak around $\delta = -\Delta = \Delta_k$. For low and nonzero Δ_k the total probe absorption thus becomes asymmetric.

for more accurate fitting, in particular when also covering a wide range of dependence on laser intensities in a single fitting approach.

The occurrence of such double EIT features will be explained by considering at first the full six-level system with laser driving as in Fig. 4.5a. Here several additional transitions are driven close to resonance. Generally, in a six-level system with triplet ground and excited state a total of nine Λ systems are possible (three sets of ground states with couplings to one of three excited states). By keeping the detuning between $|g_1\rangle$ and the other two ground-state levels large enough we ensure that the probe-laser exclusively couples close to resonance with transitions out of $|g_1\rangle$. Similarly we keep $|e_1\rangle$ detuned far enough such that no ground-state levels are coupled to it resonantly. This leaves only four Λ schemes.

Figure 4.5b highlights these four three-level Λ schemes, which are responsible for double EIT. The Λ schemes that couple $|g_1\rangle$ and $|g_2\rangle$ to a shared excited state (left panel) exhibit coherent population trapping for $\delta = 0$ just like before. Additionally, the schemes that couple $|g_1\rangle$ and $|g_3\rangle$ to

a shared excited state (right panel) have this interference at $\delta = \Delta_k - \Delta_{54}$ (defined in Fig. 4.5a). In order to observe a double EIT dip the conditions need to be tuned carefully: Δ_k needs to be large enough to get off-center EIT, while at the same time the magnetic field is weak enough to have all four Λ systems of Fig. 4.5b occur within the typical linewidth of the two-laser absorption peak. To achieve this, we set the angle φ between the magnetic field and c-axis to 87° and tune the magnitude to 6 mT.

Figure 4.5c-d show the probe-absorption versus two-laser detuning as obtained experimentally. Two EIT dips are visible, one on either sides of the absorption peak. For Fig. 4.5c we varied the optical powers of both the control and probe lasers simultaneously. This allows us to extract the Rabi frequencies and dipole strengths for the various transitions accurately. We fit the traces to a model for a five-level scheme considering all transitions depicted in Fig 4.5a and in the presence of 140 GHz inhomogeneous broadening (see Appendix 4.A5 for further details). We get for the excited-state decay rate $\Gamma_e = (2.7 \pm 0.4)$ MHz, for the Rabi frequency $\Omega_c = (7.4 \pm 0.6)$ MHz at 1 mW control beam power, and for the ensemble-averaged ground-state dephasing rate $\gamma_g^* = (0.23 \pm 0.06)$ MHz. The inverse of the latter value represents the ensemble-averaged ground-state coherence time $T_2^* = (4.3 \pm 0.5)$ μs, which is slightly longer than what was found in microwave experiment on similar ensembles of c-axis divacancy defects [29]. This indicates that the additionally driven transitions in our experiment do not significantly add to spin dephasing, thus confirming the feasibility of establishing EIT in this triplet ground-state system.

Next, we study the temperature dependence of double EIT. The results are shown in Fig. 4.5d for temperatures between 2 and 12 K (at ten times higher control laser power). The overall TLAF linewidth broadens upon increasing the temperature, while the EIT contrast diminishes. We fit the traces to the same model as before, but now keeping the transition dipole strengths and related Rabi frequencies fixed. From these fits we find that the ground-state dephasing rate γ_g does not change significantly with temperature. Although it is not possible to separately determine the excited-state decay rate Γ_e and pure dephasing rate γ_e from our two-laser absorption traces, we are able to relate them to the broadening of the TLAF linewidth. This is because it is known that changes in the divacancy PL spectrum in this temperature range are only moderate, both for the ZPL and the photon sideband emission [43]. Furthermore, it is not plausible that the electric dipole moment of the involved transitions shows a significant change at these temperatures. This points to the conclusion that the line broadening in Fig. 4.5d is mainly due to an increase in pure dephasing for this optical transition. We find that below 6 K the overall TLAF linewidth is

mainly governed by the excited-state decay rate Γ_e, while the pure dephasing rate γ_e starts to dominate above this temperature.

4.7 Discussion and conclusions

Now that we have found values for the ground-state dephasing rate γ_g and the actual control-laser Rabi frequency Ω_c we can estimate the intensity requirements for complete EIT using Eq. 4.1. For our system with 140 GHz inhomogeneous broadening the minimum value for Ω_c should be 180 MHz, which corresponds to a control laser power of 600 mW. These optical powers could not be achieved in our experimental setup. However, higher intensities could be realized when using single-mode SiC waveguides (see also Chapter 5). For example, using a divacancy-doped waveguide with a mode diameter of 5 μm would yield a 200x larger intensity compared to our experiments. In this way complete EIT could be achieved whilst still using tunable diode lasers in the milliwatt range.

In this work we investigated EIT in a divacancy ensemble in SiC. Although its rich level structure and relatively large inhomogeneous broadening could hamper the occurrence of high-quality EIT, we showed that this not necessarily the case. We have established EIT in these solid-state ensembles with large broadening of the transition frequency. We also demonstrated that, for a system with an $S = 1$ ground state, spin pumping into a dark level can be countered without additional spin dephasing. Finally, the triplet ground state might allow for more intricate single-photon storage techniques, as we show that it allows for double EIT. Here two separate windows for EIT are addressable within the same system, while requiring only a single control field.

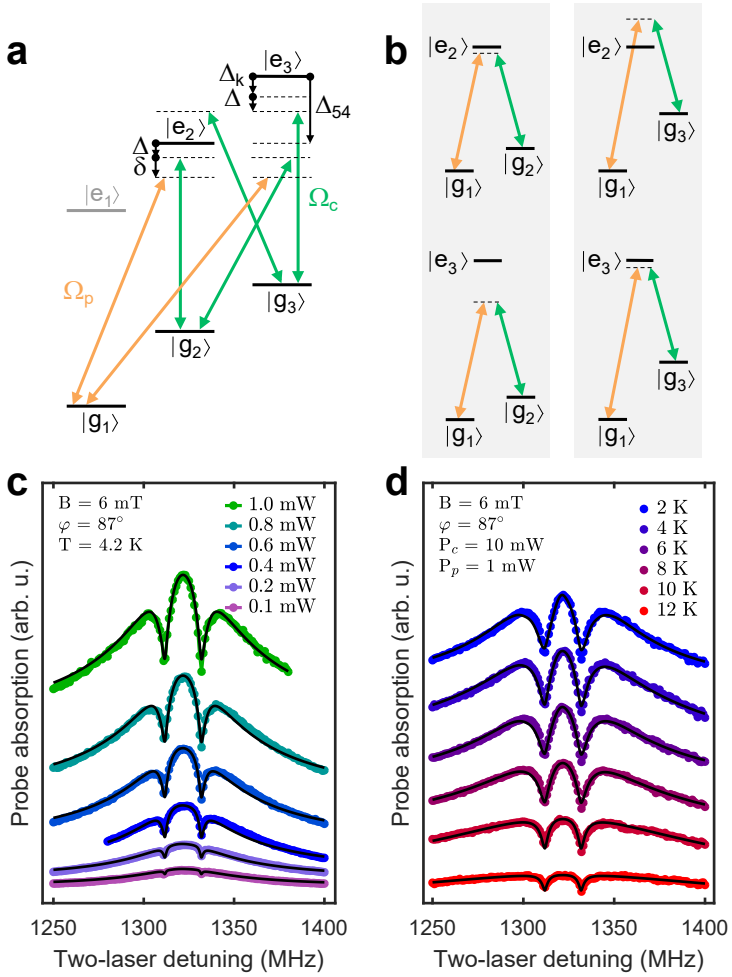

Figure 4.5: Double EIT features in two-laser absorption spectroscopy. a) At low magnetic field strength two Λ systems are driven simultaneously. As a result, two EIT features appear within the same peak in two-laser absorption spectroscopy. One EIT feature (at $\delta = 0$ in panel **a**) originates from interference of transitions from the $|g_1\rangle$ and $|g_2\rangle$ states (left panel in **b**). The other EIT feature appears when $\delta = \Delta_k - \Delta_{54}$ and comes from interference of transitions from the $|g_1\rangle$ and $|g_3\rangle$ states (right panel in **b**). **c)** Laser-power dependence of double EIT. Control- and probe-laser powers are varied simultaneously. The black traces in panels **b-c** are fits obtained from solving the master equation in Lindblad form for the five-level system and laser couplings from panel **a** (and in the presence of 140 GHz inhomogeneous broadening for the optical transition). **d)** Temperature dependence of double EIT. A vertical offset has been added for clarity in panels **c** and **d**.

Acknowledgements

We thank J. A. H. Adema for help with modeling and M. de Roosz, J. G. Holstein, T. J. Schouten, H. H. de Vries and H. Adema for technical support. Early discussions with Prof. Erik Janzén leading to initiation of this study are gratefully acknowledged. Financial support was provided by ERC Starting Grant 279931, the EU H2020 project QuanTELCO (862721), the Zernike Institute BIS program, the Swedish Research Council grants VR 2016-04068 and VR 2016-05362, the Knut and Alice Wallenberg Foundation (KAW 2018.0071), and the Carl Tryggers Stiftelse för Vetenskaplig Forskning grant CTS 15:339

Author contributions

The project was initiated by C.H.W. and O.V.Z. SiC materials were grown and prepared by N.T.S. and T.O. Experiments were performed by O.V.Z and X.Y, and D.O. and A.R.O. contributed to setting up experiments. Data analysis was performed by T.B., O.V.Z., X.Y., W.J.H. and C.H.W. For writing the manuscript, T.B., O.V.Z. and C.H.W. had the lead, and O.V.Z. and T.B. are co-first author.

References

[1] Nagel, A. *et al.* Experimental realization of coherent dark-state magnetometers. *EPL* **44**, 31 (1998).

[2] Yudin, V. *et al.* Vector magnetometry based on electromagnetically induced transparency in linearly polarized light. *Phys. Rev. A* **82**, 033807 (2010).

[3] Sedlacek, J., Schwettmann, A., Kübler, H. & Shaffer, J. Atom-based vector microwave electrometry using rubidium Rydberg atoms in a vapor cell. *Phys. Rev. Lett.* **111**, 063001 (2013).

[4] Holloway, C. L. *et al.* Electric field metrology for SI traceability: Systematic measurement uncertainties in electromagnetically induced transparency in atomic vapor. *J. Appl. Phys.* **121**, 233106 (2017).

[5] Vafapour, Z. Near infrared biosensor based on Classical Electromagnetically Induced Reflectance (Cl-EIR) in a planar complementary metamaterial. *Opt. Commun.* **387**, 1–11 (2017).

[6] Vanier, J. Atomic clocks based on coherent population trapping: a review. *Appl. Phys. B* **81**, 421–442 (2005).

[7] Harris, S. & Hau, L. V. Nonlinear optics at low light levels. *Phys. Rev. Lett.* **82**, 4611 (1999).

[8] Gorshkov, A. V., Otterbach, J., Fleischhauer, M., Pohl, T. & Lukin, M. D. Photon-photon interactions via Rydberg blockade. *Phys. Rev. Lett.* **107**, 133602 (2011).

[9] Peyronel, T. *et al.* Quantum nonlinear optics with single photons enabled by strongly interacting atoms. *Nature* **488**, 57–60 (2012).

[10] Firstenberg, O. *et al.* Attractive photons in a quantum nonlinear medium. *Nature* **502**, 71–75 (2013).

[11] Chang, D. E., Vuletić, V. & Lukin, M. D. Quantum nonlinear opticsphoton by photon. *Nat. Photonics* **8**, 685 (2014).

[12] Ozawa, T. *et al.* Topological photonics. *Rev. Mod. Phys.* **91**, 015006 (2019).

[13] Duan, L.-M., Lukin, M., Cirac, J. I. & Zoller, P. Long-distance quantum communication with atomic ensembles and linear optics. *Nature* **414**, 413–418 (2001).

[14] Boyd, R. W., Gauthier, D. J., Gaeta, A. L. & Willner, A. E. Maximum time delay achievable on propagation through a slow-light medium. *Phys. Rev. A* **71**, 023801 (2005).

[15] Khurgin, J. B. Optical buffers based on slow light in electromagnetically induced transparent media and coupled resonator structures: comparative analysis. *J. Opt. Soc. Am.* **22**, 1062–1074 (2005).

[16] Kimble, H. J. The quantum internet. *Nature* **453**, 1023 (2008).

[17] Lvovsky, A. I., Sanders, B. C. & Tittel, W. Optical quantum memory. *Nat. Photonics* **3**, 706 (2009).

[18] Novikova, I., Walsworth, R. L. & Xiao, Y. Electromagnetically induced transparency-based slow and stored light in warm atoms. *Laser & Photonics Reviews* **6**, 333–353 (2012).

[19] Gorniaczyk, H., Tresp, C., Schmidt, J., Fedder, H. & Hofferberth, S. Single-photon transistor mediated by interstate Rydberg interactions. *Phys. Rev. Lett.* **113**, 053601 (2014).

[20] Gea-Banacloche, J., Li, Y.-q., Jin, S.-z. & Xiao, M. Electromagnetically induced transparency in ladder-type inhomogeneously broadened media: Theory and experiment. *Phys. Rev. A* **51**, 576 (1995).

[21] Morigi, G., Eschner, J. & Keitel, C. H. Ground state laser cooling using electromagnetically induced transparency. *Phys. Rev. Lett.* **85**, 4458 (2000).

[22] Lukin, M. Colloquium: Trapping and manipulating photon states in atomic ensembles. *Rev. Mod. Phys.* **75**, 457 (2003).

[23] Ma, J., Shi, P., Qian, X., Shang, Y. & Ji, Y. Optical spin noise spectra of Rb atomic gas with homogeneous and inhomogeneous broadening. *Scientific reports* **7**, 1–7 (2017).

[24] Ham, B. S., Hemmer, P. & Shahriar, M. Efficient electromagnetically induced transparency in a rare-earth doped crystal. *Opt. Commun.* **144**, 227–230 (1997).

[25] Turukhin, A. *et al.* Observation of ultraslow and stored light pulses in a solid. *Phys. Rev. Lett.* **88**, 023602 (2002).

[26] Hedges, M. P., Longdell, J. J., Li, Y. & Sellars, M. J. Efficient quantum memory for light. *Nature* **465**, 1052–1056 (2010).

[27] Acosta, V. M., Jensen, K., Santori, C., Budker, D. & Beausoleil, R. G. Electromagnetically induced transparency in a diamond spin ensemble enables all-optical electromagnetic field sensing. *Phys. Rev. Lett.* **110**, 213605 (2013).

[28] Doherty, M. W. *et al.* The nitrogen-vacancy colour centre in diamond. *Phys. Rep.* **528**, 1–45 (2013).

[29] Koehl, W. F., Buckley, B. B., Heremans, F. J., Calusine, G. & Awschalom, D. D. Room temperature coherent control of defect spin qubits in silicon carbide. *Nature* **479**, 84–87 (2011).

[30] Seo, H. *et al.* Quantum decoherence dynamics of divacancy spins in silicon carbide. *Nature communications* **7**, 1–9 (2016).

[31] de las Casas, C. F. *et al.* Stark tuning and electrical charge state control of single divacancies in silicon carbide. *Appl. Phys. Lett.* **111**, 262403 (2017).

[32] Zwier, O. V., O'Shea, D., Onur, A. R. & van der Wal, C. H. All–optical coherent population trapping with defect spin ensembles in silicon carbide. *Sci. Rep.* **5**, 10931 (2015).

[33] Falk, A. L. *et al.* Optical polarization of nuclear spins in silicon carbide. *Phys. Rev. letters* **114**, 247603 (2015).

[34] Whiteley, S. J. *et al.* Spin–phonon interactions in silicon carbide addressed by Gaussian acoustics. *Nat. Phys.* **15**, 490–495 (2019).

[35] Falk, A. L. *et al.* Electrically and mechanically tunable electron spins in silicon carbide color centers. *Phys. Rev. Lett.* **112**, 187601 (2014).

[36] Waldermann, F. *et al.* Creating diamond color centers for quantum optical applications. *Diam. Relat. Mater.* **16**, 1887–1895 (2007).

[37] Calusine, G., Politi, A. & Awschalom, D. D. Cavity-enhanced measurements of defect spins in silicon carbide. *Phys. Rev. Applied* **6**, 014019 (2016).

[38] Zhang, J. L. *et al.* Hybrid group IV nanophotonic structures incorporating diamond silicon-vacancy color centers. *Nano letters* **16**, 212–217 (2016).

[39] Spindlberger, L. *et al.* Optical properties of vanadium in 4H silicon carbide for quantum technology. *Phys. Rev. Applied* **12**, 014015 (2019).

[40] Wolfowicz, G. *et al.* Vanadium spin qubits as telecom quantum emitters in silicon carbide. *Science Advances* **6**, eaaz1192 (2020).

[41] Zwier, O. V. *Two-laser spectroscopy and coherent manipulation of color-center spin ensembles in silicon carbide.* Zernike Institute PhD thesis series, ISSN 1570-1530 (University of Groningen, 2016).

[42] Fleischhauer, M., Imamoglu, A. & Marangos, J. P. Electromagnetically induced transparency: Optics in coherent media. *Rev. Mod. Phys.* **77**, 633 (2005).

[43] Magnusson, B. *et al.* Excitation properties of the divacancy in 4 H-SiC. *Phys. Rev. B* **98**, 195202 (2018).

Appendix

4.A1 Generation of high divacancy concentrations in 4H-SiC

The high concentration of divacancies in the 4H-SiC sample used in this work was generated by irradiating the sample with a 2 MeV electron beam with a dose of $8 \cdot 10^{18}$ cm^{-2}. Generally, this yields a broad range of lattice defects, such as carbon-vacancy, silicon-vacancy centers and divacancies. In order to optimize for the latter, the sample was annealed at 750 °C for 15 minutes. This allowed the carbon and silicon vacancies to diffuse until they form more stable divacancies.

4.A2 Measuring probe-beam absorption

As mentioned in the main text, all reported absorption traces are exclusively from probe absorption. The probe beam is separated from the control and repump beams by means of spatial separation: The beams cross each other in one point within the sample at angles below 5°. After transmission through the sample the probe beam passes through a 1000 nm long-pass filter to filter out any stray repump-beam radiation. Next it passes through a series of irises to filter out any stray control-beam radiation. Finally, it is captured by an InGaAs photodetector.

To increase the signal-to-noise ratio of the absorption measurements we implement a cross-modulation method. Here, the control beam passes through a chopper wheel at 270 Hz prior to entering the sample. If the control beam is blocked by the chopper, the ensemble of divacancies is not optimally prepared in the $|g_1\rangle$ state (see Fig. 4.1c), thus the probe-beam will be absorbed less. Conversely, if the control beam passes trough the chopper freely, the population will be well prepared for probe absorption and the transmission of the probe beam will drop. In order to extract this 270 Hz modulation, the InGaAs photodetector signal is fed to a lock-in amplifier. The resulting signal (lock-in R) now exclusively represents probe-beam absorption. Before plotting we normalize the results to the peak value for each trace.

Additionally, a 770 nm pulsed 10 mW repump laser is present to counter bleaching of the optical signal due to charge-state switching of the divacancies. This beam passes through the same chopper wheel as the probe beam and the alignment is tuned to have the on-off cycles of both beams in anti phase with each other. This way the influence of the repump beam on the coherence is strongly reduced when EIT is established.

4.A3 Pumping schemes for TLAF lines

We relate the two-laser absorption features (TLAF) depicted in Fig. 4.2a in the main text to pumping schemes in a six-level system by solving the ground and excited-state Hamiltonian for the energy eigenvalues. We have for the ground (excited) state Hamiltonian $H_{g(e)}$

$$H_{g(e)} = g_{g(e)}\mu_B \mathbf{B}\cdot\mathbf{S} + hD_{g(e)}S_z^2, \tag{4.2}$$

where we use $D_g = 1.3$ GHz and $D_e = 0.5$ GHz, as was found in[41]. For the ground (excited) state we set $g_{g(e)} = 2$. It is assumed that both the ground and excited state are $S = 1$ triplets. Fig. 4.A6a shows the energy splittings of the ground and excited-state spin sublevels. In total nine different optical transitions are possible between the ground and excited states. Their frequencies relative to the zero-phonon line are depicted in Fig. 4.A6b, grouped per ground-state level by color. It can be seen that beyond 30 mT two transition pairs overlap for a broad range of magnetic field values. Below 30 mT just one pair of transitions overlaps: the $|g_2\rangle - |e_2\rangle$ and $|g_3\rangle - |e_3\rangle$ transitions (control laser transitions for Λ_1 in Fig. 4.1c in the main text). The other pair consists of the $|g_2\rangle - |e_1\rangle$ and $|g_3\rangle - |e_2\rangle$ transitions (control laser transitions for Λ_2 in Fig. 4.1c in the main text).

From these transitions we can find the detunings and magnetic field magnitudes at which to expect TLAF features. These are plotted in Fig. 4.A6c for the TLAFs from Fig. 4.2a in the main text. We can relate the L_1-L_3 features to the pumping schemes depicted in Fig. 4.A7a-c. Note that, in the case of negative detuning, the probe and control lasers are effectively swapped. L_1 and L_2 both have a unique pumping scheme. The L_3 line may be caused by three different pumping schemes that lie closely together, one occurs at positive detuning, the other two at negative detuning. All these pumping schemes for Λ_3 still allow for optical spin pumping into $|g_1\rangle$ as no transition is driven from that level. This explains why that line shows up dimmer in Fig 4.2a and why we were unable to observe an EIT dip in its TLAF.

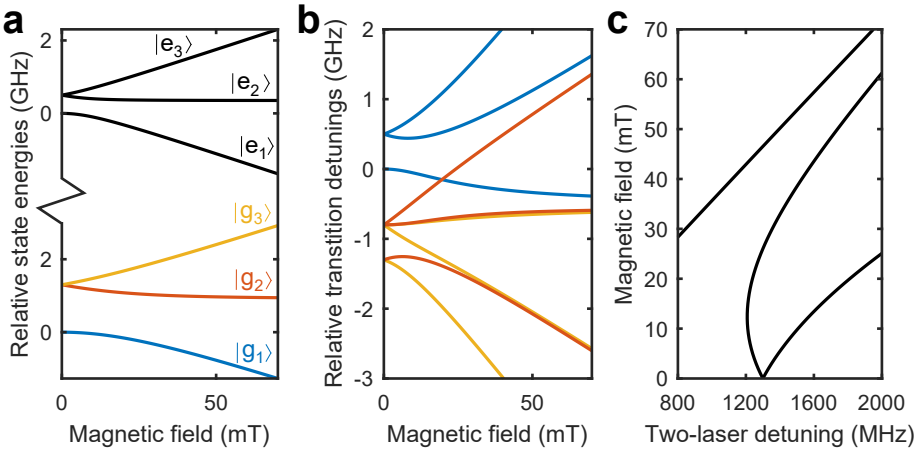

Figure 4.A6: Level splittings and transition energies. **a)** Energy level splittings versus magnetic field for the divacancy ground and excited-state sublevels. Energies for the ground (excited) state are relative to $|g_1\rangle$ ($|e_1\rangle$) **b)** Transition energies for the nine possible transitions between the ground and excited-state sublevels. The blue, orange, yellow lines correspond to transitions from the $|g_1\rangle$, $|g_2\rangle$, $|g_3\rangle$ ground-state levels, respectively. Frequencies are relative to the $|g_1\rangle - |e_1\rangle$ transition frequency **c)** Magnetic field and detuning dependence of several TLAFs obtained from combining transitions in **b)**.

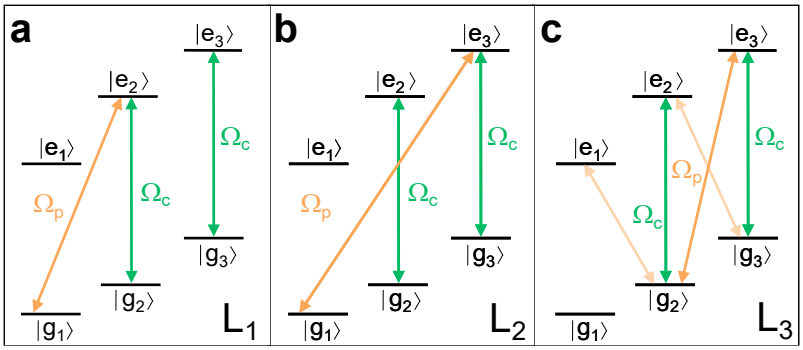

Figure 4.A7: Pumping schemes for the observed TLAFs. **a-c)** Pumping schemes for the L_1-L_3 features in Fig. 4.A6c, respectively. Three different schemes are responsible of L_3, the opaque orange probe-beam transition occurs at positive detuning, the two translucent orange probe-beam transitions occur at negative detuning.

4.A4 Density matrix for three-level system

We derive the density matrix ρ for a three-level system by using the master equation in Lindblad form

$$\dot{\rho} = -\frac{i}{\hbar}[H, \rho] + \mathcal{L}(\rho), \tag{4.3}$$

where H represents the Hamiltonian of the system and $\mathcal{L}(\rho)$ the Lindblad superoperator containing the decay and dephasing terms of the system. Figure 4.A8 shows the three-level system with the relevant laser couplings at hand.

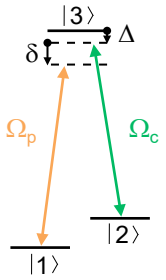

Figure 4.A8: Three-level system for master equation. This three-level systems with laser couplings for the probe and control laser is used as an example for the derivation of the density matrix from the master equation in Lindblad form. The control-laser detuning Δ from resonance with the $|2\rangle - |3\rangle$ transition and the detuning δ from two-photon resonance are depicted.

We first derive the Hamiltonian H for this system, we get

$$H = H_0 + V, \tag{4.4}$$

where H_0 represents the Hamiltonian of the unperturbed system and V the perturbations from the optical driving fields. We get

$$\mu = \begin{pmatrix} \hbar\omega_1 & 0 & 0 \\ 0 & \hbar\omega_2 & 0 \\ 0 & 0 & \hbar\omega_3 \end{pmatrix}, \tag{4.5}$$

where $\hbar\omega_i$ represents the energy for state i. For the perturbation V we use the electric dipole approximation to get [14]

$$V = -\mu E, \tag{4.6}$$

where E is the applied optical field and μ the dipole operator. We have dropped the vector notation by assuming that the optical electric fields are

always perfectly aligned with the dipole moments. The field E with an applied probe and control laser is

$$E = \frac{1}{2}\left[E_p e^{i\omega_p t} + E_c e^{i\omega_c t} + c.c.\right], \tag{4.7}$$

with E_p (E_c) the electric field amplitude and ω_p (ω_c) the frequency of the probe (control) field. For the dipole operator μ we ignore the static dipoles and the transition dipole for the $|1\rangle - |2\rangle$ transition (and vice versa), as it is far off resonance. We get

$$\mu = \begin{pmatrix} 0 & 0 & \mu_{13} \\ 0 & 0 & \mu_{23} \\ \mu_{31} & \mu_{32} & 0 \end{pmatrix}. \tag{4.8}$$

Now we can construct the full Hamiltonian H. We can reduce the number of driving terms for the perturbation part by applying the rotating wave approximation (RWA). For this, we first need to convert to the interaction picture by performing the unitary transformation $H' = UHU^\dagger$ with

$$U = e^{iH_0 t/\hbar} = \begin{pmatrix} e^{i\omega_1 t} & 0 & 0 \\ 0 & e^{i\omega_2 t} & 0 \\ 0 & 0 & e^{i\omega_3 t} \end{pmatrix}. \tag{4.9}$$

Since we have $\omega_p \approx \omega_3 - \omega_1$ and $\omega_c \approx \omega_3 - \omega_2$, some off-diagonal terms in H evolve far slower than others. The fast terms become irrelevant in this picture. Upon ignoring these terms and rotating back to the Schrödinger picture we get

$$H = \begin{pmatrix} \hbar\omega_1 & 0 & -\frac{\mu_{13}E_p}{2} e^{i\omega_p t} \\ 0 & \hbar\omega_2 & -\frac{\mu_{23}E_c}{2} e^{i\omega_c t} \\ -\frac{\mu_{32}E_p}{2} e^{-i\omega_p t} & -\frac{\mu_{32}E_c}{2} e^{-i\omega_c t} & \hbar\omega_3 \end{pmatrix}. \tag{4.10}$$

For compactness, we substitute the Rabi frequencies $\Omega_p = \frac{\mu_{13}E_p}{\hbar} = \frac{\mu_{31}E_p}{\hbar}$ and $\Omega_c = \frac{\mu_{23}E_c}{\hbar} = \frac{\mu_{32}E_c}{\hbar}$

$$H = \hbar \begin{pmatrix} \omega_1 & 0 & -\frac{\Omega_p}{2} e^{i\omega_p t} \\ 0 & \omega_2 & -\frac{\Omega_c}{2} e^{i\omega_c t} \\ -\frac{\Omega_p}{2} e^{-i\omega_p t} & -\frac{\Omega_c}{2} e^{-i\omega_c t} & \omega_3 \end{pmatrix}. \tag{4.11}$$

In order to solve the master equation (Eq. 4.4) we have to get rid of the oscillating terms. This can be done by performing another unitary transformation, converting to a frame that rotates along with these

oscillating terms. Let's call the density operator in this rotating frame σ and relate it to ρ by $\rho = R\sigma R^\dagger$ a proper choice for R is then a diagonal matrix where

$$R_{ii} = \begin{cases} e^{i\omega_k} & \text{if only one field } \omega_k \text{ couples to level } i \\ 1 & \text{otherwise} \end{cases} . \tag{4.12}$$

For our three-level system we get

$$\begin{pmatrix} e^{i\omega_p t} & 0 & 0 \\ 0 & e^{i\omega_c t} & 0 \\ 0 & 0 & 1 \end{pmatrix} . \tag{4.13}$$

The master equation (Eq. 4.4) now becomes (ignoring the Lindblad superoperator for now)

$$\left(\dot{R}\sigma R^\dagger + R\dot{\sigma}R^\dagger + R\sigma\dot{R^\dagger}\right) = -\frac{i}{h}\left[H, R\sigma R^\dagger\right] . \tag{4.14}$$

This will yield only static terms in the relation between $\dot{\sigma}$ and σ.

Before we can start solving the master equation, we still need the Lindblad superoperator $\mathcal{L}(\sigma)$, which contains the decay and dephasing terms. In this rotating frame it can be defined as follows [14,42]

$$[\mathcal{L}(\sigma)]_{ij} = \begin{cases} \Gamma_{ki}\sigma_{kk} - \Gamma_{ik}\sigma_{ii} & \text{for } i = j \\ -\left[\frac{1}{2}\left(\Gamma_{ik} + \Gamma_{jk}\right) + \gamma_i + \gamma_j\right]\sigma_{ij} & \text{for } i \neq j \end{cases} , \tag{4.15}$$

where Γ_{ij} represents the decay rate from level $|i\rangle$ to $|j\rangle$, γ_i and the dephasing rate for level $|i\rangle$. Note that the Einstein summation convention is used here.

Now we can write the components of $\dot{\sigma}$ as a system of nine coupled equations like $\dot{\sigma} = M\sigma$. We set $\Gamma_{12} = \Gamma_{21} = \Gamma_g \neq 0$ and $\Gamma_{31} = \Gamma_{32} = \Gamma_e \neq 0$, all other decay terms are set to zero. For the dephasing terms we set $\gamma_1 = 0$ to consider all phases relative to state $|1\rangle$. Furthermore, since in our system the decay rate from the excited state is several orders of magnitude larger than the dephasing rate γ_3, we ignore it by setting $\gamma_3 = 0$. Additionally, we substitute the control-laser detuning $\Delta = \omega_3 - \omega_2 - \omega_c$ and the probe-laser detuning $\delta + \Delta = \omega_3 - \omega_1 - \omega_p$. Now we get for our three level system

$$
\begin{bmatrix} \dot{\sigma}_{11} \\ \dot{\sigma}_{12} \\ \dot{\sigma}_{13} \\ \dot{\sigma}_{21} \\ \dot{\sigma}_{22} \\ \dot{\sigma}_{23} \\ \dot{\sigma}_{31} \\ \dot{\sigma}_{32} \\ \dot{\sigma}_{33} \end{bmatrix} =
\begin{pmatrix}
-\Gamma_g & 0 & i\frac{\Omega_p}{2} & 0 & \Gamma_g & 0 & -i\frac{\Omega_p}{2} & 0 & \Gamma_e \\
0 & -i\delta - \Gamma_g - \gamma_2 & i\frac{\Omega_c}{2} & 0 & 0 & 0 & 0 & -i\frac{\Omega_p}{2} & 0 \\
i\frac{\Omega_p}{2} & i\frac{\Omega_c}{2} & -i(\Delta+\delta) - \Gamma_e - \frac{\Gamma_g}{2} & 0 & 0 & i\frac{\Omega_p}{2} & 0 & 0 & -i\frac{\Omega_p}{2} \\
0 & 0 & 0 & i\delta - \Gamma_g - \gamma_2 & 0 & i\frac{\Omega_c}{2} & -i\frac{\Omega_c}{2} & 0 & 0 \\
\Gamma_g & 0 & 0 & 0 & -\Gamma_g & 0 & 0 & -i\frac{\Omega_c}{2} & \Gamma_e \\
0 & 0 & 0 & i\frac{\Omega_p}{2} & i\frac{\Omega_c}{2} & -i\Delta - \Gamma_e - \frac{\Gamma_g}{2} - \gamma_2 & 0 & 0 & -i\frac{\Omega_c}{2} \\
-i\frac{\Omega_p}{2} & 0 & 0 & -i\frac{\Omega_c}{2} & 0 & 0 & i(\Delta+\delta) - \Gamma_e - \frac{\Gamma_g}{2} & 0 & i\frac{\Omega_p}{2} \\
0 & -i\frac{\Omega_p}{2} & 0 & 0 & -i\frac{\Omega_c}{2} & 0 & 0 & i\Delta - \Gamma_e - \frac{\Gamma_g}{2} - \gamma_2 & i\frac{\Omega_c}{2} \\
0 & 0 & -i\frac{\Omega_p}{2} & 0 & 0 & -i\frac{\Omega_c}{2} & i\frac{\Omega_p}{2} & i\frac{\Omega_c}{2} & -2\Gamma_e
\end{pmatrix}
\begin{bmatrix} \sigma_{11} \\ \sigma_{12} \\ \sigma_{13} \\ \sigma_{21} \\ \sigma_{22} \\ \sigma_{23} \\ \sigma_{31} \\ \sigma_{32} \\ \sigma_{33} \end{bmatrix}.
$$

The $\dot{\sigma} = M\sigma$ system of equations can be solved if we define the total population in the system to be unity

$$\sigma_{11} + \sigma_{22} + \sigma_{33} = 1. \tag{4.16}$$

The material susceptibility to the probe laser $\chi(\omega_p)$, and thus its absorption coefficient, is proportional to the σ_{13} component of the density matrix [42].

4.A5 Fitting routine

In similar fashion as in section 4.A4 we derived a system of equations based on the master equation for the five-level system and laser couplings from figure 4.5a in the main text. To include the inhomogeneity of the transition frequency we calculated the probe absorption for a range of single-laser detuning Δ values. The total absorption for the probe beam in the ensemble was computed as a weighted sum, determined by a Gaussian-distributed inhomogeneous width Δ with a FWHM width of 140 GHz. We also accounted in our modeling for the inhomogeneity of the optical intensity throughout the ensemble, given the Gaussian TEM_{00} laser beam shape in the SiC crystal. We assumed perfect beam overlap, and use the experimentally determined values for the beam diameter. All six double EIT traces from the power dependence measurement of Fig. 4.5c in the main text were fit simultaneously to the model with a least-squares method. This way we obtained unique values for the transition dipole moments. For fitting the temperature dependent traces in Fig. 4.5d the transition dipole moments were kept fixed to these values.

CHAPTER 5

Broadband single-mode monolithic waveguides in 4H-SiC

T. Bosma, X. Yang, J. U. Hassan, N. T. Son, C. H. van der Wal

Abstract

Color-center defects in silicon carbide promise optoelectronic quantum applications in several fields, such as computing, sensing and communication. For scaling down and combining these functionalities with the existing silicon device platforms it is crucial to consider SiC integrated optics. In recent years many examples of SiC photonic platforms have been shown, like photonic crystal cavities, film-on-insulator waveguides and micro-ring resonators. However, all these examples rely on separating thin films of SiC from substrate wafers. This introduces significant surface roughness and defects in the material, which greatly affects the homogeneity of the optical properties of color centers. Here we present and test a method of fabricating monolithic single-crystal integrated-photonic devices in SiC: by tuning the carrier concentration. We fabricated monolithic SiC n-i-n junctions where the intrinsic layer acts as waveguide core. We demonstrate the functionality of these samples with propagation losses below 16 dB/cm. These waveguide types allow for addressing color-centers over a broad wavelength range with low strain-induced inhomogeneity of the optical-transition frequencies. Furthermore, we expect that our findings open the road to creating similar SiC waveguides from p-i-n junctions, which will allow for integrated electrostatic and RF control together with high-intensity optical control of defects in silicon carbide.

In recent years silicon carbide has gained renewed interest for quantum technology applications in fields like communication [1–3] and (bio)sensing [4,5]. It was found that color centers in SiC have favorable properties, such as long-lived spin states and possibilities for operation at telecom wavelengths [6]. For scaling down potential optoelectronic quantum applications, integrated photonics are paramount. In silicon carbide it would be simple to combine such architectures with existing silicon and silicon-carbide device platforms.

Though many examples exist of amorphous SiC waveguides [7–9], a high-quality single-crystal material is required in order to get reliable spin-active color centers with predetermined properties [6]. Crystalline waveguides and photonic devices have been fabricated for various SiC polytypes such as photonic crystal cavities with arrays of cylindrical holes in 3C-SiC [10], 4H-SiC film-on-insulator waveguides [11] and micro-ring resonators [8,12].

However, recent studies on color-center defects in silicon carbide, showing combined electrical and optical control of color-center defects in silicon carbide for quantum technologies in p-i-n junctions [3,13–15], have us looking closely at another method for fabricating monolithic SiC waveguides: by carrier-concentration reduction [16]. The main reason for this is that for technologies involving color centers, especially ensemble based, high material purity and low strain inhomogeneity are vital. This grade of material quality can only be achieved when growing 4H-SiC device layers on substrates of the same material. The layers are difficult to separate without loss of homogeneity [8].

In this work we show how junctions from layers with alternating doping concentration can be engineered into single-mode optical waveguides. We fabricated a n-i-n junction planar structure in 4H-SiC as a proof of concept. These devices can be engineered to confine any preferred number of waveguide modes. Notably, the number of allowed modes, as well as their field distributions, are independent of wavelength. We demonstrate the broadband properties single-mode waveguides with core thickness of 4 μm and cladding doping concentration up to 10^{19} cm^{-3}. Our findings can be generalized for p-i-n junction devices, which will allow for RF control of SiC color centers by the AC Stark effect [13,17] along with high-intensity optical control.

5.1 Carrier-concentration reduction

According to the Drude model free charge carriers reduce the refractive index [18–20]. They screen a material from the optical electric field, thereby

lowering the net polarization and thus the index of refraction. As explained in Appendix 5.A1, the influence of free carriers on the refractive index of a medium for a wide range of conditions for 4H-SiC leads to a shift [21,22]

$$\Delta n = -\frac{Ne^2\lambda_0^2}{2\varepsilon_0 n_0 m^* c^2}, \tag{5.1}$$

where N is the concentration of free charge carriers with effective mass m^*, ε_0 is the vacuum permittivity, c the speed of light in vacuum, n_0 the refractive index of the undoped host material, γ the damping constant and λ_0 the vacuum wavelength for which we evaluate the refractive index. Increasing the free-carrier concentration N will decrease the refractive index, allowing for total internal reflection at shallow reflection angles.

5.2 Samples

The planar waveguide samples used in this research are grown on an n^+ 4H-SiC substrate ($8 \cdot 10^{18}$ cm^{-3}). Using epitaxial chemical vapor deposition growth in which the nitrogen concentration for n-type doping could be controlled, first a 4 μm layer of minimally doped (10^{14} cm^{-3}) SiC is grown as the waveguide core. The material was then cleaved along the $[1\bar{1}00]$ direction to yield several samples of 3.2 and 6.9 mm length with very smooth facets. Next, a highly doped layer (10^{19} cm^{-3}) of 2 μm is deposited on top to serve as cladding. According to equation (5.1) the step in index of refraction between the core and cladding is then $\Delta n \approx 3 \cdot 10^{-3}$ for 800 nm TE polarized light where it is assumed that each nitrogen dopant donates one electron to the conduction band.

With this knowledge we can predict the electric field distribution for the optical modes. The expected field distributions for TE and TM modes are shown in Fig. 5.1b [23]. Interestingly, the shape of these modes is wavelength independent due to two competing effects. For increasing wavelengths, the reduction of round-trip phase for the optical field bouncing between the substrate and cladding layers is compensated by the increase in the range of total internal reflection angles [16]. This is discussed in detail in Appendix 5.A3.

5.3 Mode matching

To investigate the functionality of these samples we evaluate the transmission and confinement of a Gaussian laser beam through the sample. For this purpose we use a 700-1000 nm tunable CW Ti:Sapphire laser. For initial

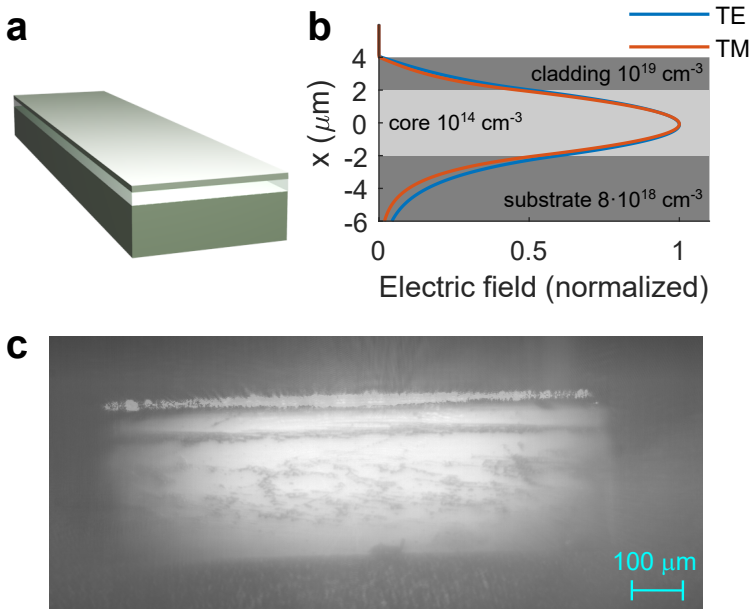

Figure 5.1: Demonstration of waveguiding. **a)** Schematic of a monolithic waveguide sample. On the substrate layer (bottom) a 4 μm core and a 2 μm cladding layer are grown. **b)** Predicted electric field distribution of the fundamental waveguide modes for TE and TM polarization, the distributions are independent of wavelength. **c)** Camera image of the sample end facet with an 800 nm laser coupled into the waveguide layer. It can be seen that the transmission is confined to a layer near the top of the sample.

5

testing we focused an 800 nm beam to a diameter of 4 μm and aligned it to the waveguide layer using a stepper-motor controlled six-axis stage. Figure 5.1c shows a camera image of the sample end facet at optimal transmission. Along the top edge, a bright transmission band is visible, confirming the confinement of the optical field.

We further study the mode matching and coupling efficiency by measuring the transmission versus laser position. The experimental setup for this is shown in figure 5.2. A single-mode fiber attached to a six-axis stage feeds a wavelength-tunable laser to the setup. On the stage the laser beam with 1.2 mm diameter is polarized and focused by an aspheric lens with 4.5 mm focal length. By scanning the position of the stage, the focal point of the laser can be scanned along front facet of sample. The transmission is captured by a photodetector and a camera focused at the sample end facet. We repeat these scans for several wavelengths in order to study the wavelength dependence of the mode matching.

The results for scanning along the optical axis (z) and and sample layers

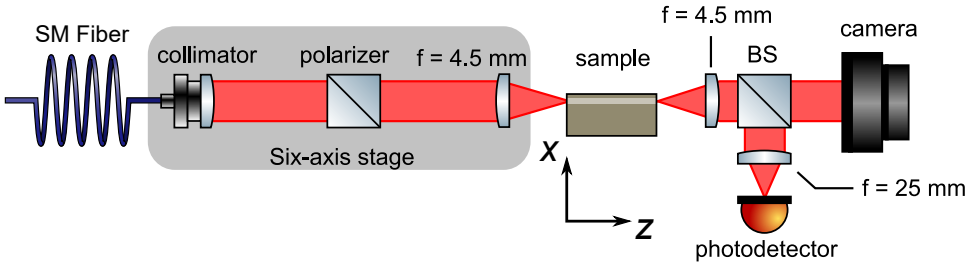

Figure 5.2: Waveguide coupling setup. A laser beam is fed to a six-axis stage by a single-mode fiber. After collimation and polarization it is focused onto a waveguide sample by a 4.5 mm aspheric lens. Half of the intensity of light exiting the sample is focused onto a CMOS camera, the other half is focused into a photodetector. The x- and z- axes are shown.

(x) are shown in figure 5.3 for TE polarization, *i.e.* polarization along the sample plane. The results for TM polarization as well as results for longer wavelengths (up to 1290 nm) can be found in Appendix 5.A2 and , respectively. At the narrowest, the full-width at half maximum (FWHM) for the peaks along x is 1.5 μm, independent of wavelength. Some linear background is visible along z: at higher z more transmission is detected. The reason for this is the fact that we use an aspheric lens to focus light into a planar waveguide. The focused beam will be confined by the planar waveguide in one direction, but will expand freely in the other. As the laser focus is moved towards the collection apparatus upon increasing z, the detection losses due to beam divergence are reduced. Note that the shift of the optimal coupling point along z with varying wavelengths matches with the theoretical focal shift of the aspheric lens in use [24].

Figure 5.4a-b summarizes a few properties of the four wavelength dependent $x - z$ scans from Fig. 5.3. Panel a shows the peak height of the transmission versus position along z relative to the maximum z_0. Panel b shows the full-width at half maximum (FWHM) obtained from fitting the transmission lines along x to Gaussian curves. Both the peak width and height are unaffected by wavelength changes in this range, confirming that the mode distribution within the waveguide core is independent of wavelength. In Fig. 5.4c we show a theoretical prediction of the coupling efficiency for various beam positions at 800 nm. The coupling efficiency profile matches well with the transmission profile from Fig. 5.3b. This estimate was obtained by solving the overlap integral η for optical powers [25]

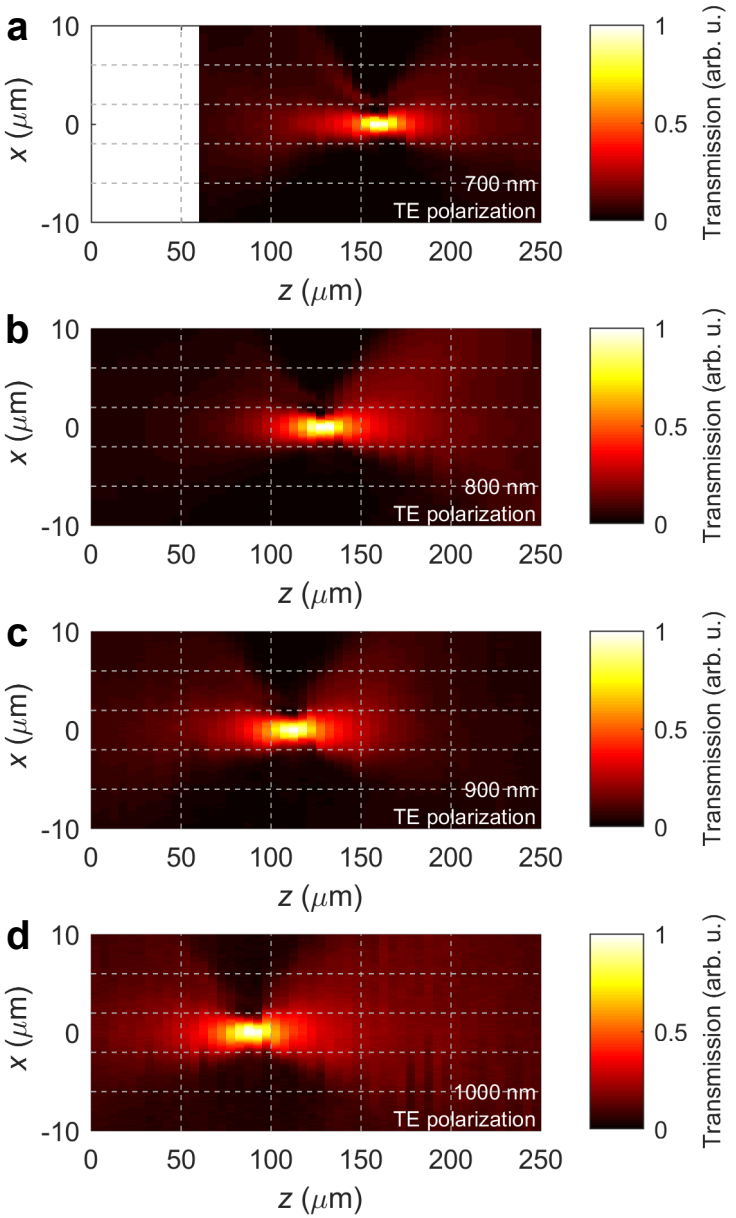

Figure 5.3: Transmission versus laser position. The focus of the coupling lens is scanned along the z-axis and along the sample layers (x-axis). **a-d)** Transmission for 700 - 1000 nm wavelength, respectively.

$$\eta = \frac{|\int E_b^* E_m \mathrm{d}A|}{\int |E_b|^2 \mathrm{d}A \int |E_m|^2 \mathrm{d}A}, \tag{5.2}$$

with E_b the complex electric field of the laser beam and E_m the electric field for the waveguide mode. These electric-field terms were determined based on the experimental-setup parameters and the predicted waveguide mode from Fig. 5.1b, respectively.

We obtained an indication for the propagation losses by comparing the transmission optimal coupling for samples of varied lengths (3.2 and 6.9 mm. We found that for TE polarization the losses vary from $11 - 18$ dB/cm in the $700 - 1000$ nm wavelength range. For TM polarization the losses vary from $11 - 17$ dB/cm in this range.

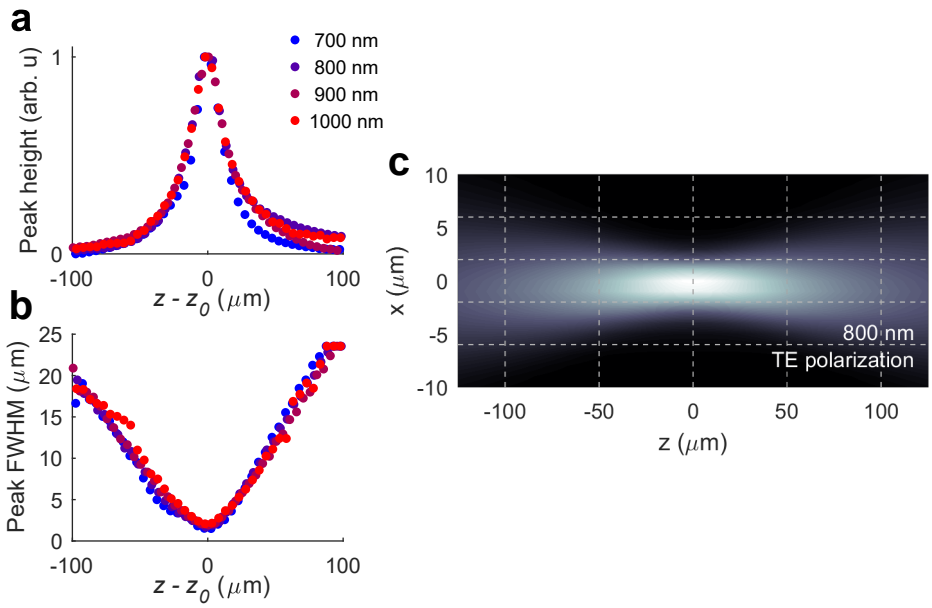

Figure 5.4: Wavelength-independent coupling for TE polarization. a) Peak height versus position along z. **b)** Peak width along x versus position along z. Both the peak width and peak height are obtained from fitting the transmission data in Fig. 5.3 to Gaussian curves along x. **c)** Theoretically predicted coupling efficiency for our experimental setup and waveguides (brighter means higher coupling efficiency).

5.4 Conclusions

In this research we have studied the feasibility of using the carrier-concentration reduction method for fabricating waveguides in single-crystal high-purity 4H-SiC material. We fabricated a monolithic planar waveguide that allows for broadband single-mode operation. Although the propagation losses up to 18 dB/cm will not allow for long-range operation, they are low enough for on-chip applications. At a typical on-chip length scale of 100 μm at most 4.1% of the optical intensity will be dissipated. As follow-up we propose to engineer a p-i-n junction waveguide with color-center defects, such as divacancies or vanadium impurities, in the waveguide core to demonstrate the true potential of these devices.

Acknowledgments

We thank X. Wei, R. H. van der Velde, F. Šimić, R. J. M. Julius, O.V. Zwier and D. O'Shea for discussions and preliminary efforts. We thank M. de Roosz, J. G. Holstein, T. J. Schouten, and H. Adema for technical support.

5

Author contributions

The project was initiated by C.H.W. and T.B. SiC materials were grown and prepared by N.T.S. and J.U.H. Experiments were performed by T.B. Data analysis was performed by T.B. and C.H.W. T.B. and C.H.W. had the lead on writing the manuscript.

References

[1] Koehl, W. F., Buckley, B. B., Heremans, F. J., Calusine, G. & Awschalom, D. D. Room temperature coherent control of defect spin qubits in silicon carbide. *Nature* **479**, 84–87 (2011).

[2] Zwier, O. V., O'Shea, D., Onur, A. R. & van der Wal, C. H. All–optical coherent population trapping with defect spin ensembles in silicon carbide. *Sci. Rep.* **5**, 10931 (2015).

[3] Widmann, M. *et al.* Electrical charge state manipulation of single silicon vacancies in a silicon carbide quantum optoelectronic device. *Nano Lett.* **19**, 7173–7180 (2019).

[4] Saddow, S. E. *et al.* Single-crystal silicon carbide: A biocompatible and hemocompatible semiconductor for advanced biomedical applications. *Mater. Sci. Forum* **679**, 824–830 (2011).

[5] Simin, D. *et al.* High-precision angle-resolved magnetometry with uniaxial quantum centers in silicon carbide. *Phys. Rev. Applied* **4**, 014009 (2015).

[6] Bosma, T. *et al.* Identification and tunable optical coherent control of transition-metal spins in silicon carbide. *npj Quantum Inf.* **4**, 1–7 (2018).

[7] Pandraud, G., Pham, H., French, P. & Sarro, P. PECVD SiC optical waveguide loss and mode characteristics. *Opt. Laser Technol.* **39**, 532–536 (2007).

[8] Zheng, Y. *et al.* High-quality factor, high-confinement microring resonators in 4H-silicon carbide-on-insulator. *Opt. Express* **27**, 13053–13060 (2019).

[9] Zhang, B. *et al.* Femtosecond laser modification of 6H–SiC crystals for waveguide devices. *Appl. Phys. Lett.* **116**, 111903 (2020).

[10] Calusine, G., Politi, A. & Awschalom, D. D. Silicon carbide photonic crystal cavities with integrated color centers. *Appl. Phys. Lett.* **105**, 011123 (2014).

[11] Lukin, D. M. *et al.* 4H-silicon-carbide-on-insulator for integrated quantum and nonlinear photonics. *Nat. Phot.* **14**, 330–334 (2020).

[12] Martini, F. & Politi, A. Linear integrated optics in 3C silicon carbide. *Opt. Express* **25**, 10735–10742 (2017).

[13] Falk, A. L. *et al.* Electrically and mechanically tunable electron spins in silicon carbide color centers. *Phys. Rev. Lett.* **112**, 187601 (2014).

[14] Widmann, M. *et al.* Bright single photon sources in lateral silicon carbide light emitting diodes. *Appl. Phys. Lett.* **112**, 231103 (2018).

[15] Anderson, C. P. *et al.* Electrical and optical control of single spins integrated in scalable semiconductor devices. *Science* **366**, 1225–1230 (2019).

[16] Hunsperger, R. *Integrated Optics: Theory and Technology* (Springer-Verlag New York, 2009), 6 edn.

[17] de las Casas, C. F. *et al.* Stark tuning and electrical charge state control of single divacancies in silicon carbide. *Appl. Phys. Lett.* **111**, 262403 (2017).

[18] Bond, W., Cohen, B., Leite, R. & Yariv, A. Observation of the Dielectric-Waveguide Mode of Light Propagation in p-n Junctions. *Appl. Phys. Lett.* **2**, 57–59 (1963).

[19] Bennett, B. R., Soref, R. A. & Del Alamo, J. A. Carrier-induced change in refractive index of InP, GaAs and InGaAsP. *IEEE J. Quantum Electron.* **26**, 113–122 (1990).

[20] Fox, M. *Optical properties of solids* (Oxford University Press, Oxford, 2010).

[21] Yoshida, S., Hijikata, Y. & Yaguchi, H. Nondestructive and Contactless Characterization Method for Spatial Mapping of the Thickness and Electrical Properties in Homo-Epitaxially Grown SiC Epilayers Using Infrared Reflectance Spectroscopy. *Physics and Technology of Silicon Carbide Devices* **11**, 1 (2012).

[22] Sedighi, M., Svetovoy, V., Broer, W. & Palasantzas, G. Casimir forces from conductive silicon carbide surfaces. *Phys. Rev. B* **89**, 195440 (2014).

[23] Hammer, M. 1-D mode solver for dielectric multilayer slab waveguides. `https://www.computational-photonics.eu/oms.html` (2020). Accessed: 2020-09-04.

[24] Thorlabs. 35520 Apshere Focal Shift. `https://www.thorlabs.com/images/TabImages/355230_Focal_Shift_780.gif` (2020). Accessed: 2020-04-01.

[25] Chang, L. *et al.* Analysis of the fiber-waveguide coupling efficiency and the resulting polarization dependent loss. In *2017 International Conference on Numerical Simulation of Optoelectronic Devices (NUSOD)*, 155–156 (IEEE, 2017).

[26] Wang, S. *et al.* 4H-SiC: a new nonlinear material for midinfrared lasers. *Laser Photonics Rev.* **7**, 831–838 (2013).

Appendix

5.A1 Refractive index contrast

Drude model We start from the following equation of motion for a driven mass-damper system [20]

$$\ddot{x} + \gamma\dot{x} = -\frac{e}{m^*}E, \tag{5.3}$$

where x represents the displacement of the charge carrier, γ is the damping constant, e the electronic charge, m^* the effective mass of the carrier and E the applied electric field. For an oscillating field E and a linear solution x we get

$$x = \frac{e/m^*E}{\omega^2 + i\gamma\omega}. \tag{5.4}$$

The additional polarization is then

$$P_{\text{doping}} = -\frac{Ne^2E}{m^*(\omega^2 + i\gamma\omega)}, \tag{5.5}$$

with N the number of additional nearly-free electrons in the material. This contribution to the polarization perturbs the total electric displacement as

$$D = \varepsilon_0 E + P_{\text{material}} + P_{\text{doping}}, \tag{5.6}$$

where ε_0 is the permittivity of free space and P_{material} the response of the pure material to the applied field E. The electric displacement D of the pure material can also be written using the dielectric constant. We get

$$D = \varepsilon_0\varepsilon_{\text{opt}}E + P_{\text{doping}}, \tag{5.7}$$

$$= \left(\varepsilon_0\varepsilon_{\text{opt}} - \frac{Ne^2}{m^*(\omega^2 + i\gamma\omega)}\right)E, \tag{5.8}$$

where $\varepsilon_{\text{opt}} = n_0^2 \approx 6.8$ [26] is the off-resonant dielectric constant of our silicon carbide. The dielectric constant of the doped layer would then be

$$\varepsilon_r = \varepsilon_{\text{opt}} - \frac{Ne^2}{\varepsilon_0 m^*(\omega^2 + i\gamma\omega)} = n_{\text{doped}}^2, \tag{5.9}$$

where n_{doped} is the refractive index of the doped layer. It should be noted that Eq. 5.9 is the same for positive and negative charge carriers. Either of these will lower the dielectric constant of the material.

Contrast in refractive index The contrast in refractive between doped and an undoped layers of 4H-SiC can now be calculated as function of doping level N (assuming that each dopant adds one nearly-free electron). It is worth considering that there will always be some degree of unintentional doping. For our material, this level is around $10^{14}\,\mathrm{cm}^{-3}$. The contrast will be defined as

$$\Delta n = n_{\mathrm{doped}} - n_{\mathrm{undoped}}. \tag{5.10}$$

Figure 5.A5 shows the dependence of contrast in refractive index on doping level. It can be seen that at a doping level of $10^{19}\,\mathrm{cm}^{-3}$, the contrast Δn reaches a value of $3 \cdot 10^{-3}$, which will result in total internal reflection at angles above 87.4° for light propagating from an undoped to a doped region of 4H-SiC.

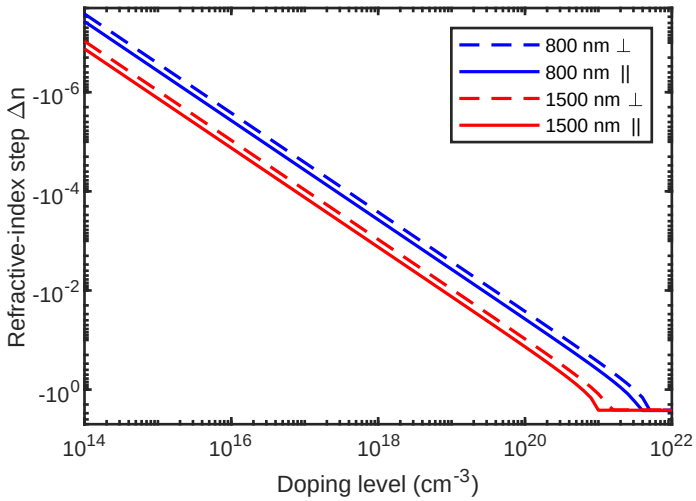

Figure 5.A5: 4H-SiC refractive-index contrast versus doping level. The step in index of refraction is plotted versus doping level for 800 and 1500 nm and for linear polarization parallel ∥ to the crystal c-axis (TM) and orthogonal ⊥ to the c-axis (TE).

Past a doping level of $10^{21}\,\mathrm{cm}^{-3}$, the contrast reaches a saturation as the real part of the refractive index becomes zero. At this point the plasma frequency, given by

$$\omega_p^2 = \frac{Ne^2}{m^* \varepsilon_0 \varepsilon_{\mathrm{opt}}}, \tag{5.11}$$

exceeds the frequency of the incident light and the material exhibits metallic reflection.

5.A2 Mode-matching for TM polarization

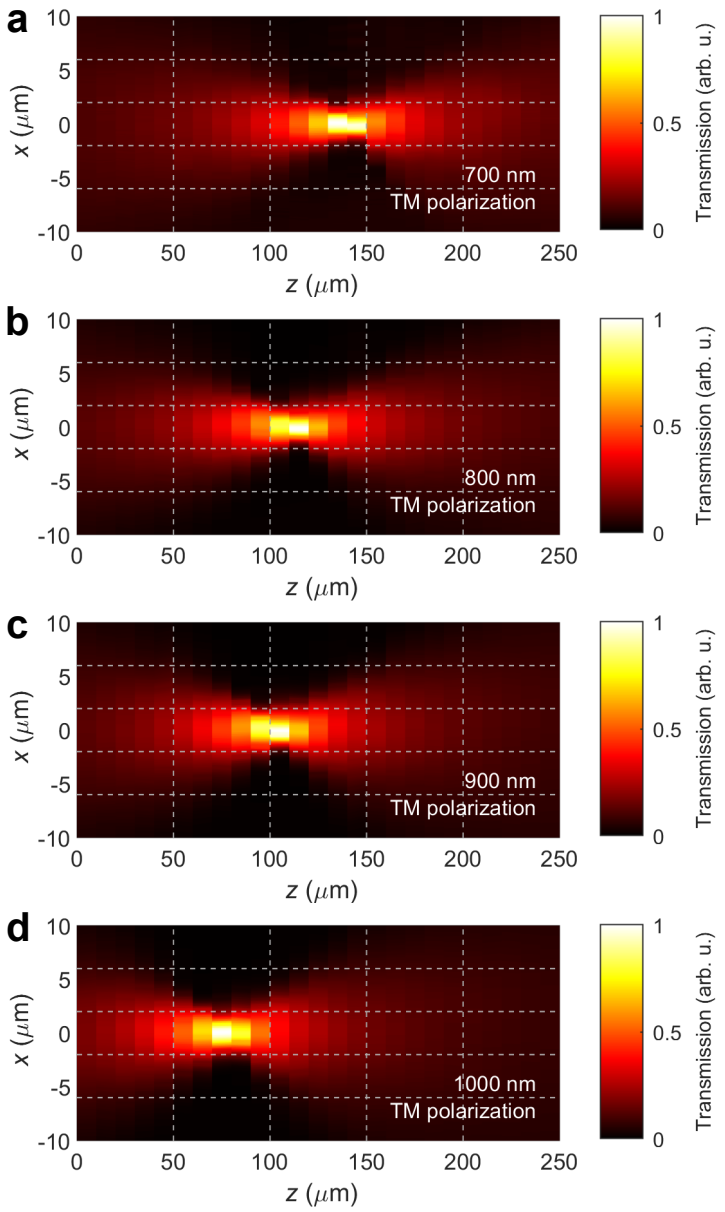

Figure 5.A6: Transmission versus laser position. The focus of the coupling lens is scanned along the z-axis and along the sample layers (x-axis). **a-d)** Transmission for 700 - 1000 nm wavelength, respectively.

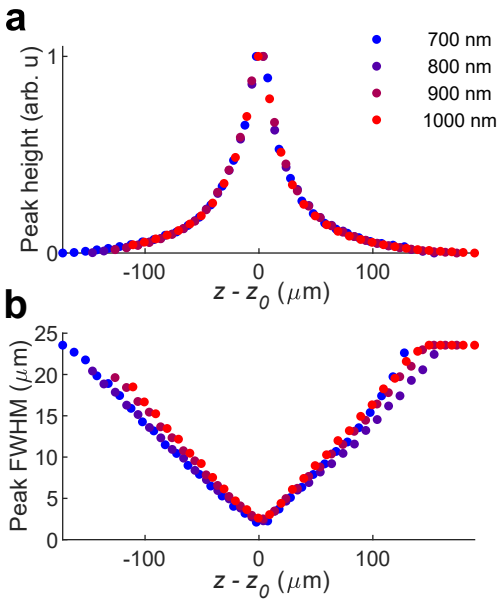

Figure 5.A7: Wavelength-independent coupling for TM polarization. a) Peak height versus position along z. **b)** Peak width along x versus position along z. Both the peak width and peak height are obtained from fitting the transmission data in Fig. 5.A6 to Gaussian curves along x.

5.A3 Wavelength independence for TE and TM waveguide modes

In order to model the electric field distribution inside a planar waveguide, we have to consider the wave nature of light. For certain angles of reflection at the core-substrate and core-cladding interfaces the wave reproduces itself after two reflections. In such cases the total field can be described by two particular plane waves that interfere with each other to generate a field distribution that is homogeneous along the propagation direction. These particular fields are the waveguide modes.

Reflection angle θ_m The reflection angle θ_m for the mode m (where $m = 0$ is the lowest order mode) can be found using the self-consistency condition: the wave should reproduce itself every second reflection. For a dielectric waveguide, this condition is

$$4\pi \frac{n_{\text{core}} d}{\lambda_0} \sin\theta_m + \varphi_{\text{clad}} + \varphi_{\text{sub}} = 2\pi m, \tag{5.12}$$

where λ_0 is the vacuum wavelength, n_{core} the refractive index for the waveguide core, d the thickness of the core, and $\varphi_{\text{clad(sub)}}$ is the phase that is accumulated upon reflection from the cladding (substrate) interface. The latter be found by solving the boundary value problem for the electromagnetic field at the core-cladding and core-substrate interfaces. For TE polarization it becomes

$$\varphi_{\text{clad(sub)}} = \tan^{-1}\left(\sqrt{\frac{\cos^2\theta_{\text{c,clad(sub)}}}{\sin^2\theta_m} - 1}\right), \tag{5.13}$$

with $\theta_{\text{c,clad(sub)}}$ the critical angle for total internal reflection on the cladding (substrate). Figure 5.A8 shows the accumulated phase per reflection angle θ at 800 nm and 1000 nm for the waveguide structures as mentioned in the main text. The total round-trip phase will not pass 2π before the critical angle for total internal reflection on the core-substrate interface $\bar{\theta}_{\text{c,sub}}$ is reached. Therefore, this waveguide will only support the fundamental waveguide mode for TE polarized light. For TM polarization the next mode ($m = 1$) can also be guided, as the round-trip phase will exceed 2π before the critical angle is reached.

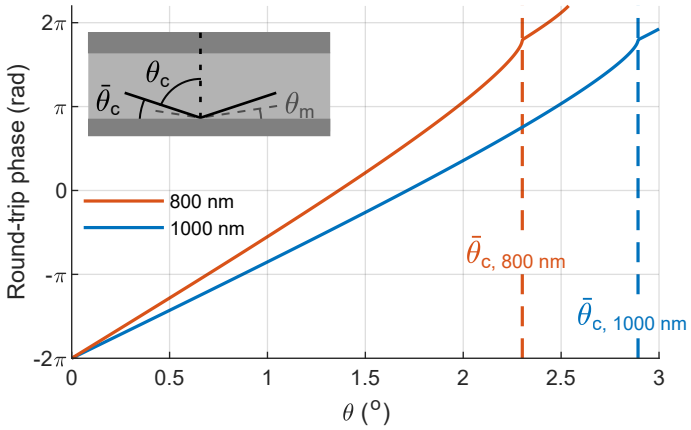

Figure 5.A8: Round-trip phase versus bounce angle for TE polarization. Phase accumulation upon two reflections versus reflection angle between the k-vector and the core/cladding interface. Shown for 800 and 1000 nm wavelengths. The red and blue dashed lines represent the complement of the critical angle for total internal reflection $\bar{\theta}_{\text{c}}$ on the core-substrate interface of our sample for 800 and 1000 nm, respectively. The inset shows how this complement angle is defined. Below $\bar{\theta}_{\text{c}}$ total internal reflection occurs.

In fact, for the doping concentrations mentioned in the main text, this

will be a single-mode waveguide for all wavelengths at TE polarization[1]. This is because the complement of the critical angle $\bar{\theta}_{\mathrm{c}}$ scales linearly with wavelength in the small angle approximation for $\bar{\theta}_{\mathrm{c}}$ and binomial approximation for Δn. The critical angle becomes

$$\begin{aligned}\cos\bar{\theta}_c &= \frac{n_{\mathrm{core}}+\Delta n}{n_{\mathrm{core}}},\\ 1-\frac{\bar{\theta}_c^2}{2} &\approx 1-\frac{\omega_p^2}{2n_{\mathrm{core}}^2c^2}\lambda_0^2,\\ \bar{\theta}_c &\approx \frac{\omega_p}{n_{\mathrm{core}}c}\lambda_0.\end{aligned}$$

Therefore, the slower phase accumulation (Eq. 5.13) at larger wavelengths is near-perfectly compensated by an increased $\bar{\theta}_c$.

[1]That is: for all frequencies below the bandgap and far enough above the plasma frequency

5.A4 Mode-matching for 1100 and 1300 nm

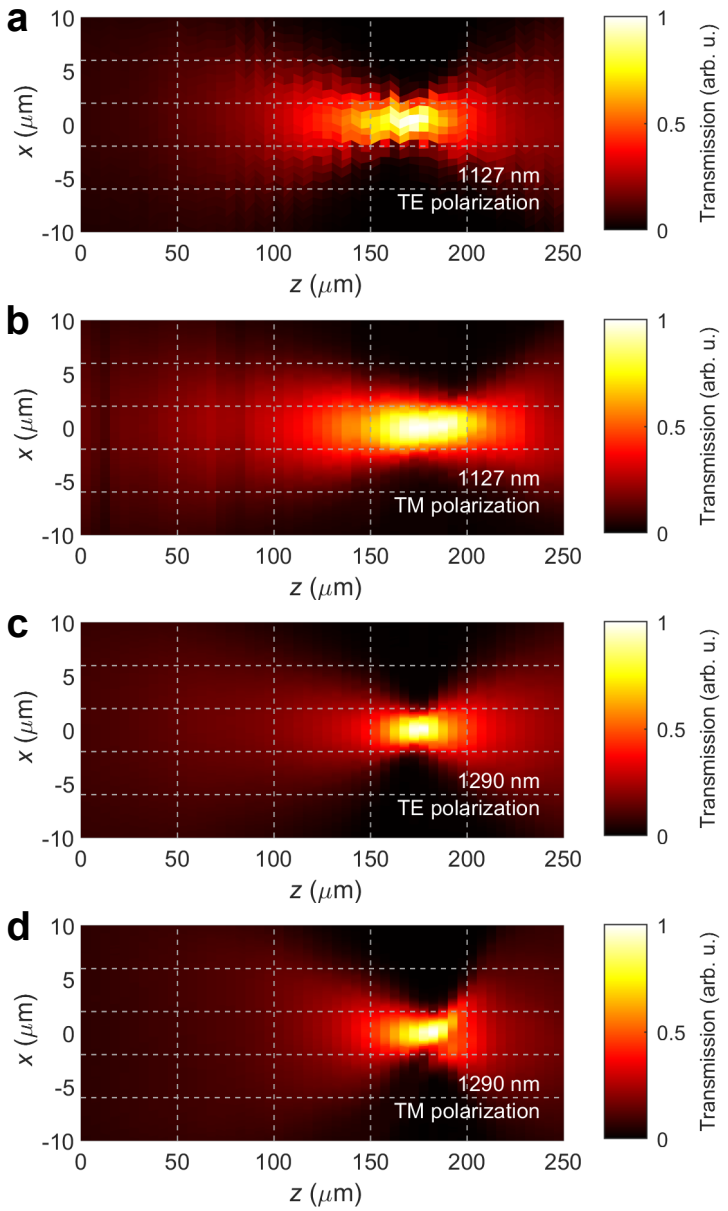

Figure 5.A9: Transmission versus laser position at 1127 and 1290 nm. The focus of the coupling lens is scanned along the z-axis and along the sample layers (x-axis). **a-b)** Transmission at 1100 nm for TE and TM polarization, respectively. **c-d)** Transmission at 1300 nm for TE and TM polarization, respectively. Note that the coordinate system has a different origin compared to Figs. 5.3 and 5.A6.

Scientific summary

Spin-active color centers in silicon carbide for telecom-compatible quantum technologies

The work in this thesis is aimed towards identifying and characterizing color-center qubits in silicon carbide that are suitable for quantum technologies. We envision applications in a large variety of fields, such as sensing, computing and communication. Especially the latter sparks our interest in SiC, as this material can host a wide range of optically-accessible and spin-active defect centers in its crystal lattice. A holy-grail type of such a color-center defect would be one operating at telecom wavelengths (around 1300 and 1550 nm) to allow for efficient long-range quantum communication using the existing world-wide fiber-optic network.

We use an all-optical approach to characterize these systems, exciting the system with one or more lasers and measuring either the absorption or subsequent luminescence. We choose to study the defects at the ensemble level, rather than the single-defect level. This generally yields large and robust signals, which makes the initial characterization easier. Unfortunately, at the ensemble level certain inhomogeneities throughout the material affect the measurement of several color-center properties, most prominently the optical transition frequency. Therefore, we often employ a two-laser spectroscopy method to isolate homogeneous subensembles.

One example of a spin-active color center in SiC is molybdenum. Its large atomic mass makes this transition-metal impurity in SiC an interesting subject of study, due to the large spin-orbit coupling that accompanies it. In chapter 2 we present the characterization of the electronic spin state of this defect. It turns out to be an $S = 1/2$ doublet for both the ground and excited state. Optical transitions between these states can be driven by laser with 1121 nm wavelength. Interestingly, we find that the Zeeman splitting of these spins is strongly anisotropic: A magnetic field component along the basal plane of the crystal does not affect the ground-state spin energy levels at all. This behavior is explained by the fact that the effective electronic spin of the defect is coupled to the crystal c-axis due to the

symmetry of the lattice and the spin-orbit coupling. With the spin state known we were able to address the Mo ensemble in a Λ system configuration to study coherent population trapping (CPT). For this quantum-physical phenomenon to occur optical transitions from two different ground states towards a common excited state are driven simultaneously by two laser fields. Upon two-photon resonance both excitation pathways interfere destructively, trapping the system in a coherent superposition of ground states that cannot be optically excited. This trapping can be observed as a dip in the laser-absorption and luminescence spectrum. The width of this dip is inversely proportional to the ensemble-averaged spin coherence time T_2^*. For Mo in 6H-SiC we extract 0.3 μs for this parameter, although it is likely that the actual homogeneous coherence time T_2 is considerably longer.

We also investigate the temperature dependence of the spin-flip time T_1 of molybdenum in SiC. This is done using a pump-probe experiment, which is discussed in chapter 3. The T_1 time exceeds seconds below 2 K and drops to tens of microseconds at 7 K. This result is quite surprising, given the fact that spin-orbit coupling is often found to be detrimental to the spin lifetime. As it turns out, the anisotropy of the g-factor, as caused by the spin-orbit coupling, reduces the coupling of Mo to nearby paramagnetic impurities with $g = 2$. Also, spin flips due to magnetic field fluctuations orthogonal to the c-axis are suppressed, as the spin is insensitive to magnetic fields in that direction. These factors explain the long T_1 times that we observed. Interestingly, spin-orbit coupling actually prolongs the spin-flip time in this case. We provide further analysis of the transitions to nearby vibrational and orbital energy levels, which leads us to conclude that the spin-flips are mostly mediated by vibrational levels in this temperature range.

Next, we look at divacancy color centers in SiC. Here the defect occurs as a neighboring carbon and silicon atom that are missing from the lattice, making a very stable defect system. Their $S = 1$ ground-state spin triplet displays long coherence even up to room temperature. In chapter 4 we demonstrate that electromagnetically induced transparency (EIT) can be achieved in divacancy ensembles with large inhomogeneous broadening. Similar to CPT, EIT can be established by driving a Λ system at two-photon resonance. This is harder to achieve for a triplet ground-state system as compared to a doublet, since the system could go dark due to spin pumping into the third level. We solve this by controlling the resonance frequencies for transitions between the energy levels with a magnetic field, such that one of the two already present laser fields counteracts any unwanted spin pumping. We fit the absorption traces exhibiting EIT to a model for our system with an $S = 1$ ground state and large inhomogeneous broadening. From these fits we extract ensemble-averaged coherence times that compare well with

literature, indicating that our method is minimally invasive to the established coherence. Furthermore, we demonstrate that it is possible to achieve double EIT where two Λ systems can be driven within the homogeneous linewidth. This can be interesting for photon-storage applications, as this effect may allow for the coherent storage of multiple photons with varying frequency.

The final part of the work in this thesis is aimed towards demonstrating SiC as an optoelectronic device platform for quantum applications. Specifically, we demonstrate monolithic single-crystal silicon carbide waveguides in chapter 5. The highest-grade SiC can only be grown on a 4H-SiC substrate. Therefore, any high-quality SiC waveguide layer will initially be grown onto the same material. This usually means that there is not reflecting interface between both layers. In order to create the proper interfaces, most existing methods of fabricating these devices in SiC rely on separating a waveguide layer from the substrate on which it is grown. This approach is not ideal as it introduces surface roughness, strain inhomogeneity and other defects in the material. We fabricated a planar SiC n-i-n junction and show that the doped outer layers act as cladding layers with a lower refractive index, while the intrinsic layer behaves as a waveguide core that confines light. We measure propagation losses of 18 dB/cm and below, which sets a promise for on-chip applications. It is expected that similar waveguides can be created from p-i-n junctions, which will allow for integrated electrostatic and RF control combined with high-intensity optical control of color-center defects in silicon carbide devices.

Wetenschappelijke samenvatting

Spinactieve kleurencentra in siliciumcarbide voor telecomtoepasbare kwantumtechnologie

Het werk in dit proefschrift is erop gericht kleurencentrum-qubits in siliciumcarbide geschikt voor kwantumtechnologie aan te wijzen en te karakteriseren. We voorzien toepassingen in verscheidene categorieën, zoals meetapparaten, computers en communicatiemiddelen. Vooral de laatste heeft onze interesse, aangezien dit materiaal een grote verzameling aan optisch toegankelijke en spinactieve defectcentra kan bevatten. De heilige graal onder de kleurencentra zou er een zijn die opereert op de telecomgolflengtes (rond 1300 en 1550 nm) om zodoende effectieve kwantumcommunicatie op lange afstand via het bestaande wereldwijde optische vezelnetwerk mogelijk te maken.

We gebruiken een volledig optische aanpak om deze systemen te karakteriseren, waarbij ze aangeslagen worden met één of meerdere lasers en we vervolgens de absorptie of daaropvolgende fotoluminescentie meten. We kiezen ervoor om de defecten te bestuderen op het ensemble niveau in tegenstelling tot het niveau van een enkele defect. Over het algemeen resulteert dit in sterke en robuuste signalen, die de initiële karakterisatie vergemakkelijken. Op ensemble niveau worden de metingen van verschillende eigenschappen van de kleurencentra helaas beïnvloed door bepaalde inhomogeniteiten in het materiaal. De voornaamste van deze eigenschappen is de optische transitiefrequentie. Daarom gebruiken we vaak een tweelaserspectroscopiemethode om homogene subensembles te isoleren.

Een voorbeeld van spinactieve kleurencentra in SiC is molybdeen. De grote atomische massa maakt dit overgangsmetaal tot een interessant studieobject vanwege de sterke spin-baan-koppeling die daarbij hoort. In hoofdstuk 2 presenteren we de karakterisatie van de elektronische spintoestand van dit defect. Het blijkt te gaan om een $S = 1/2$ doublet voor zowel de grondtoestand als de aangeslagen toestand. Optische transities tussen deze toestanden kunnen worden gedreven door een laser met een golflengte van 1121 nm. Opmerkelijk genoeg blijkt dat de Zeemansplitsing

van deze spins sterk anisotroop is: een magnetisch veldcomponent langs het grondvlak van het kristal beïnvloedt de energieniveaus van de grondtoestandspin algeheel niet. Dit gedrag valt te verklaren door het feit dat de effectieve elektronische spin van het defect is verbonden aan de c-as van het kristal door de symmetrie van het rooster en de spin-baan-koppeling. Deze kennis van de spintoestand stelt ons in staat het Mo-ensemble aan te slaan in een Λ-systeem-configuratie om coherente populatie-insluiting (*coherent population trapping*, CPT) te bestuderen. Dit kwantumfysische fenomeen komt voor wanneer optische transities uit twee verschillende grondtoestanden naar één gezamenlijke aangeslagen toestand tegelijkertijd worden aangedreven door twee laservelden. In tweelaserresonantie zullen beide excitatiepaden destructief interfereren. Daarbij wordt het systeem ingesloten in een coherente superpositie van beide grondtoestanden en kunnen de grondtoestanden niet meer optisch aangeslagen worden. Deze insluiting kan waargenomen worden als een inzinking in het laserabsorptie- en luminescentiespectrum. De breedte van deze inzinking is omgekeerd evenredig met de spincoherentietijd, gemiddeld over het ensemble, T_2^*. Voor Mo in 6H-SiC vinden we 0.3 μs voor deze parameter, hoewel het waarschijnlijk is dat de daadwerkelijke homogene coherentietijd T_2 aanzienlijk langer is.

We onderzoeken ook de temperatuurafhankelijkheid van de spinfliptijd T_1 van molybdeen in SiC. Dit doen we door middel van een *pump-probe*-experiment, zoals besproken in hoofdstuk 3. De T_1-tijd overschrijdt secondes onder 2 K en valt terug naar tientallen microseconden bij 7 K. Dit resultaat is verassend, gegeven het feit dat spin-baan-koppeling vaak nadelig is voor de spinlevensduur. Het blijkt dat de anisotropie in de g-factor, die veroorzaakt wordt door de spin-baan-koppeling, de koppeling verzwakt tussen Mo en naburige paramagnetische onzuiverheden met $g = 2$. Daarnaast worden spinflips door fluctuaties in het magnetische veld langs de c-as onderdrukt, omdat de spin ongevoelig is voor magnetische velden in die richting. Deze factoren verklaren de lange T_1-tijden die we observeren. Interessant genoeg helpt de spin-baan-koppeling in dit geval juist mee met het verlengen van de spinlevensduur. We leveren verdere analyse van transities naar naburige vibrationele en orbitale energieniveaus, die ons tot de conclusie brengen dat de spinflips in dit temperatuurbereik vooral plaatsvinden via vibrationele niveaus.

Vervolgens kijken we naar *divacancy*-kleurencentra in SiC. In dit geval komt het defect voor als naburige koolstof- en siliciumatomen uit het rooster missen, wat het tot een zeer stabiel defectsysteem maakt. De $S = 1$ grondtoestandspin triplet laat lange coherenties zien, zelfs op kamertemperatuur. In hoofdstuk 4 demonstreren we dat

elektromagnetisch geïnduceerde transparantie (*electromangetically induced trasnparency*, EIT) bewerkstelligd kan worden in *divacancy*-ensembles met een sterke inhomogene verbreding. Vergelijkbaar met CPT kan EIT tot stand gebracht worden door een Λ-systeem aan te drijven in tweefotonresonantie. Dit is lastiger te bereiken voor een triplet grondtoestandsysteem vergeleken met een doublet, omdat het systeem verduisterd zal worden door toedoen van spinpompen naar een derde niveau. We lossen dit op door de resonantiefrequenties van de transities tussen de energieniveaus te sturen met een magnetisch veld, zodat één van de twee aanwezige laservelden het ongewilde spinpompen tegengaat. We fitten de absorptiespectra die EIT vertonen aan een model voor ons systeem met een $S = 1$ grondtoestand en sterke inhomogene verbreding. Uit deze fits halen we de coherentietijden, gemiddeld over het ensemble, die goed overeenstemmen met de literatuur. Dit geeft aan dat onze methode een minimale invloed heeft op de tot stand gebrachte coherentie. Verder tonen we dat het mogelijk is om dubbele EIT te bereiken, waar twee Λ-systemen tegelijkertijd gedreven kunnen worden binnen dezelfde homogene lijnbreedte. Dit kan interessant zijn bij toepassingen voor fotonopslag, omdat dit effect het coherent opslaan van meerdere fotonen met verschillende frequenties mogelijk zou kunnen maken.

Het laatste deel van het werk in dit proefschrift is erop gericht te laten zien dat SiC kan dienen als opto-elektronisch componentenplatform voor kwantumtoepassingen. In hoofdstuk 5 demonstreren we monolithische golfgeleiders in enkelvoudig kristallijn siliciumcarbide. De hoogste kwaliteit van SiC-kristallen kan alleen verkregen worden wanneer deze op een 4H-SiC substraat gegroeid worden. Daarom zal elke hoogwaardige SiC-golfgeleider in eerste instantie op hetzelfde materiaal gegroeid moeten worden. Dit betekent doorgaans dat er geen reflecterend grensvlak tussen beide lagen bestaat. Om toch de juiste grensvlakken te creëren zijn de meeste bestaande fabricagemethodes afhankelijk van het scheiden van de golfgeleiderlaag van het substraat waarop deze is gegroeid. Dit is geen ideale aanpak, aangezien het oppervlakteruwheid, rekinhomogeniteit en aanvullende defecten in het materiaal introduceert. Wij hebben een vlakke SiC n-i-n-overgang gefabriceerd en laten zien dat de gedoteerde buitenlagen zich gedragen als *cladding* van de golfgeleider, terwijl de intrinsieke laag zich als lichtinsluitende kern gedraagt. We meten voortplantingsverliezen van 18 dB/cm en lager. Dit stelt een belofte voor *on-chip* toepassingen. Het is te verwachten dat vergelijkbare golfgeleiders gemaakt kunnen worden van p-i-n-overgangen. Dit zal het mogelijk maken kleurencentrumdefecten te besturen met geïntegreerde elektrostatische en RF technieken, gecombineerd met besturing door optische velden met hoge intensiteit.

Acknowledgments

This PhD thesis concludes a decade of my life in Groningen. It has been a wonderful time! I would like to take the opportunity to thank everyone that was involved in my PhD for their contributions.

First of all, I would like to thank Caspar van der Wal. I came to your group in 2015 for my final master research project and we got along very well right from the start. I admire the way you divide your time as a group leader and ZIAM director, finding the time to regularly meet with PhD students and always being available when needed. Our group meetings were always fun and effective and I am really happy to have been part of a team that worked so well together. I also really liked running together on several occasions, most notably the intensive 4-mile-of-Groningen preparation training sessions we had in the Tiergarten park during a conference in Berlin.

Next, I would like to thank Remco Havenith for being a very involved copromotor. You are a valuable collaborator on several projects during my PhD and I enjoyed all the chats and discussions we had over the years. I also wish to thank Albert Polman, Cristian Bonato and George Palasantzas for assessing my thesis. George, thanks also for all the fun conversations we had.

I am very grateful to my two paranymphs Carmem and Joop, thank you for being such nice colleagues. Carmem, I appreciate our teamwork very much. I think us playing to each other's strengths has resulted in some valuable and high-quality science output. Good luck wrapping up your PhD work this year! Joop, I liked working with you for the past year, you bring a great no-nonsense mentality to the group. I wish you all the best for your PhD and I hope that you will demonstrate a true telecom-compatible qubit in SiC.

Many thanks to the other members of the QD team. Xu, thank you for introducing me to the group and for always being genuinely interested, regardless of topic. Gerjan, thank you for our very close collaboration in working tirelessly to get the measurement setup to work and for providing

a different point of view when needed. Olger, thank you for leaving a well thought-out measurement setup. Thanks to you and Jakko too for the helpful discussions after your PhDs finished. I am also grateful for all the students that completed their research projects with me: Robert, Fran, Xiangyang, Wessel, Danny and Robbert, thank you very much for all the work you did. You all played an invaluable part in my PhD project. Next, I would like to thank N.T. Son, Ivan G. Ivanov, Jawad U. Hassan and Adam Gali for the fruitful collaboration with our team.

Within the entire FND I want to thank everyone for their involvement in my PhD, but also for all the activities, dinners, drinks, lunches and coffee breaks that we had over time. Thank you Job, Arijit, Dennis, Anouk, Eswar, Ping, Anna, Crystal, Madhu Freddie, Arjan, Tian, Xiangyang, Mallik, Alexey, Obed, Julian, Jorge, Kumar, Geert, Siddhartha and Sytze. Thanks also to Talieh, Frank, Jan, Pep, Christian, Roald for being the friendly office mates that you were. Special thanks to Anna, Marleen, Johan, Tom, Hans, Herman, Feitze and Martijn without whom this research group could never function. Also thanks to the other group leaders within FND: Tamalika, Bart and Marcos, thanks for the many interesting, fun and warm interactions we had. I had fun outside the FND group as well, for this I would like to thank Pascal, Yori, Marten, Edwin, Arjan and the members of the Francken club.

Dan wil ik nu graag mijn familie en schoonfamilie bedanken. Pap, mam, Nick, Helen, Joost, Elsje, Menno, Martin en Chris-Jan, bedankt voor jullie interesse en steun de afgelopen tijd en ook vooral bedankt voor de gezelligheid en warmte door de jaren heen. Martin, bedankt ook voor het geslaagde ontwerp van de omslag van dit proefschrift. Tot slot wil ik graag mijn vrouw bedanken: lieve Machteld, je bent een geweldig voorbeeld geweest voor mijn promotieonderzoek en je doortastendheid hierin streef ik graag na. Het is geweldig jou als maatje te hebben en ik kijk uit naar ons nieuwe avontuur in Denemarken!

Tom Bosma
Copenhagen, Denmark
January 5, 2021

Curriculum Vitae

Tom Bosma

21 March 1992	Born in Sneek, the Netherlands.
2004-2010	Gymnasium at Bogerman College, Sneek, the Netherlands.
2010-2014	B.Sc. Applied Physics at the University of Groningen, Groningen, the Netherlands.
2014-2016	M.Sc. Applied Physics at the University of Groningen, Groningen, the Netherlands.
2016-2021	Ph.D. research at the Zernike Institute for Advanced Materials, University of Groningen, the Netherlands, under the supervision of prof. dr. ir. C. H. van der Wal. Subject: Spin-active color centers in silicon carbide for telecom-compatible quantum technologies.

List of Publications

1. *Broadband single-mode monolithic waveguides in 4H-SiC*
   T. Bosma, X. Yang, J.U. Hassan, N.T. Son, C.H. van der Wal, *in preparation* (2021).

2. *Electromagnetically induced transparency in inhomogeneously broadened divacancy defect ensembles in SiC*
   O.V. Zwier*, T. Bosma*, X. Yang, W.J. Brinkhuis, D. OŚhea, A.R. Onur, T. Oshima, N.T. Son, C.H. van der Wal, *in preparation* (2021).

3. *Spin-relaxation times exceeding seconds for color centers with strong spinorbit coupling in SiC*
   C.M. Gilardoni*, T. Bosma*, D. van Hien, F. Hendriks, B. Magnusson, A. Ellison, I.G. Ivanov, N.T. Son, C.H. van der Wal, *New J. Phys.* **22**, 103051 (2020).

4. *Circuit-model analysis for spintronic devices with chiral molecules as spin injectors*
   X. Yang, T. Bosma, B.J. van Wees, C.H. van der Wal, *Phys. Rev. B* **99**, 214428 (2019).

5. *Identification and tunable optical coherent control of transition-metal spins in silicon carbide*
   T. Bosma*, G.J.J. Lof*, C.M. Gilardoni, O.V. Zwier, F. Hendriks, B. Magnusson, A. Ellison, A. Gällström, I.G. Ivanov, N.T. Son, E. Janzén, C.H. van der Wal, *npj Quantum Inf.* **4**, 48 (2018).

* These authors contributed equally